CENTRE FOR QUANTUM AND OPTICAL SCIENCE
FACULTY OF SCIENCE, ENGINEERING AND TECHNOLOGY
SWINBURNE UNIVERSITY OF TECHNOLOGY

Exotic fermionic superfluidity in low-dimensional atomic Fermi gases

A thesis submitted for the degree of
Doctor of Philosophy

CANDIDATE:

Umberto Toniolo

SUPERVISORS:

A/Prof. Hui Hu

Prof. Xia-Ji Liu

Acknowledgement

Faber est, quisque, fortunae suae, i.e. "Each man is the maker of his own destiny" is by far the best sentence to fully embody the whys and hows I've ended up in the Down Under. Reality (Australia being the reality), in fairness, hasn't failed expectations and definitively I can check the box "life experience overseas" from the bucket list. The subplot of this long adventure in Australia read: (1) completion of the Ph.D. degree in Physics and (2) learn how to surf and I couldn't be happier to say that both (almost) got the "achieved" status.

Needless to say that human beings don't sparsely populate Earth but rather gather and help each other: indeed this gift of life didn't pass unobserved. First of all, I would like to thank my supervisors, Hui and Xia-Ji, that granted me the opportunity of a fully funded Ph.D., have been a constant source of ideas and very generous with me in many regards. A special thank goes to my workmate Brendan who shared with me an extensive deal of knowledge, spanning from the page layout of an article to how to achieve a kneebar move on a V6 climb at the Lactic Fact... whatever, a vast diversity of topics. Amongst my colleagues I would like also to thank Jia and Xiaolong, the latter without whom I probably would have missed all the deadlines of the Ph.D. program at Swinburne.

Nowadays, physics and computer coding are so related that I needed someone to teach me high level C++ coding. A very deep thank here goes to the master of parallelising/coding/geeking and all of that, Simon. Honestly, man, you saved me during the first year.

A special thank goes to Seb and Chris for the endless conversations about... really anything that comes to mind: economic stability of the Eurozone, wild animal biosphere of Maffra VIC, the next best theory of Quantum Gravity, "the Lord of the Rings" how to hate it and how to love it, Furphy or James Boag's pure Tasman water, and many other things. I wish them the best luck for their careers.

A special mention and the dedication of this thesis goes to my friends Alessandro, Pavel and Nathan.

Abstract

This thesis is devoted to the study of exotic superfluid phases in strongly interacting Fermi gases. While superfluidity in ultracold gases has many distinct manifestations we choose to address first a mean field approach to imbalance Fermi gas and then, in the balanced case, we studied the dimensional crossover of a confined gas and other relative feautures.

Firstly, we present an extensive study of the Larkin-Ovchinnikov (LO) phase in a two-dimensional spin-polarized Fermi gas. In the context of Fulde-Ferrell-Larkin-Ovchinnikov (FFLO) phase, we explore the availability of a very wide and generic class of energy gap functions with explicit space dependency. We inspecte the nature of the phase transitions that are available via a saddle point approximation: in particular in between the fully paired Bardeen-Cooper-Schrieffer (BCS) state, an exotic LO phase, and the partially polarized free Fermi gas (N_{PP}). The order of phase transitions has been carefully examined and has led us to reconsider the idea of a second order phase transition between the exotic inhomogeneous phase and the normal free imbalanced Fermi gas. The superfluid density of the LO phase has been computed in the perpendicular direction with respect to the direction in which the spatially dependend gap parameter appears, moreover we investigate the relationship between superfluid density and the spin polarisation.

We then move to the theoretical description of the crossover from three dimensions (3D) to two (2D) in a strongly interacting atomic Fermi superfluid through confining the transverse spatial dimension. Using beyond mean field methods, we determine the zero-temperature equation of state and Landau critical velocity as functions of the spatial extent of the transverse dimension and interaction strength. In the presence of strong interactions, we determine a criterion to distinguish three dimensional regimes and we explicitly map out a dimensional crossover diagram using the location of the superfluid maximum critical velocity, which exhibits distinct dependence on the transverse dimension from 2D to quasi-2D, and to 3D. Through the dynamic structure factor we propose an experimental viable measurement to probe the dimensional crossover diagram by using Bragg spectroscopy.

In the final part of the thesis, due to the recent experimental interests, we address

the role played by dimensionality on the breathing mode quantum anomaly in a harmonically trapped balanced Fermi gas at zero temperature. Based on our model for the dimensional crossover for a strongly-interacting Fermi gas we employ periodic boundary conditions (PBC) to simulate the dimensionality of the system and then we impose a local density approximation (LDA), with two different schemes, to achieve a model of a harmonically trapped Fermi gas. By using sum-rules techniques we compute the breathing mode frequency associated with a small variation of the transverse trapping frequency and we describe its behaviour as a function of the dimensionality. We finally compare our results with previous predictions.

Declaration

I, Umberto Toniolo declare that this thesis entitled:

"*Exotic fermionic superfluidity in low-dimensional atomic Fermi gases*"

is my original work and contains no material which has been submitted previously, in whole or in part, in respect of any other academic award and to the best of my knowledge and belief contains no material previously published except where due reference is acknowledged in the text.

Umberto Toniolo

Centre for Quantum and Optical Science

Faculty of Science, Engineering and Technology

Swinburne University of Technology

Melbourne, Australia

13 December 2018

Contents

Chapter 1

Introduction

This introductory chapter is devoted to outlining the content of this thesis and provide an introductory explanation to all the topics this work deals with. We start with a brief historical summary containing the major cornerstones of the research in condensed matter and, in particular, the ultracold gases field of research. The motivations of this thesis are then exposed followed by the scientific results and conclusions achieved during the Ph.D. term. We will focus in particular, at the end of the chapter, to emphasize the original contribution of our work presented to the Condensed Matter scientific community in the form of published papers.

1.1 Historical background on superfluidity and superconductivity

The foundations of condensed matter have a remarkably simple birthplace: the paramount observation that the discretisation of the spin eigenvalues splits the particles, in which nature is composed, into two different sectors. The fermionic sector has spin eigenvalues always equal to a half-integer multiple of the Planck constant $\hbar$, whereas the bosonic sector allows only integer multiples of $\hbar$. Such a difference enriches physics of two systems which behave in completely different ways.

In 1925, Wolfgang Pauli formulated his Pauli exclusion principle for the electron, basically stating that the wave function of a system of indistinguishable electrons changes its phase by a factor $e^{i\pi\sigma}$ when we impose a permutation, with parity σ, on the electrons. This successful idea turns out to be a feature the electron shared with every half-integer spin field in Quantum Field Theory. Indeed it came to no surprise when in the 50s, within the formalism of the Gårding–Wightman axioms [1–3], the spin-statistics theorem (i.e. the relation spin-phase) got proven for any spinorial quantum field. From our point of view, since we will deal with ultracold gases, the

fermionic nature of a system doesn't allow the ground state of a many-body state to be squeezed on the lowest energy eigenvalue of the Hamiltonian, but particles fill up eigenstates up to the system's Fermi energy.

On the other side of the fence, the bosonic sector, which enjoys the property of not changing the wave function phase when indistinguishable particles are swapped in a many-body system, had attracted the interests of Satyendra Nath Bose and Albert Einstein in 1924 [4]. A many-body system of bosonic particles, when cooled down enough, undergoes a phase transition to a new state of matter we now call the Bose-Einstein condensate (BEC). Its predominant feature is that it can be relatively macroscopic but still be described by a single wave function: it provides a direct example of a Quantum system that verifies the Copenhagen interpretation of Quantum Mechanics at the scale of the µm, interpreting the wave function as a probability distribution.

Within the formalism of the canonical ensemble, the probability of populating an excited state is given by the Bose-Einstein probability distribution,

$$f_{BE}(\varepsilon) = \frac{1}{e^{\beta(\varepsilon - \mu)} - 1} \tag{1.1}$$

where $\beta = (k_B T)^{-1}$ is the inverse of the temperature, k_B is the Boltzmann constant and μ the chemical potential. The density of particles is always linked, in the absence of interactions, to a critical temperature T_c that returns $\mu(T_c) = 0$ (absence of fugacity) and yields the famous equation

$$\beta_c^{-1} = k_B T_c = \frac{2\pi\hbar^2}{m} \left(\frac{n}{(2s + 1)\zeta(3/2)} \right)^{2/3} \tag{1.2}$$

where s is the integer spin of the particles we are considering, ζ is the Riemann's zeta function and n the particle density. Such critical temperature can be understood as the energy at which the inter-particle spacing in the many-body system, $n^{-1/3}$, becomes comparable with the de Broglie wavelength, $\lambda_{dB}(T) = \sqrt{\frac{2\pi\hbar^2}{mk_B T}}$, associated with the particles. This idea became indeed very useful when a non-classical "superfluid" phase of Helium below 2.2 K was discovered. Fritz London then suggested that the Bose-Einstein condensation might have been the right tool to explain this new phenomenon, though it took nearly 70 years to experimentally realise [5, 6] the first BEC with alkali atoms, in 1995, and subsequently prove it undergoes a superfluid transition.

In 1908 Heike Kamerlingh Onnes was the first to obtain liquid Helium close to the temperature of 1.5 K. By using this superfluid Helium, in 1911, he managed to cool down Mercury, at 4.2 K, and discovered that it displays a vanishing electrical resistance [7]. Furthermore, increasing the electron scattering in such a regime, no deviation from this behaviour could be observed. A similar peculiar characteristic

was then found in Indium (3.4 K), tin (3.72 K) and lead (7.19 K). Moving further towards other available compounds the critical temperature associated to this absence of electrical resistance was found to be even higher, for instance the nitrate of Niobium pushed it to 17.3 K. This limit increased through decades, in 1973 was brought to 22 K in the Nb_3Ge [8], and nowadays it stands stationary, at low pressures, around 135 K in exotic Cuprates compounds [9–11] with a record critical temperature 164 K when a specific Cuprate is brought to high pressure [12].
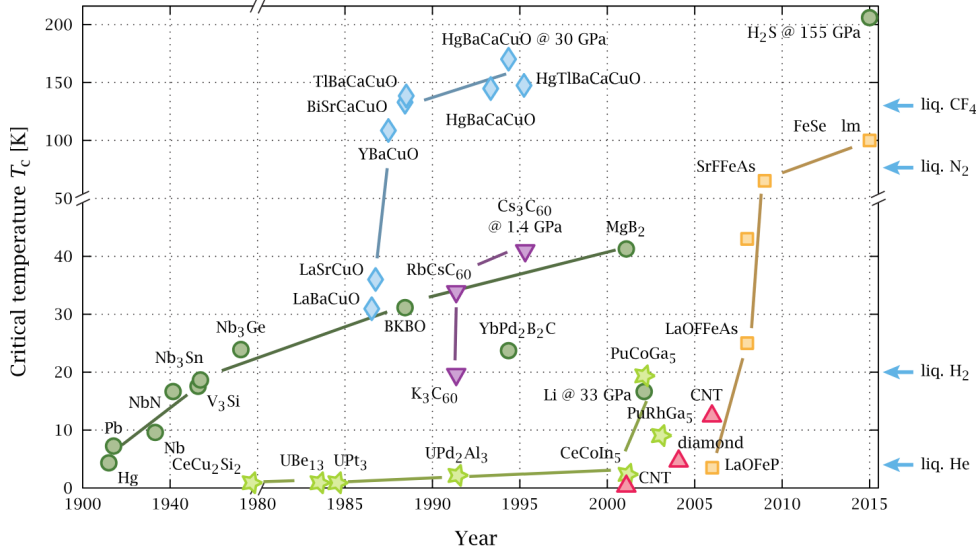
Figure 1.1: *The evolution of the critical superfluid temperature T_c from Onnes experiment (bottom left) to nowadays. From [13].*

This phenomenon was called superconductivity but brought an even deeper novelty in physics: a gas of electrons, or fermions in general, undergoes a superfluid phase. The charge of the electron in the superfluid phase is responsible for the superconductivity. At the time of the discovery of superconductivity, several properties of this new phase of matter were tracked down: (a) ABSENCE OF DC RESISTANCE: persistent flowing electrical currents have been trapped in superconducting coils with expected decay rate of 10^5 years [14]. DC current resistance can be considered suppressed in any soft core superconducting material with a lower estimate of 10^{-15} times the normal phase resistance. (b) CRITICAL FREQUENCY FOR AC CURRENT RESISTANCE: at zero absolute temperature has been observed a complete suppression of resistance whenever the AC frequency is less then $\nu_{AC} \approx 3.5 \frac{k_B T_c}{2\pi\hbar}$, where T_c is the superconducting phase transition temperature. Instead, at finite temperature, we observe a finite resistance for any frequency $\nu < \nu_{AC}$ and a normal phase behaviour when $\nu \gg \nu_{AC}$. (c) MEISSNER EFFECT: below a certain critical temperature, external magnetic fields are expelled. Inside a core the superconductor

behaves like an ideal diamagnet with magnetisation $\chi_m = -1$ and outside the magnetic field has maximum penetration depth of 5×10^{-6} cm, up to a critical value of the magnetic field when superconductivity breaks. (d) CRITICAL MAGNETIC FIELD: the repulsion of a magnetic field H costs, per volume, an energy increase $H^2/(8\pi)$ but a phase change must undergo, on the energetically favourable side, an energy decrease. Hence it must exist a critical magnetic field $H_c(T)$. (e) FROZEN INTERNAL MAGNETIC FIELD: a vanishing resistance requires only the magnetic field time derivative to vanish, hence we still have the possibility of a magnetic field captured inside the superconducting core. (f) FLUX QUANTISATION: the magnetic flux within a superconducting ring is discrete and constant in time. In the case of a hollow superconductor, the discrete flux is multiple of $hc/(2e) \approx 4 \times 10^{-6}$ gauss cm^{-3}.

The picture of superconductivity was definitively more puzzling than the bosonic superfluidity. With impressive intuition London suggested that superfluidity and superconductivity were essentially peculiar quantum mechanical features that happen on macroscopic scale. Again in 1950, London's superfluid theory provided us a paramount suggestion: to explain superconductivity, a theory that involves a new kind of bound state between two fermions with total charge of twice the electron charge was needed. Unfortunately while bosons are likely to occupy the same eigenstate when at low temperatures, fermions not only obey the Pauli exclusion principle, but, like in the case of electrons, strongly repel each other due to Coulomb interaction. Finally, the degeneracy temperature of conducting electrons (the Fermi temperature) is of the order of thousands of Kelvin, hardly a viable way to explain an eventual "fermionic condensation" which would appear at very low temperatures.

As we know, the breakthrough came when it was realised by Cooper, in 1956, that fermions on the rim of their Fermi sphere, in presence of an arbitrarily small attractive potential, form weakly bound pairs. In metals, when the temperature is low enough, the crystal structure screens the Coulomb interaction of far away distant electrons and provides a phonon-mediated electron-electron interaction. In this way it became clear that the Fermi sea (i.e. the ground state of the free Hamiltonian for fermions) is unstable towards a ground state made of long range pairs of fermions by adding an attractive interaction. Eventually, in 1957, Bardeen Cooper and Schriffer published their theory of superconductivity (BCS) which provided the form of the wave function associated with the new ground state for fermions [15]. When the electron-electron interaction was tuned via the lattice phonon their theory was able to explain the superconducting critical temperature of all the metals investigated at that time. We describe the BCS theory within the field theoretical formalism in Chapter 2 since it sets the stage for almost all the investigations presented in the current work.

1.2   Ultracold interacting gases

The first experimental realisation of a Bose-Einstein condensation was achieved in 1995 [5, 6], and paved the way to the realisation of new states of matter. At low temperature, as suggested before, the comparable size of inter-particle distance and de Broglie wave-length induces macroscopic quantum effects. Despite an extremely low atom density in these gases, they exhibit many-body correlations that affect both their microscopic and macroscopic properties.

Ultracold gases then represented both a theoretical and experimental challenge, but in return were expected to enlighten our comprehension of very interesting and unknown physical phenomena, namely those phenomena that are related with superfluidity and superconductivity but can be hardly investigated via ordinary superfluids. Moreover, nowadays ultracold gases are believed to be a viable setup for quantum computations and quantum simulations [16], i.e. an alternative way of understanding strongly-interacting theories that cannot be perturbatively expanded in orders of the interaction parameters. Furthermore, ultracold atoms may even allow to create exotic states of matter, which cannot otherwise be observed in nature. Ultracold atoms are also used as precision measurement tools as it is possible to remove the thermal noise which is unavoidable when dealing with macroscopic systems.

An impressive variety of experimental tools made ultracold gases relatively simple to investigate. The evaporative cooling technique allows to reach temperatures of the order of 10^{-9} K and gases can be trapped with harmonic oscillator traps, hard walls or even an arbitrary shape of the system's boundaries. Exploiting different trapping methods allows experiments to undergo different dimensional regimes, for instance forcing the dynamics to evolve in a one- or two-dimensional landscape. Quantum selection rules allow tunnelling through certain quantum states allowing to select specific features and neglect others, such a way that it is easier to find theoretical models that accurately describe a given experimental setup. The interactions between atoms can be tuned and a highly controllable environment can be achieved.

The first theoretical approach to study ultracold gases has been the mean-field (MF) theory. The lack of computational control we experience, due to huge amounts of particles or interactions, can be overcome, in some regime of weak interactions between particles, by the approximation that each particle instead of interacting with any other particle in the system, sees them as a whole, as an external average field. This approach is very reliable, at least for qualitative results in a large variety of systems. For instance, we can remind that the Gross-Pitaevskii equation is a mean-field theory. The BCS theory of superconductivity in weakly interacting

(im-)balanced Fermi gases is also a mean-field theory. It is also correct to say that mean-field theory cannot predict all the properties of systems quantitatively and struggles in regimes in which inter-particle interactions are strong. In fact, a major goal for condensed matter physics has been to find methods to go beyond the MF framework.

There are two ways to create a beyond mean-field effect. Optical lattices can be used to suppress the tunnelling through lattice sites, reducing the average kinetic energy per particle [17, 18]. The resulting lower dimensionality of a system increases the role of fluctuations (higher order corrections to a mean-field treatment), leading to phenomena like the Berezinskii-Kosterlitz-Thouless phase [19, 20] or properties like the Mermin-Wagner theorem [21] and so on. Alternatively, and Feshbach resonances can be used [22, 23] to tune interactions described by the contact potential model and its related scattering length.

Feshbach resonances can be understood using the theoretical framework derived by Ugo Fano [24] and Herman Feshbach [25] which describes how it is possible to couple a scattering state with a bound state. The Fano-Feshbach method of controlling the scattering length in the scattering process of two particles (the open channel) allows to tune the energy of such state close to the energy of a bound state (closed channel). Such proximity allows resonance and the event of both particles to fall virtually (oscillating from and towards the bound configuration) into the bound state.
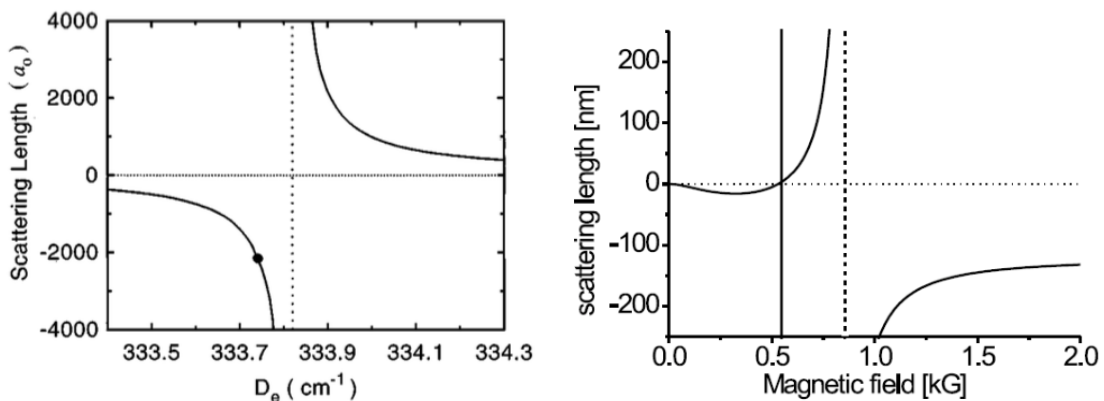
Figure 1.2:   *(Left) The scattering length of the open channel as a function of the dissociation energy D_e, i.e. the distance to the closed channel matching resonance. The dashed line is the binding energy of the closed channel [26]. (Right) The divergence of the open channel scattering length when open and closed channel have the same energy and undergo resonance [27].*

Moreover, if the magnetic moments of a pair of particles in these two channels are, as it often happens, different and in particular the bound state stands below the continuous spectrum of excitations, the Fano-Feshbach resonance allows to raise

such a closed channel above the continuous spectrum threshold. An experimental paramount application of this phenomenon can be easily described: indeed the ^{6}Li has a favourable configuration to probe such resonance [26]. The open channel in this case is given by two atoms with their valence electrons in the lowest angular momentum eigenvalue ($l = 0$). The symmetry of the molecular state with respect to nuclear exchange restricts the possible values of total nuclear spin to $I = 1$. The total spin angular momentum (electron and nucleus spins) $F = S + I$ of both particles can couple in either a triplet or singlet state. We notice some remarkable facts:

(i) the triplet state has a large and negative scattering length, i.e. in a certain condition of proximity, atoms feel attracted;

(ii) there is a molecular bound state that is accessible from this scattering state through absorption and emission of photons from the former triplet state. The dissociation energy, D_e that the scattering state would have, if bound, is really close to this molecular bound state energy

We usually refer to a Fano-Feshbach resonance when a closed channel has almost the same energy of a scattering open channel. When tuning an external magnetic field it is possible to modify the scattering length of the open channel. In this case the dissociation energy of the open state can match exactly the closed channel resonance (see Fig. 1.2). This discovery was experimentally proved in 2002 [28] and it is often referred as stability of a strongly-interacting Fermi gas, when long-lived Li$_2$ molecules were observed.

When dealing with fermions, Fano-Feshbach resonances are the tools we are mostly interested in, because the largest part of recent experimental achievements have been obtained via the tuning of the scattering length. This scattering length tuning procedure indeed admits to shift the system continuously from a weakly interacting regime, where fermions have a weak and long-range binding, to a strongly interacting regime where pairs of fermions behave like bosons.

1.2.1 BCS superfluidity and BEC-BCS crossover

We focus now on ultracold fermionic atoms whose interactions are controlled and tuned according to the Fano-Feshbach protocol we just described. As we remarked earlier, the free ideal Fermi gas ground state, obtained by piling up fermions into single-particle states, is unstable in presence of arbitrarily weak interactions. The BCS theory predicts a new ground state which is composed by pairs of fermions. When these fermions are close enough they can be seen as a system of molecules that behave like bosons and thus undergo Bose-Einstein condensation. Though, as

pointed out by Schrieffer, the BCS Cooper pair cannot truly form a Bose-Einstein condensation since it doesn't obey, within the BCS theory, the bosonic statistics, also when coupled. Roughly speaking, after a Bogoliubov transformation the creation/annihilation operators of the free ideal Fermi gas become quasi-particles creation/annihilation operators, but the commutators of the Cooper pair operators do not fully verify the bosonic commutation rules. The physics involved in this transition process, from weakly to strongly interacting fermions can be studied experimentally using the Fano-Feshbach resonance and qualitatively can be understood from Figure 1.3. The idea of invoking some sort of BEC to understand superconductivity
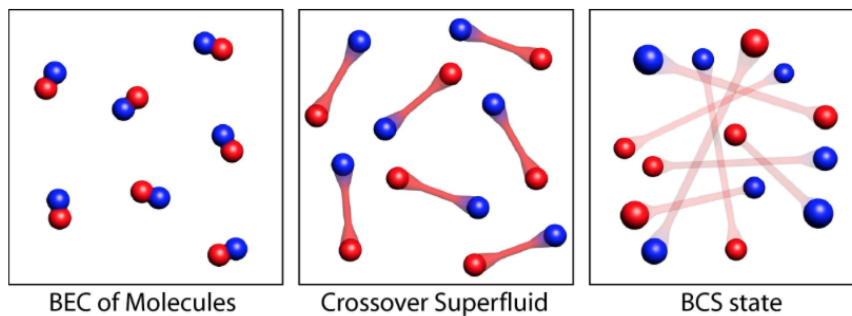
Figure 1.3: *The BEC-BCS crossover. By tuning the interaction strength between the two fermionic spin states, one can smoothly cross over from a regime of tightly bound molecules to a regime of long-range Cooper pairs, whose characteristic size is much larger than the inter-particle spacing. In between these two extremes, one encounters an intermediate regime where the pair size is comparable to the inter-particle spacing. From [29]*

is dating back to Schafroth et al. [30]. Also Eagles [31] studied superconductivity in doped semiconductors like $SrTiO_3$ with a very low carrier density, where the attraction between electrons need not to be small compared with the Fermi energy. This led to the first mean-field treatment of the BCS-BEC crossover. Independently, Leggett [32] addressed the problem of the BCS-BEC crossover in a dilute gas of fermions at $T = 0$ motivated by superfluid ^{3}He. Although ^{3}He is very much in the BCS limit, Leggett wanted to understand the extent to which some of its properties, such as the total angular momentum of the superfluid, might be similar to that of a BEC of diatomic molecules. A finite temperature analysis of the BCS-BEC crossover, along with the evolution of the critical temperature was first presented by Nozières and Schmitt-Rink (NSR) [33]. With the discovery of high temperature superconductors in 1986 and the realisation that the pair size is only slightly larger than the average inter-particle spacing, there was a resurgence of interest in the BCS-BEC crossover.

Since the BCS-BEC crossover is the backbone of our thesis work we will devote Chapter 2 to introduce all its features but it is worth outlining its MF interpretation here. As pointed out by Cooper, in presence of a Fermi surface, a tiny attractive

interaction makes the ideal Fermi gas ground state energetically unfavourable. A new ground state is reached and the dispersion relation of the new ground state quasi-particle components, the Cooper pairs, is characterised by a gap in the density of states between the Cooper pairs bulk and the excited states: such separation is called the energy gap. In a broader sense, pairs of fermions are thought as interacting through an auxiliary bosonic field that plays the role of phase transition order parameter, from a phase diagram region where the normal Fermi gas is favourable to one where the Cooper pair ground state has lower energy. At the mean-field level the auxiliary field is approximated to an uniform constant parameter.

The BCS-BEC crossover order parameter has been investigated through various techniques, at the MF level, beyond MF and via non-perturbative numerical approaches, such as quantum Monte Carlo. Moreover, the BCS-BEC crossover concept has been studied in low-dimensions, where the superfluidity experiences disruptive interplay of beyond MF contributions and/or spin-population imbalance. It is known that the BCS superfluid ground state cannot support a two-component spin mixture when the populations are not equally balanced in the two components. In this case, the system either forms two coexisting phases, a superfluid phase and a normal phase or it is expected to display exotic superfluid phases [34]. Moreover, at the BCS-BEC crossover, particles which experience p-wave interactions might display topological phase transitions [35]. Finally, the experimental realisation of the BCS-BEC crossover appears to be very sensitive to dimensionality and the interplay between inter-particle interaction and low-dimensionality is to be understood.

1.3 Research outline

As the thesis title suggests we will address the superfluid phase of Fermi gases in lower dimensionality, in particular in two dimensions. We move in two different directions: (1) the exotic superfluid phases that can be obtained when the spin-populations are moved away from the balanced conditions and (2) the interplay of interaction and dimensionality. Firstly, we remark that the theoretical and computational models increase in richness while we proceed through the chapters and will allow, when possible, a more accurate description of the superfluid phase phenomena. The following section aims to describe the specific topics we addressed according with the order they appear in the thesis.

1.3.1 Exotic superconducting states

Chapter 3 is devoted to the FFLO exotic superfluid phase in a low dimensional Fermi gas. The presence of an external magnetic field in gases, a microwave sweeper,

which is a microwave drive [36], between two different (pseudo-)spin populations can lead to two Fermi surfaces of different spin populations as in regular superconductors, which don't overlap. This is a simple and naturally occurring example of an imbalanced mixture of a two-spin populations system. The BCS theory, in the grand-canonical ensemble, at the mean field level, doesn't allow a good description of a unique superfluid phase. In fact a coexistence of two different phases has to be taken into account [34]. Namely, when the chemical potentials associated with different spin populations are different, it is impossible to find both a finite energy gap and a finite particle density polarisation. In fact, the difference of the chemical potentials, $\delta\mu = (\mu_\uparrow - \mu_\downarrow)/2$, where $\uparrow, \downarrow$ are labelling the (pseudo-)spin state, doesn't correspond to a population imbalance but to the repulsion of an external magnetic field. However, in the canonical ensemble, the imbalance of spin populations is not a problem by itself when undergoing a phase transition from a normal state to a superfluid BCS phase. The superfluid state may just discard the amount of particles that provide the imbalanced fraction by leaving them in the normal phase and will undergo a superfluid phase with the remaining balanced populations (see Fig. 1.4). It turns out that the favourable configuration, i.e. the state occupancy distribution with lower total free energy, is given by a spatially non-uniform gap parameter.

A family of exotic phases and spatially dependent order parameters was theoretically introduced by Fulde and Ferrell (FF) [37] in 1964, but also independently by Larkin and Ovchinnikov (LO) [38] in the same year. They showed that, due to the not overlapping nature of Fermi surfaces in an imbalanced Fermi gas, the Cooper pairs with a non-vanishing centre-of-mass momentum leads to a favourable energetic configuration with respect to both the normal phase and the BCS phase. A large variety of studies is devoted to this topic for many different reasons: the FFLO phase may explain some features of high transition temperature superconductors [39–42]. It could also give another point of view on the BEC-BCS crossover [43, 44] because of its possible interplay with the Berezinskii-Kosterlitz-Thouless transition specialised in 2D [45, 46].

Fulde and Ferrell proposed to model the spatial dependence of the pairing gap with a plane wave. Instead, Larkin and Ovchinnikob proposed a double plane wave with the same momentum going in opposite direction, i.e. a cosine function. In general we can refer to the FFLO family as any choice that describes an order parameter like

$$\Delta_{\text{FFLO}}(\mathbf{x}) = \sum_{\mathbf{q}\in\mathbb{Z}^\nu} \Delta_{\mathbf{q}}\, e^{i\mathbf{q}\cdot\mathbf{x}} \tag{1.3}$$

where ν indicates the dimensionality of the system and $\mathbb{Z}^\nu$ declares $\mathbf{q}$ to be a discrete momentum of the free Hamiltonian. Hence, for a box with the same edges L, we have $\mathbf{q} = \frac{2\pi}{L}(n_1, \ldots, n_\nu)$ with $n_i \in \mathbb{Z}$. It can easily be understood that no analytical
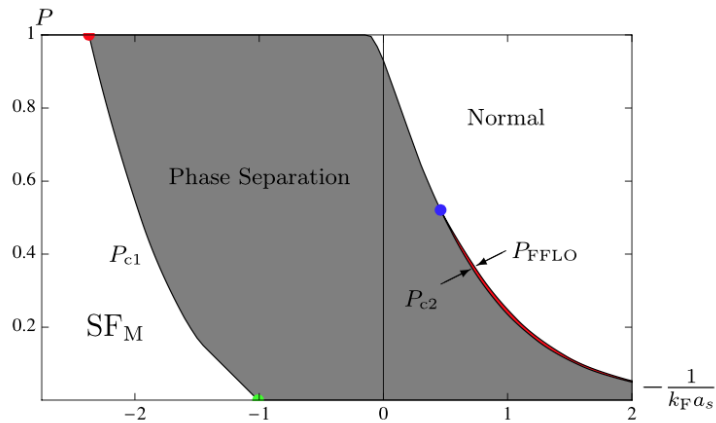
Figure 1.4: *The phase diagram of the FFLO exotic phase. The parameters are $-(k_F a_s)^{-1}$, the interaction strength tuning parameter, in 3D, with Fermi momentum k_F and scattering length a_s, and the difference of particle densities, $P = n_\uparrow - n_\downarrow$, of the two spin population. The phase separation allows the coexistence of BCS and normal phas, while the tiny red region is reserved to the FFLO phase. From [44].*

solution without specific choices of $\mathbf{q}$ can be computed. With the FF choice (single fixed $\mathbf{q}$ and constant $\Delta_{\mathbf{q}} = \Delta_0$), the form of the order parameter allows analytic calculations and it is used to describe the areas of the phase diagram that should be occupied by a generic FFLO phase (see Fig. 1.4). The LO ansatz instead often leads to computational complexity but it has been proven to be more stable and even favourable with respect to the FF counterpart. From Fig. 1.4, it is also straightforward to notice that the FFLO region, for 3D gases is expected to be available in a weakly interacting regime, not too close to the BEC-BCS crossover. Unfortunately, the window of imbalance needed to probe the FFLO phase is extremely narrow. However, the situation in low dimensions opens the possibility of probing a similar phase diagram, but with a larger region associated with the FFLO phase due to Fermi surface nesting [47, 48].

According to [47], it has been proved that in 1D the FFLO region is, in percentage, spanning a wider region in the phase diagram and we dedicate Chapter 3 to address the FFLO phase for 2D Fermi gases. We show how a generic FFLO family has lower energy configurations than the BCS ground state and discuss the signature of FFLO phases. The results are summarised in a published paper [49].

1.3.2 The interplay of dimensionality and interactions

Chapter 4 is devoted to the dimensional crossover of a trapped strongly-interacting Fermi gas. The experimental realisation of an ultracold Fermi gas, by sympathetic cooling with a bosonic atomic species, requires a confinement. The ideal Fermi gas,

i.e. a collection of non-interacting fermionic particles with an intrinsic (pseudo-)spin, is a good zeroth-order approximation that encapsulates the Pauli exclusion principles. The interplay of such system with a trapping potential turns out to be, as well, easy to handle from both the theoretical and experimental point of view. It is possible to maintain an ultracold gas inside a volume bound by harmonic oscillators and study the ideal Fermi gas in this new scenario. The physical properties of the ultracold gas however are strongly modified when we consider interacting particles. As we described before, a Fano-Feshbach resonance can be employed in order to control the interaction strength between pair of particles and allows, via an external magnetic field, to address the investigation of different interacting regimes. This setup represents an experimental realisation of the BCS-BEC crossover of a trapped ultracold fermionic gas.

We can identify, for each direction in the 3D space, a set of frequencies $\{\omega_x, \omega_y, \omega_z\}$ that regulate the harmonic traps. In particular each particle in the system will be experiencing a trapping potential given by

$$V(\mathbf{x}) = \frac{1}{2}m\left(\omega_x^2 x^2 + \omega_y^2 y^2 + \omega_z^2 z^2\right) \tag{1.4}$$

where m is the mass of the fermionic particle. This framework allows us to introduce a dimensionless parameter called aspect ratio, $\lambda = \omega_z/\omega_\rho$, by fixing $\omega_\rho = \omega_x = \omega_y$. The single particle picture suggests that when λ is large, i.e. $\omega_z \gg \omega_\rho$, the separation between the harmonic oscillator states, in the z or axial direction,

$$E_n = \hbar\omega_z\left(n + \frac{1}{2}\right), \tag{1.5}$$

for each natural number n, requires a large amount of energy to axially transfer particles from a state to the other. When the temperature of the experimental apparatus is low and in particular

$$k_B T \ll \frac{\hbar\omega_z}{2}, \tag{1.6}$$

the fermionic gas is confined to the axial harmonic oscillator ground state. Indeed a thermal fluctuation doesn't possess enough energy to send particles into excited states in the axial direction. The result of this confinement scheme, as pictured in Fig. 1.5, is a quantum system which is allowed to displace its dynamics only in the transverse directions, namely x and y. This confinement system has been experimentally tested s [51] and led to a better understanding of the criterion that separates the two- and three-dimensional regimes beyond the single particle picture previously described. It is expected, when the particles are interacting, that a slight modification of the Hamiltonian spectrum will occur. Thus by observing the ratio between the particle density and the expected 2D particle density, an experimental
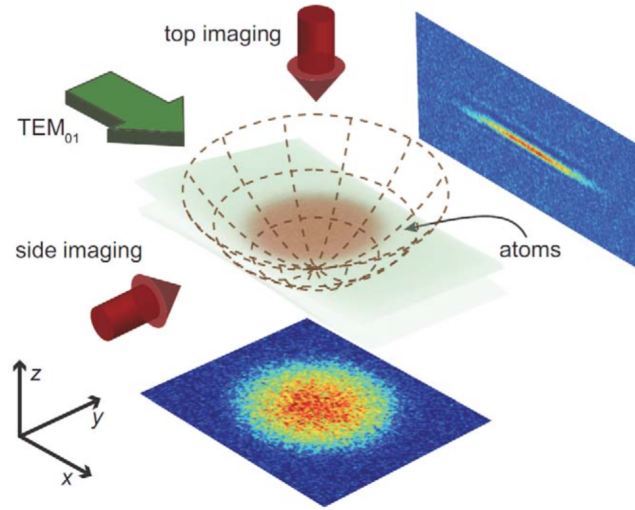
Figure 1.5: *Tightly confinement of an atomic cloud via harmonic trapping. The dashed parabola represents the transverse confinement ω_ρ along x and y while the axial trap has higher frequency. The result is a low dimensional system which lies on the ground state of the axial confinement. From [50].*

criterion for the dimensional transition can be obtained. From the theoretical point of view, instead, it is not so simple to go beyond the mean-field treatment for harmonically confined systems, mainly due to the non-uniformity of the particle density. Moreover, the listed criteria do not contain information about the interplay of the BCS-BEC crossover and the dimensionality. In fact, when we approach a 2D regime we expect the interaction picture to radically shift with respect to its 3D counterpart. This is due to the need of mapping the 3D scattering length, which regulates the Fano-Feshbach resonance in 3D, onto the interaction parameter in 2D, which contains a logarithm (see Chap. 2).

Due to the interests of the scientific community [51–65] and, in particular, of our experimental research group at Swinburne [50, 66], we addressed the theoretical study of the criterion required for a Fermi gas, prepared in a confined chamber, in order to reach a true 2D dimensionality. Despite most of the experiments deal with this problem in a harmonically trapped setup, we overtake the disadvantage of a globally non-uniform particle density with an alternative confining scheme [67]. Recently, it has been shown that it is possible to confine ultracold gases within hard walls (see Fig. 1.6) such that, away from the traps boundaries, the system appears to be uniform in density [68].

Utilizing a periodic boundary conditions (PBC) ansatz we characterise the dimensional crossover between a 3D and a 2D Fermi gas. The periodicity on the boundaries allows a straightforward extension beyond the mean field theory on such
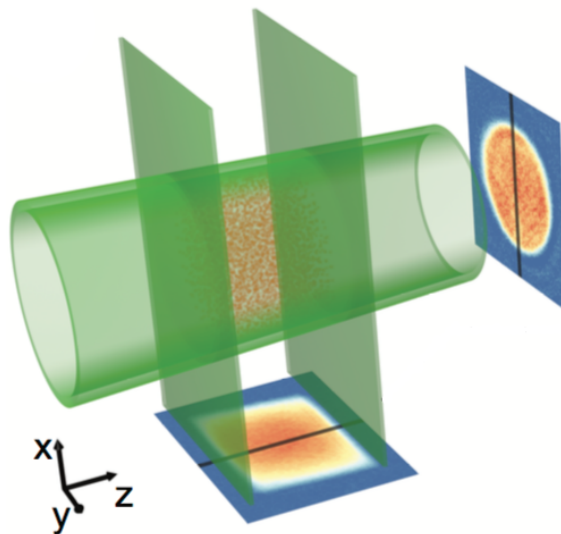
Figure 1.6: *The transverse direction is confined by hard walls that allow the particle density to be almost uniform when away from the boundaries. This setup can be theoretically treated with Gaussian pair fluctuations in the central region of the trapped gas. From [68].*

confined system and describes some experimental features that can be employed to mark the signature of the dimensional crossover, i.e. the continuous change of dimensionality from three- to two-dimensions. We extract the thermodynamic quantities, such as the chemical potential and the superfluid order parameter, that describe the BCS-BEC crossover phase diagram. We introduce a criterion to keep track of the BCS-BEC crossover evolution while the dimensionality is modified and we describe an experimental protocol to observe the transition amongst different dimensional regimes. The study is summarised in a published article [67].

1.3.3   The breathing mode frequency of a confined Fermi gas

The last contribution to this thesis is the study, in low dimensionality of the so-called "quantum anomaly" associated with the breathing mode frequency of a confined Fermi gas. In general, we refer to a quantum anomaly when a classical symmetry of a given system is broken during the process of quantisation of the theory, namely when we correct the Fourier spectrum of the Hamiltonian according to a renormalisation scheme.

Let's consider a scale invariant Hamiltonian and its Schrödinger equation for a single particle,

$$\left(-\frac{\hbar^2}{2m}\nabla_{\mathbf{x}}^2 + V(\mathbf{x})\right)\psi(\mathbf{x}) = E\psi(\mathbf{x}) \tag{1.7}$$

where the dimensionality is not fixed, V represents the external potential, ψ is the wave function with energy eigenvalue E. A scale invariance is a mapping $\mathbf{x} \mapsto \lambda \mathbf{x}$ with $\lambda > 0$ and the potential must either be $V(\mathbf{x}) \propto \delta(\mathbf{x})$ in two-dimensions, or $V(\mathbf{x}) \propto |\mathbf{x}|^{-2}$. In this case it can be manifested that $\tilde{\psi}(\mathbf{x}) = \lambda^{-2}\psi(\mathbf{x})$ is again solution of the Schrödinger equation with eigenvalue $\tilde{E} = \lambda^2 E$. This feature in the theory of unbounded linear operators is referred to as a failure in the symmetry of the Hamiltonian operator (which implies a failure in self-adjointness). The procedure of renormalisation allows the selection of a self-adjoint extension that returns a real valued energy spectrum.

This scale invariance, in many body problems can be obtained with a broader variety of potentials and in particular [69, 70] it is interesting to consider an interacting many body Hamiltonian in a first quantised fashion

$$\mathcal{H}_0 = -\sum_i \frac{\hbar^2}{2m_i} \nabla^2_{\mathbf{x}_i} + \sum_{i,j>i} V(\mathbf{x}_i - \mathbf{x}_j) \tag{1.8}$$

and to break the scale invariance with a confining harmonic trap

$$\mathcal{H}_{\mathrm{pot}} = \sum_i \frac{1}{2} m_i \omega^2 |\mathbf{x}_i|^2. \tag{1.9}$$

When we consider equal masses for each particle, a dilation operator appears

$$[\mathcal{H}_0, \mathcal{H}_{\mathrm{pot}}] = \mathrm{i}\omega^2 Q \qquad Q = -\frac{\mathrm{i}}{2} \sum_i (\nabla_{\mathbf{x}_i} \cdot \mathbf{x}_i + \mathbf{x}_i \cdot \nabla_{\mathbf{x}_i}) \tag{1.10}$$

Then it is possible to construct ladder operators $L^{\pm}$ to solve the spectrum of the Hamiltonian and any perturbation in time of the external harmonic oscillator trap will de-phase such ladder operator by [69]

$$L^{\pm}(t) = e^{\mp \mathrm{i}2\omega t} L^{\pm}. \tag{1.11}$$

The operator associated with the displacement of particles, in time, now averages to a stationary quantity, I_0, plus an extra oscillatory term which can be explicitly computed in the case when the internal interaction V has a λ^{-2}-type scale invariance. In particular one can show that

$$\left\langle \sum_i |\mathbf{x}_i(t)|^2 \right\rangle = I_0 + A\cos(2\omega t + \phi). \tag{1.12}$$

The appearance of a constant frequency of oscillation, 2ω, which is twice the frequency of by the confinement is a marker of a hidden symmetry in the system associated with the Lorentz group of boosts and rotation in dimension $2 + 1$ (2 spatial $+$ 1 time). The oscillation in the displacement field is usually referred to as

breathing mode. Such a symmetry though is not expected to survive in a context in which the interaction has to undergo a renormalisation procedure. In the case of ultracold diluted Fermi gases, when we have perfect balance of two-spin populations we know that a good model for interactions is given by a contact potential $gV(\mathbf{x})$. In three-dimensions the contact potential suffers from non self-adjointness, which doesn't imply a symmetry failure. Thus it requires only a so-called ultraviolet renormalisation.

In two-dimensions, the contact interaction amongst particles suffers from a ultraviolet divergence but, more important, also from a symmetry failure. It was realised that the contact potential in 2D doesn't actually scatter particles. Namely, for small incoming momentum the scattering cross-section tends to disappear. In order to make it scatter we introduce a bound state ε_B which, upon quantisation, removes the symmetry failure and hence the exact relation, $\omega_B = 2\omega$, between breathing mode frequency and harmonic trapping frequency is violated. Hence upon quantisation, the deviation $\delta\omega = (\omega - \omega_B)/\omega_B$ is a marker of the quantum anomaly. Since the seminal work done by Johannes Hofmann [71] we expect, in two dimensions, to detect a deviation of the breathing mode frequency around $\log(k_F^{2D} a_{2D}) \sim 0$, where k_F^{2D} is the 2D Fermi momentum and a_{2D} the 2D scattering length introduced upon quantisation to renormalise the contact potential. Since the experimental observation of this phenomenon is achieved in a quasi-2D environment, by squeezing the axial harmonic trap, we address in Chapter 5, the interplay of the quantum anomaly with the dimensional crossover scheme of Chapter 4. We study the breathing mode frequency as a function of both the interaction strength between a pair of particles and the dimensionality intrinsic to the system. The resulting picture may be of extreme help to the large experimental community which is addressing the problem nowadays. This study is summarised in a published paper [72].

Chapter 2

Ultracold Fermi gases

In this chapter we outline the theoretical models used to describe an interacting Fermi gas that undergoes extreme cooling, close to the absolute zero temperature (we mainly follow the first chapters of Ref. [73]). In particular we present here the field theoretical approach to the BCS theory of superconductivity [74], the framework for describing trapped gases and the Fano-Feshbach resonance which allows tunability of the interaction amongst fermions.

2.1   Fermi systems formalism

From the axioms of Quantum Mechanics we recall that a quantum system must allow the description of its dynamics by a self-adjoint operator bounded from below, the Hamiltonian, $\mathcal{H}$, which acts on a Hilbert space, $\mathfrak{H}$, of square summable functions, moreover let $(\cdot, \cdot)_{\mathfrak{H}}$ be its hermitian product. The single particle picture obtained from the Schrödinger equation anyway doesn't suit many-particle systems and/or systems in which the number of particles is free to vary.

It serves this second purpose the introduction of the Fock space of $\mathfrak{H}$, which is defined by steps as follows. We define for each $n \in \mathbb{N}$ the n-particle Hilbert space $\mathfrak{H}^{\otimes n}$, meaning the tensor product of n identical copies of $\mathfrak{H}$. When $n = 0$ we have $\mathfrak{H}^{\otimes 0} = \mathbb{C}$. Then a pre-Hilbert subspace is simply obtained as graded direct sum of the former objects

$$\mathfrak{F} = \bigoplus_{n \in \mathbb{N}} \mathfrak{H}^{\otimes n}. \tag{2.1}$$

The Fock space can be projected onto two very special subspaces, i.e. the symmetric and anti-symmetric sector. To do so we introduce two orthogonal self-adjoint

projectors by defining them on each $\mathfrak{H}^{\otimes n}$ as

$$P_+(f_1 \otimes \cdots \otimes f_n) = \frac{1}{n!} \sum_{\sigma \in \mathfrak{S}_n} f_{\sigma(1)} \otimes \cdots \otimes f_{\sigma(n)},$$

$$P_-(f_1 \otimes \cdots \otimes f_n) = \frac{1}{n!} \sum_{\sigma \in \mathfrak{S}_n} \varepsilon_\sigma f_{\sigma(1)} \otimes \cdots \otimes f_{\sigma(n)}, \tag{2.2}$$

where σ's are elements of $\mathfrak{S}_n$, the space of all permutations of n elements and ε_σ is the parity of the σ permutation. Hence the bosonic (+) and fermionic (−) sectors of the Fock space are given by

$$\mathfrak{F}_\pm = P_\pm (\mathfrak{F}) \tag{2.3}$$

where $P_\pm$ are extended by linearity on the whole Fock space.

Given any self-adjoint operator, $\mathcal{H}$, or any unitary operator, $\mathcal{U}$, defined over $\mathfrak{H}$, it is straightforward to extend them to the Fock space and, meanwhile, maintain their respective properties of self-adjointness and unitarity. The rules to obtain these new operators are given by

$$\mathcal{H}^{\mathfrak{F}_\pm} = \bigoplus_{n \in \mathbb{N}} \mathcal{H}_n \qquad \mathcal{H}_n(P_\pm(f_1 \otimes \cdots \otimes f_n)) = P_\pm \left(\sum_{i=1}^n f_1 \otimes \cdots \otimes \mathcal{H} f_i \otimes \cdots \otimes f_n \right), \tag{2.4}$$

and

$$\mathcal{U}^{\mathfrak{F}_\pm} = \bigoplus_{n \in \mathbb{N}} \mathcal{U}_n \qquad \mathcal{U}_n(P_\pm(f_1 \otimes \cdots \otimes f_n)) = P_\pm (\mathcal{U} f_1 \otimes \cdots \otimes \mathcal{U} f_n). \tag{2.5}$$

Finally, to describe the algebras of observables we apply to a many-body system, we are aided by the "creation" and "annihilation" operators. Being neither unitary nor self-adjoint, though one the adjoint of the other, we can follow a similar chain of definitions as we did previously. Let $f \in \mathfrak{H}$ a single-particle wave-function. Let $(\psi^{(n)})_n$ a Fock space vector, we define $a(f)\psi^{(0)} = 0$ and $a^*(f)\psi^{(0)} = f$, also

$$a(f)(f_1 \otimes \cdots \otimes f_n) = \sqrt{n}(f, f_1)_{\mathfrak{H}} f_2 \otimes \cdots \otimes f_n, \tag{2.6}$$

$$a^*(f)(f_1 \otimes \cdots \otimes f_n) = \sqrt{n+1} f \otimes f_1 \otimes \cdots \otimes f_n. \tag{2.7}$$

Since, for each $n \in \mathbb{N}$, we have $\psi^{(n)} \in \mathfrak{H}^{\otimes n}$, then $a(f)$ and $a^*(f)$ are defined by linear extension on the whole Fock space. Moreover the interplay between the creation/annihilation operators and the symmetric or anti-symmetric projectors leads to the rules

$$a_\pm(f) = a(f)P_\pm \qquad\qquad a_\pm^*(f) = P_\pm a^*(f) \tag{2.8}$$

where we defined the symmetrised (+) and anti-symmetrised (-) counterparts of the creation/annihilation operators. We will focus now on the fermionic sector only, or

the anti-symmetrised part, and we will set $\phi(f) = a(f)$ to simplify the notation. We observe that for each $f \in \mathfrak{H}$ we have

$$\phi^*(f)\phi^*(f) = 0 \tag{2.9}$$

which means we cannot create two fermions in the exact same state with wavefunction f. Moreover it is straightforward to prove that

$$\{\phi(f), \phi(g)\} = \{\phi^*(f), \phi^*(g)\} = 0 \qquad \{\phi(f), \phi^*(g)\} = (f, g)_{\mathfrak{H}} \mathbb{1} \tag{2.10}$$

where $\{\cdot, \cdot\}$ represents the anti-commutator of operators, namely $\{A, B\} = AB + BA$, also referred as canonical anti-commutation relations (CARs).

In the vast majority of cases, the Fock space formalism can be reduced to the Schrödinger representation, which sets $\mathfrak{H} = L^2(\mathbb{R}^\nu)$, being ν the spatial dimensionality of the system and the Hilbert space is given by the square-summable functions over $\mathbb{R}^\nu$. Let $(\psi^{(n)})_n$ be a (anti-symmetric) Fock space vector, then we have

$$(\phi(f)\psi)^{(n)}(x_1, \ldots, x_n) = \sqrt{n+1} \int_{\mathbb{R}^\nu} dx \overline{f(x)} \psi^{(n+1)}(x, x_1, \ldots, x_n) \tag{2.11}$$

and

$$(\phi^*(f)\psi)^{(n)}(x_1, \ldots, x_n) = \frac{1}{\sqrt{n}} \sum_{i=1}^n (-1)^{i-1} f(x_i) \psi^{(n-1)}(x_1, \ldots, \hat{x}_i, \ldots, x_n) \tag{2.12}$$

where each coordinate x_i belongs to $\mathbb{R}^\nu$ and $\hat{x}_i$ denotes a coordinate that has been omitted. The Lebesgue measure of the Hilbert space and the Riesz's theorem allow us to write each operator as a operator-valued distribution, namely we denote formally

$$\phi(f) = \int dx \overline{f(x)} \phi(x) \qquad \phi^*(f) = \int dx f(x) \phi^*(x) \tag{2.13}$$

through which it is possible to write most of the observables we use in the current theories. The simpler case of this class of operators described by operator-valued distributions is the particle number counter

$$N = \int dx \ \phi^*(x)\phi(x) \tag{2.14}$$

Another operator is the kinetic energy given by

$$K = \int dx \ \phi^*(x) \left(-\frac{\hbar^2}{2m} \nabla_x^2\right) \phi(x) \tag{2.15}$$

or the free grand-canonical Hamiltonian

$$H_0 = K - \mu N = \int dx \ \phi^*(x) \left(-\frac{\hbar^2}{2m} \nabla_x^2 - \mu \mathbb{1}\right) \phi(x) \tag{2.16}$$

We observe that the CARs become

$$\{\phi(x), \phi(y)\} = \{\phi^*(x), \phi^*(y)\} = 0 \qquad \{\phi(x), \phi^*(y)\} = \delta(x-y)\mathbb{1}. \qquad (2.17)$$

Given a self-adjoint single-particle Hamiltonian we can build the many-body counterpart, $\mathcal{H}$, which acts on the Fock space, as described above. A many-body quantum state is then described by all the expectations values on every observable A, weighted by the grand-canonical ensemble probability weight. Given an inverse temperature $\beta = (k_B T)^{-1}$ we have the β-state

$$\omega_\beta(A) = Z^{-1}\mathrm{Tr}(e^{-\beta\mathcal{H}}A) \qquad (2.18)$$

where we introduced the grand-canonical partition function,

$$Z = \mathrm{Tr}(e^{-\beta\mathcal{H}}) \qquad (2.19)$$

which returns the (grand-canonical) thermodynamic potential

$$\Omega = -\frac{1}{\beta}\log Z \qquad (2.20)$$

One can show that the ω_β states are Kubo-Martin-Schwinger (KMS) states, i.e. their two-point functions exhibit a peculiar periodicity when the time is analytically extended to the complex plane. For instance, if $\mathcal{H}$ doesn't depend explicitly on time, we can also define time-dependent creation/annihilation operators

$$\phi(x,t) = e^{-\mathrm{i}t\mathcal{H}/\hbar}\phi(x,0) \qquad (2.21)$$

and then the two-point correlation function

$$\omega_\beta(\phi(x,t)\phi(y,0)) = \frac{1}{Z}\mathrm{Tr}\left(e^{-\beta\mathcal{H}}\phi(x,t)\phi(y,0)\right) = \omega_\beta(\phi(y,-\mathrm{i}\beta)\phi(x,t)) \qquad (2.22)$$

thus we analytically extend t to a complex variable and we study it on the pure imaginary line $t \mapsto \tau = \mathrm{i}t$, which returns

$$\omega_\beta(\phi(x,\tau)\phi(y,0)) = \omega_\beta(\phi(y,\beta)\phi(x,\tau)) \qquad (2.23)$$

but the CARs then force the creation/annihilation operators to verify

$$\phi(x,0) = -\phi(x,\beta) \qquad (2.24)$$

This (anti-)periodic behaviour of the creation/annihilation operators allows a Wick rotation of the Hamiltonian that modifies the definition of the theory's action into

$$\mathscr{S}[\phi^*, \phi] = \int_0^\beta d\tau \int dx \left\{\phi^*(x,\tau)\hbar\partial_\tau\phi(x,\tau) + \mathcal{H}[\phi^*(x,\tau), \phi(x,\tau)]\right\} \qquad (2.25)$$

where $\mathcal{H}[\phi^*(x,\tau), \phi(x,\tau)]$ is the integral kernel of $\mathcal{H}$ and the partition function is now given by the integration on paths

$$Z = \int \mathcal{D}\phi^* \mathcal{D}\phi \; e^{-\mathscr{S}[\phi^*, \phi]/\hbar} \tag{2.26}$$

The easiest way to construct all the expectation values of the quantum state is to extend Z to a generating functional $Z[J, J*]$ that is given by

$$Z[J, J^*] = \int \mathcal{D}\phi^* \mathcal{D}\phi \; e^{-\mathscr{S}[\phi^*, \phi]/\hbar + \int_0^\beta d\tau \int dx \; (\phi^*(x,\tau)J(x,\tau) + \phi(x,\tau)J^*(x,\tau))} \tag{2.27}$$

then the functional derivatives

$$\frac{1}{Z} \left. \frac{\delta}{\delta J^*(x,\tau)} \right|_{J=0} Z[J, J^*] = \frac{1}{Z} \int \mathcal{D}\phi^* \mathcal{D}\phi \; \phi(x,\tau) e^{-\mathscr{S}[\phi^*, \phi]/\hbar} = \omega_\beta(\phi(x,\tau)) \tag{2.28}$$

are able to give a closed form to any observable that is given by an algebraic combination of the creation/annihilation operators. The computation of path integrals, according to the spin sector in which the system lives, can be done through various techniques. In the case of fermions, it is possible to introduce Grassmann variables to replace the operators. A Grassmann algebra is an algebra generated by anti-commuting elements.

The simplest case in which the Fock space formalism can be used analytically, through the integral in Eq. (2.26), is the study of a Fermi gas, with spin s, in which the particles are not interacting. It is well known that, in the case of the ideal Fermi gas, the thermodynamic quantities can be expressed as regular sums or integrals. In particular, if we require the spatial configurations to be constrained in a box of volume V instead of the whole $\mathbb{R}^n$, we perform the Fourier transform $\mathscr{F}$ on the operator H_0 and we have

$$\hat{H}_0 = \mathscr{F} H_0 \mathscr{F}^{-1} = \frac{1}{V} \sum_{\mathbf{k},\sigma} (\varepsilon_{\mathbf{k}} - \mu_\sigma) a^*_{\sigma\mathbf{k}} a_{\sigma\mathbf{k}} \tag{2.29}$$

where the σ label introduces the s spin degeneracy and $\varepsilon_{\mathbf{k}} = \hbar^2 |\mathbf{k}|^2 / (2m)$. The thermodynamic potential then assumes the closed form

$$\Omega_0 = -\frac{1}{\beta} \sum_{\sigma, \mathbf{k}} \log \left(1 + e^{-\beta(\varepsilon_{\mathbf{k}} - \mu_\sigma)} \right) \tag{2.30}$$

Despite the Fock space method works well in the ideal case, the truth is that it doesn't help when we attempt treating more complicated cases, namely when the interaction is turned on. To overtake these limitations we move to a path integral formalism which employs a recombination of spinorial fields via an auxiliary bosonic field.

2.2   Field theory formalism for the BCS theory

We introduce in this section the BCS theory viewed from the point of view of quantum fields. The many body Hamiltonian is given by the kinetic energy and a simple contact interaction. We address the description of a Fermi gas with two spin components that interact via a contact potential. Since it will be useful to address both the two- and three-dimensional case we will keep the notation as generic as possible and we will remark where the dimensionality comes into play in the description of the dynamics of the systems. The field theoretical approach allows also to treat the mean-field level and beyond mean-field level through the same formalism.

When the fermionic mixtures of particles is kept at low temperature and we can consider a diluted regime, i.e. the inter-particle distance is larger compared to the de Broglie thermal wavelength, the particles are forced to interact through an *s*-wave scattering channel. This simplification brings several advantages. Firstly, a single scattering length is enough to describe the interacting regime, whether it is repulsive, weakly-attractive or strongly-attractive. Secondly, we want to model an experimental setup in which the interacting regime is tuned by a Fano-Feshbach resonance. That means an external magnetic field is directly responsible of the tuning of the *s*-wave scattering length.

Finally, we expect the experimental system to possess two spin states only. Experimentally this is realised by forcing the particles in two hyperfine levels. By doing so a microwave sweeper is often employed to balance or imbalance the spin populations. Such imbalance is controlled in the Hamiltonian by the presence of two chemical potentials which can be set equal in case of perfect population balance. We will address an imbalanced case when addressing the Fulde-Ferrell superfluid phase in Chapter 3.

We label the selected two (pseudo-)spin states of the system as $\uparrow$ and $\downarrow$, then the Hamiltonian of the system, in terms of the creation/annihilation operators of the fermionic fields is given by

$$
\begin{aligned}
\mathcal{H} = \int dx \sum_{\sigma=\uparrow,\downarrow} \phi_\sigma^*(x) \left(-\frac{\hbar^2}{2m_\sigma} \nabla_x^2 - \mu_\sigma \right) \phi_\sigma(x) \\
+ \sum_{\sigma,\sigma'=\uparrow,\downarrow} \int dx dx' \ \phi_\sigma^*(x)\phi_{\sigma'}^*(x')V_{\sigma,\sigma'}(x-x')\phi_{\sigma'}(x')\phi_\sigma(x)
\end{aligned}
\tag{2.31}
$$

where the integration is, according to the case, wither two- or three-dimensional. The potential is modelled as a contact interaction, hence we can write

$$
V_{\sigma,\sigma'}(x-x') = \frac{g}{2}\delta_{\sigma,\bar{\sigma}'}\delta(x-x')
\tag{2.32}
$$

where $\bar{\sigma}'$ is the opposite spin of σ', thus we obtain

$$\mathcal{H} = \int dx \sum_{\sigma=\uparrow,\downarrow} \phi_\sigma^*(x) \left(-\frac{\hbar^2}{2m_\sigma} \nabla_x^2 - \mu_\sigma \right) \phi_\sigma(x) + g \int dx \, \phi_\uparrow^*(x)\phi_\downarrow^*(x)\phi_\downarrow(x)\phi_\uparrow(x) \tag{2.33}$$

It is well known that the contact potential lacks of self-adjointness in both 2D and 3D, while in 2D only it displays a dilation symmetry. This latter symmetry is responsible for the introduction a 2D binding energy. First of all, in order to renormalise the interaction potential we introduce the two-body T-matrix, obtained from the Lippmann-Schwinger equation

$$T_{2\mathrm{B}}^{-1}(E) = g^{-1} - \Pi(E) \tag{2.34}$$

where $\Pi(E)$ is the two-particle bubble, or equivalently the retarded Green's function of the two-body problem, which reads

$$\Pi(E) = \frac{1}{V} \sum_{\mathbf{k}} \frac{1}{E + \mathrm{i}\varepsilon - 2\varepsilon_{\mathbf{k}}}. \tag{2.35}$$

The dimension is controlled by the sum over the components of $\mathbf{k}$ and the dispersion relation is set to $\varepsilon_{\mathbf{k}} = \hbar^2|\mathbf{k}|^2/(2m)$. The left hand-side, in the thermodynamic limit, for $V \to \infty$ of Eq. (2.34) must match the correct scattering amplitude $f(E) = 4\pi\hbar^2 T_{2\mathrm{B}}(E)/m$

$$f_{2\mathrm{D}}(E) = \frac{1}{\log(\varepsilon_B^{2\mathrm{D}}/E) + \mathrm{i}\pi} \qquad\qquad f_{3\mathrm{D}}(E) = \frac{1}{a_{3\mathrm{D}}^{-1} + \mathrm{i}\sqrt{2mE/\hbar^2}} \tag{2.36}$$

where we introduced, in 2D the binding energy of the contact potential bound state $\varepsilon_B^{2\mathrm{D}}$ and, in 3D, the 3D s-wave scattering length $a_{3\mathrm{D}}$. Since the integral in Eq. (2.35) is divergent in both 2D and 3D, we need to balance it with the magnitude of g which becomes

$$g_{2\mathrm{D}}^{-1} = -\frac{1}{V} \sum_{\mathbf{k}} \frac{1}{2\varepsilon_{\mathbf{k}} + \varepsilon_B^{2\mathrm{D}}} \qquad\qquad g_{3\mathrm{D}}^{-1} = \frac{m}{4\pi\hbar^2 a_{3\mathrm{D}}} - \frac{1}{V} \sum_{\mathbf{k}} \frac{1}{2\varepsilon_{\mathbf{k}}}. \tag{2.37}$$

In order to solve the partition function, Z, according to Eq. (2.25) and Eq. (2.26), we plug the Hamiltonian (2.33) in the action

$$\frac{\mathscr{S}[\phi^*,\phi]}{\hbar} = \int_0^\beta d\tau \int dx \sum_\sigma \phi_\sigma^* \partial_\tau \phi_\sigma + \int_0^\beta d\tau \mathcal{H}[\phi^*,\phi] \tag{2.38}$$

and we introduce the bosonic pairing field $\Phi(x) = g\phi_\downarrow(x)\phi_\uparrow(x)$. We can also re-organise the fermionic fields into Nambu-Gor'kov spinors by setting

$$\psi^* = \begin{pmatrix} \phi_\uparrow^* & \phi_\downarrow \end{pmatrix} \qquad\qquad \psi = \begin{pmatrix} \phi_\uparrow \\ \phi_\downarrow^* \end{pmatrix} \tag{2.39}$$

The Hubbard-Stratonovich transformation modifies the partition function into

$$Z = \int \mathcal{D}\psi^* \mathcal{D}\psi \mathcal{D}\Phi^* \mathcal{D}\Phi \; e^{-\mathscr{S}[\psi^*, \psi, \Phi^*, \Phi]/\hbar} \tag{2.40}$$

with action

$$\mathscr{S}[\psi^*, \psi, \Phi^*, \Phi] = -\int dx \frac{|\Phi(x)|^2}{g} - \int dx dx' \; \psi^*(x) \mathbb{G}^{-1}(x, x')\psi(x'). \tag{2.41}$$

The operator-valued distribution spinorial Green's function assumes the form

$$\mathbb{G}^{-1}(x, x') = \delta(x - x') \begin{pmatrix} -\partial_\tau + \frac{\hbar^2 \nabla_x^2}{2m} + \mu \mathbb{1} & \Phi(x) \\ \Phi^*(x) & -\partial_\tau - \frac{\hbar^2 \nabla_x^2}{2m} - \mu \mathbb{1} \end{pmatrix} \tag{2.42}$$

and the Nambu-Gor'kov spinors now present themselves in Gaussian integral form. By considering a Grassmann algebra formed by such spinors as Grassmann variables we can perform the path integral analytically and obtain an effective action which depends on the bosonic pairing field only

$$\mathscr{S}[\Phi^*, \Phi] = -\int dx \frac{|\Phi(x)|^2}{g} - \mathrm{Tr}[\log \mathbb{G}^{-1}] \tag{2.43}$$

2.2.1 BCS mean-field theory

We can now proceed to simplify the bosonic pairing field. The prescription for the BCS mean-field theory is to consider the pairing as a constant field. In this case it represents the energy gap that the Cooper pairs onto the Fermi surface have to overcome in order to reach excited states outside the superfluid fraction. Namely, this amounts to

$$\Phi(x) = \Delta \mathbb{1}. \tag{2.44}$$

We will see in Chapter 3 that it is interesting to consider the bosonic pairing field as a non-uniform classic field by enforcing a dependency on a spatial coordinate. Anyway the BCS theory with constant gap parameter allows a very simple form for the partition function due to the fact that the measures $\mathcal{D}\Phi^* \mathcal{D}\Phi$ are now regular Lebesgue measures. We obtain the grand-canonical thermodynamic potential, at the mean-field level as

$$\Omega_{\mathrm{MF}} = -\frac{\Delta^2}{g} - \frac{1}{\beta V} \sum_{\mathrm{i} k_n, \mathbf{k}} \log\{\det[\beta G^{-1}(\mathrm{i} k_n, \mathbf{k})]\} + \frac{1}{V} \sum_{\mathbf{k}} \xi_{\mathbf{k}} \tag{2.45}$$

where the Fourier transform of the spinorial Green's function reads,

$$G^{-1}(\mathrm{i} k_n, \mathbf{k}) = \begin{pmatrix} \mathrm{i} k_n - \xi_{\mathbf{k}} & \Delta \\ \Delta & \mathrm{i} k_n + \xi_{\mathbf{k}} \end{pmatrix}. \tag{2.46}$$

We introduce some very useful notation here. The Matsubara frequencies, which correspond to the Fourier mode in the imaginary time space, are written as $k_n = (2n+1)\pi/\beta$ for each $n \in \mathbb{Z}$. The resulting inverse Fourier transform, in imaginary time, is then anti-periodic with period β. Moreover we introduce the shifted dispersion relation $\xi_\mathbf{k} = \varepsilon_\mathbf{k} - \mu$ and the BCS dispersion relation $E_\mathbf{k} = \sqrt{\xi_\mathbf{k} + \Delta^2}$. Finally we ask the pairing gap to assume only real values such a way it is the complex conjugate of itself. We thus obtain

$$\Omega_{\mathrm{MF}} = -\frac{\Delta^2}{g} + \frac{1}{V} \sum_\mathbf{k} (\xi_\mathbf{k} - E_\mathbf{k}) \tag{2.47}$$

when at zero temperature we set $\beta \to \infty$ and we exchange the sum $\beta^{-1} \sum_{\mathrm{i}k_n}$ with the integral $(2\pi)^{-1} \int d\omega$ being ω the analytically continued variable associated with $\mathrm{i}k_n$. It is very simple to compute the particle density which can be inferred from the thermodynamic potential as

$$n_{\mathrm{MF}} = -\frac{d\Omega_{\mathrm{MF}}}{d\mu} = \frac{1}{V} \sum_\mathbf{k} \left(1 - \frac{\xi_\mathbf{k}}{E_\mathbf{k}} \right) \tag{2.48}$$

By explicitly minimising the thermodynamic potential is also important to remind that the gap equation can be written as

$$0 = \frac{\partial \Omega_{\mathrm{MF}}}{\partial \Delta} = 2\Delta \left(\frac{1}{g} + \frac{1}{V} \sum_\mathbf{k} \frac{1}{2E_\mathbf{k}} \right) \tag{2.49}$$

which has trivial solutions for $\Delta = 0$ and finite positive solutions when the content of the brackets goes to zero. The normal phase of the BCS theory, i.e. when there is no superfluidity, appears when the solution $\Delta = 0$ becomes more energetically favourable.

We will use the mean field approach across Chapters 3 and 4 by introducing also other computational methods such as the Bugoliubov-de Gennes equations and a hybrid dimensional scheme that allows to continuously span from three- to two-dimensional systems. Anyway the generic results, with periodic boundary conditions, where the momentum space assumes discrete values on a lattice, will turn out to be the starting point of all the results henceforth discussed.

2.2.2 Gaussian pair fluctuations theory

The BCS theory is well known to describe qualitatively well the BCS-BEC crossover for ultracold Fermi gases in three dimensions. As this remarkable result is obtained only with a crude mean field approach, we expect it to fail while describing low dimensional system. We already commented the disruptive role of

fluctuations and the Mermin-Wagner theorem which asserts the impossibility of breaking a continuous symmetry, in low dimensions, at finite temperature, and the arise of quasi-long range order parameters beneath the BKT temperature. To take into account such deviation from the mean-field results, we enrich the bosonic auxiliary field, introduced in Eq. (2.40), with a true bosonic oscillation around the mean-field pairing gap

$$\Phi(x) = \Delta \mathbb{1} + \chi(x). \tag{2.50}$$

In particular we discard all the terms in the action which are linearly depended on the fluctuation field χ and any term which is of order strictly greater than 2 in χ. The new effective action will return a mean-field and a Gaussian pair fluctuations component

$$\mathscr{S}[\Phi^*, \Phi] \sim \mathscr{S}_{\mathrm{MF}} + \mathscr{S}_{\mathrm{GPF}}[\chi^*, \chi] + \dots \tag{2.51}$$

where $\mathscr{S}_{\mathrm{MF}}$ is given by plugging Eq. (2.44) into Eq. (2.43) and the fluctuations part can be formally expanding the logarithm in Eq. (2.43)

$$\mathscr{S}_{\mathrm{GPF}}[\chi^*, \chi] = \frac{1}{2} \sum_Q \begin{pmatrix} \chi^*(Q) & \chi(-Q) \end{pmatrix} \mathbb{M}(Q) \begin{pmatrix} \chi(Q) \\ \chi^*(-Q) \end{pmatrix}. \tag{2.52}$$

where we are employing a multi-index notation $Q \equiv (\mathrm{i}\, q_l, \mathbf{q})$, $q_l = 2\pi l/\beta$ for each integer $l \in \mathbb{Z}$ and $\mathbf{q}$ a vector in $\mathbb{R}^2$ or $\mathbb{R}^3$, according with the selected dimensionality. The matrix $\mathbb{M}(Q)$ is thus given by components as

$$\mathbb{M}(Q) = \begin{pmatrix} \mathbb{M}_{11}(Q) & \mathbb{M}_{12}(Q) \\ \mathbb{M}_{21}(Q) & \mathbb{M}_{22}(Q) \end{pmatrix} \tag{2.53}$$

The entries of the matrix are second order functions of the spinorial Green's function from Eq. (2.46) and in particular we obtain

$$\mathbb{M}_{11}(\mathrm{i}\, q_l, \mathbf{q}) = \mathbb{M}_{22}(-\mathrm{i}\, q_l, \mathbf{q}) = -\frac{1}{g} + \frac{1}{\beta V} \sum_K [G_{11}(K + Q) G_{22}(K)] \tag{2.54}$$

$$\mathbb{M}_{12}(\mathrm{i}\, q_l, \mathbf{q}) = \mathbb{M}_{21}(\mathrm{i}\, q_l, \mathbf{q}) = \frac{1}{\beta V} \sum_K [G_{12}(K + Q) G_{12}(K)] \tag{2.55}$$

where a term G_{ij} represents the ij-th entry of G and the symmetry suggested by the previous equations can be inferred from the symmetries of the spinorial Green's function. The Matsubara sums in $\mathrm{i}\, k_l$ can be carried out and be obtained in compact form,

$$\mathbb{M}_{11}(\mathrm{i}\, q_l, \mathbf{q}) = -\frac{1}{g} + \frac{1}{V} \sum_{\mathbf{k}, k_z} \left(\frac{u_+^2 u_-^2}{\mathrm{i}\, q_\nu - E_+ - E_-} - \frac{v_+^2 v_-^2}{\mathrm{i}\, q_\nu + E_+ + E_-} \right) \tag{2.56}$$

$$\mathbb{M}_{12}(\mathrm{i}\, q_l, \mathbf{q}) = \frac{1}{V} \sum_{\mathbf{k}, k_z} \left(-\frac{u_+ u_- v_+ v_-}{\mathrm{i}\, q_\nu - E_+ - E_-} + \frac{u_+ u_- v_+ v_-}{\mathrm{i}\, q_\nu + E_+ + E_-} \right) \tag{2.57}$$

Here, we use the notations [75–77]

$$u_\pm^2 = 1 - v_\pm^2 = \frac{1}{2}\left(1 + \frac{\xi_\pm}{E_\pm}\right). \tag{2.58}$$

with

$$E_\pm = \sqrt{\xi_\pm^2 + \Delta^2} \qquad \xi_\pm \equiv \xi_{\mathbf{k}\pm\frac{\mathbf{q}}{2}} \tag{2.59}$$

The path integration in χ and χ^* can be formally solved and we obtain a direct characterisation of the thermodynamic potential correction beyond the mean field level which can be written compactly as

$$\Omega_{\mathrm{GPF}} = \frac{1}{2\beta V}\sum_Q \log[\det \mathbb{M}(Q)] \tag{2.60}$$

Although simple, the previous formula is only formal in the sense that it contains a diverging sum in the bosonic Matsubara frequencies, $\mathrm{i}\,q_l$. To obtain a physically convergent expression we need to regulate the pathologic part of $\mathbb{M}$, which is the entry 11 due to renormalised interaction strength g. A convergence factor is defined as

$$\mathbb{M}_{11}^C\left(\mathrm{i}\,q_l, \mathbf{q}\right) = \mathbb{M}_{22}^C\left(-\mathrm{i}\,q_l, \mathbf{q}\right) = -\frac{1}{g} + \frac{1}{V}\sum_{\mathbf{k}} \frac{u_+^2 u_-^2}{\mathrm{i}\,q_\nu - E_+ - E_-} \tag{2.61}$$

By mean of the gap equation (2.49) we can correct the interaction strength with the proper T-matrix

$$\mathbb{M}_{11}^C\left(Q\right) = \frac{1}{V}\sum_{\mathbf{k}}\left(\frac{u_+^2 u_-^2}{\mathrm{i}\,q_\nu - E_+ - E_-} + \frac{1}{2E_{\mathbf{k}}}\right) \tag{2.62}$$

Note that, we consider the case $T = 0$, or equivalently $\beta \to \infty$, which continuously maps the Matsubara frequencies on the imaginary line of the complex plane. We introduce a complex variable to integrate out the Matsubara frequencies and by a Wick rotation onto the real line we have, for a holomorphic generic function f

$$\frac{1}{\beta}\sum_{l\in\mathbb{Z}} f(\mathrm{i}\,q_l) \to \frac{1}{2\pi}\int_{\mathbb{R}} d\omega\, f(\omega) \tag{2.63}$$

which in the specific case returns

$$\Omega_{\mathrm{GPF}} = \frac{1}{V}\sum_{\mathbf{q}}\int_0^\infty \frac{d\omega}{2\pi}\log\left[\frac{\mathbb{M}_{11}\left(\mathrm{i}\,\omega, \mathbf{q}\right)\mathbb{M}_{22}\left(\mathrm{i}\,\omega, \mathbf{q}\right) - \mathbb{M}_{12}\left(\mathrm{i}\,\omega, \mathbf{q}\right)^2}{\mathbb{M}_{11}^C\left(\mathrm{i}\,\omega, \mathbf{q}\right)\mathbb{M}_{22}^C\left(\mathrm{i}\,\omega, \mathbf{q}\right)}\right] \tag{2.64}$$

One can show that the pairing gap Δ needs to satisfy the mean-field equation

$$\frac{\partial \Omega_{\mathrm{MF}}}{\partial \Delta} = 0 \tag{2.65}$$

in order to have the gapless Goldstone phonon excitation spectrum. The equation of state at the GPF level can be obtained from a correction to the mean field result of Eq. (2.48)

$$n = -\frac{d\Omega}{d\mu} = n_{\mathrm{MF}} - \frac{\partial\Omega_{\mathrm{GPF}}(\mu, \Delta)}{\partial\mu} - \frac{\partial\Omega_{\mathrm{GPF}}(\mu, \Delta)}{\partial\Delta}\frac{d\Delta(\mu)}{d\mu} \tag{2.66}$$

Chapter 3

The FFLO phase in a two-dimensional Fermi gas

Amongst the first theoretical attempts that dealt with imbalanced fermionic systems was proposed independently by P. Fulde and R. A. Ferrell [37] and by A. Larkin and Y. Ovchinnikov [38]. The resulting spatially inhomogeneous superfluid has since then been referred to as FFLO phases [34, 78]. The idea was to start from the Cooper solution of a fermionic pair over a Fermi surface and consider the case where fermions could have a finite net centre-of-mass momentum. This idea in the balanced case is energetically costly; it was pointed out by Cooper that finite net centre-of-mass momentum pairs are energetically unfavourable because of an increase of internal energy due to the pair drift velocity [15]. In the case of an imbalanced system, where the Fermi surfaces of different components do not fully overlap, the most favourable energetic configuration of the ground state is a spatially inhomogeneous order parameter, while the BCS prediction is a constant parameter. In practical experiments involving superconductors, the presence of an external magnetic field may lead to a polarized system that still is superfluid and eventually probe a superfluid state with a non-constant pairing gap parameter. Unfortunately, the required magnitude of these magnetic fields is too high and superconductivity is limited by orbital pair-breaking effects with much smaller upper critical fields than the regime under investigation [79].

The lack of clear-cut evidences of the FFLO phase can be explained by invoking the fragile nature of the FFLO phase due to the tiny assigned region in the phase diagram of a polarized Fermi gas and a very small bunch of stable configurations that the FFLO can display [80–82] . Various attempts to enhance the effects of an FFLO phase have been carried out both theoretically and experimentally. Following the idea of the Fermi surface nesting, the study of the FFLO family has been addressed in both one and two dimensions. The former has been theoretically dis-

cussed in a full one-dimensional space [47] and a suitable experimental setup has been investigated [83] providing new interesting hints for the FFLO phase observation and detection. In two dimensional systems the problem has been theoretically analysed testing the LO proposal [84], on square lattices [85], within both FF and LO theories, beyond the MF theory [45] including the FF ansatz only. Two dimensional Fermi gases can be approximated by squeezing a three dimensional gas along one direction and this scenario has nowadays a consolidated state of the art in experimental apparata [50, 60, 66]. Many theoretical results suggested however that the FF proposal is not the most energetically favourable choice and that the LO phase, although preferable to the FF one, could be enhanced.

For the sake of clarification we provide a summary of the definitions of the main cases in the FFLO family. The mean field theory and its consequent saddle point approximation requires us to study the average of the interaction subsidiary field that drives pair interactions. The standard Hubbard-Stratonovich transformation, performed on the contact potential Hamiltonian, provides the pairing field $\hat{\Delta}$. The saddle point approximation, averaging on the energetically favourable ground state, produces the pairing gap profile $\Delta(\mathbf{x})$ which is the order parameter for the superfluid transition. The BCS theory requires an order parameter that is constant, which in two-dimensions at zero temperature, for instance, is given by

$$\Delta_0(\mu) = \sqrt{\varepsilon_b(\varepsilon_b + 2\mu)} \tag{3.1}$$

where μ is the chemical potential and ε_b is the 2D contact potential binding energy that will be described later. The most generic ansatz for the order parameter can be stated as a Fourier transform of a space dependent function that is decomposed into plane waves or any complete orthonormal Hilbert basis. In this new frame the FF ansatz is given by $\Delta(\mathbf{x}) = \Delta_0 \exp(i\mathbf{Q} \cdot \mathbf{x})$ where Δ_0 is a constant parameter and $\mathbf{Q}$ plays the role of the Cooper pair center-of-mass non-vanishing momentum. Improving the form of the FF phase, Larkin and Ovchinnikov proposed the sum of two opposite plane waves with the same momentum $\Delta(\mathbf{x}) = \Delta_0 \cos(\mathbf{Q} \cdot \mathbf{x})$. It is pretty straightforward that, although we can justify sums of opposite plane waves with symmetry arguments, we cannot a-priori exclude that many different momenta might contribute to the definition of the inhomogeneous order parameter basically giving it the shape of a Fourier transform of a generic even function. A combination of these methods, generalization of the order parameter function and a lower dimensionality, could show a new path to probe the FFLO phases [49].
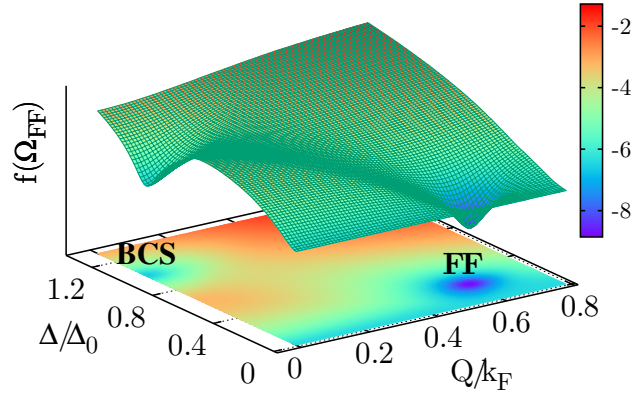
Figure 3.1: *Thermodynamic potential per particle for the FF ansatz in 2D. The appearance of the FF minimum indicates a first order phase transition with the BCS minimum while the transition with the partially polarized normal state is a second order one when the FF minimum merges with the free Fermi gas line ($\Delta = 0$). The z axis is smeared by a logarithmic function $f(x) = \log(1 + \alpha x/(2\pi N \varepsilon_F))$, with $\alpha = 9.916$ and N the number of particles, to enhance the FF absolute minimum. The FF phase depends on the frequency $Q = |\mathbf{Q}|$ and the order parameter amplitude Δ here scaled via the two-dimensional BCS constant order parameter Δ_0 in equation (3.1). Moreover we set $\mu = \varepsilon_F$ and $\varepsilon_b = 0.10\varepsilon_F$. From [49].*

3.1 The FFLO family

If we put the system in a box with side L and volume $V = L^\nu$, with an arbitrary dimension $\nu > 1$ that exhibits periodic boundary conditions, then the most generic order parameter is indeed the result of a Fourier transform over the discretised modes of the box

$$\Delta_{\text{FFLO}}(\mathbf{x}) = \sum_{\mathbf{Q}} \Delta_{\mathbf{Q}} \exp(\mathrm{i}\,\mathbf{Q} \cdot \mathbf{x}) \tag{3.2}$$

with $\mathbf{Q} \in \mathbb{Z}^\nu$, that is the FFLO family's order parameter. In this family many further approximations and simplifications can be done. In Fig. 3.1 we show the thermodynamic potential of the the FF ansatz

$$\Delta_{\text{FF}}(\mathbf{x}) = \Delta_{\mathbf{Q}} \exp\left(\mathrm{i}\,\mathbf{Q} \cdot \mathbf{x}\right) \tag{3.3}$$

being the easiest choice that can be performed in (3.2) by selecting a single vector $\mathbf{Q}$. This case has been intensively studied and most of the times remains the paramount ansatz to study generic features of the FFLO phase. Anyway the FF choice is neither the best in terms of quantity of stable configurations nor the most energetically favourable. This fact has been shown in one and two dimensions and basically led

to consider another subfamily: the LO.

If we consider $\mathbf{Q}$ and $-\mathbf{Q}$, the opposite momentum, we actually may argue, by symmetry, that the associated coefficients in $\Delta(\mathbf{x}) = A\exp(i\mathbf{Q}\cdot\mathbf{x}) + B\exp(i\mathbf{Q}\cdot\mathbf{x})$ must verify $A = B$ providing the LO ansatz

$$\Delta_{\mathrm{LO}}(\mathbf{x}) = \Delta_{\mathbf{Q}}\cos(\mathbf{Q}\cdot\mathbf{x}) \tag{3.4}$$

The LO ansatz suffers from the loss of an analytic formula for the thermodynamic potential: as long as a single mode $\mathbf{k}$ can couple two different ones, namely $-\mathbf{k}\pm\mathbf{Q}$, the fermionic path integral cannot be solved any-more by using the Nambu spinors techniques.

We might further specialize the LO phase in other cases that are actually the target of our research. It has been shown, in 2D and 3D, that the spontaneous break of symmetry due to the LO transition essentially occurs in a random direction only, and moreover in 3D it occurs in a very narrow region of the phase diagram. However, when the system experiences high population imbalance, the order parameter can actually depend on 2 or 3 directions in the space. Eventually the study of the FFLO phases can be greatly simplified by taking into account this effective mono-dimensional symmetry breaking. If we require the order parameter to depend only on a single direction the cost of the diagonalisation of the system Hamiltonian can be reduced and a complete study even in 2 and 3 dimensions becomes available just by avoiding complicated multidimensional integrations. Given $\mathbf{x} = (x, \mathbf{x} - x\mathbf{e}_1)$, this new order parameter is referred usually as the LO_1 phase parameter

$$\Delta_{\mathrm{LO}_1}(\mathbf{x}) = \Delta_Q\cos(Qx) \tag{3.5}$$

The approach we used lets us model the order parameter as a much more detailed function as long as we keep the phase transition symmetry breaking in one direction. In particular, we were able to study the best generalization of the LO_1 phase that will be called LO_g throughout the chapter. The Fourier transform entails the most generic form for the order parameter as

$$\Delta_{\mathrm{LO}_g}(\mathbf{x}) = \sum_Q \Delta_Q\cos(Qx) \tag{3.6}$$

where Q here is summed over the periodic boundary conditions (PBC) box modes in a single direction. This choice (perhaps combined with a multidimensional counterpart) represents possibly the broader exotic phase in the imbalanced case of the Fermi gas and in the meantime the most energetically favourable of the FFLO phases so far studied.

For our purposes we are going to consider a two-dimensional Fermi gas. Due to the imbalance, we studied the various features and properties of its LO_g phase

choosing a preferred x direction, namely it'll be the first component of $\mathbf{x}$, and computing the best choice, in terms of energy of the order parameter. The transition between a constant order parameter (BCS theory), a spatially inhomogeneous parameter (LO_g phase) and a partially polarized non-interacting Fermi gas (N_{PP} phase) are investigated. In particular, at very high polarization the LO_g and LO_1 merge together.

3.2   Description of the model

We consider the case of a polarized Fermi gas in an exact 2D regime. Such a condition can be realized via a combination of harmonic traps alongside a radial and an axial direction. The tuning of the harmonic constants is often expressed in the anisotropic aspect ratio $\lambda = \omega_z/\omega_\rho$ that measures the size of the axial confinement, with frequency ω_z, over the radial counterpart denoted by ω_ρ. In the case of a polarized Fermi gas, a Feshbach resonance (see Chap. 1) can couple two different hyperfine states that will be labelled with pseudo-spins $\sigma = \uparrow, \downarrow$. Fermions must have an anti-symmetric wave function, hence in a scattering process where only opposite spins interact, at a sufficiently low temperature, we can consider the s-wave scattering only, leading to the effective Hamiltonian (see Chap. 2):

$$\mathscr{H} = \sum_\sigma \int_V d\mathbf{x} \; \psi_\sigma^*(\mathbf{x}) \left(-\frac{\hbar^2}{2m}\nabla^2 - \mu_\sigma \right) \psi_\sigma(\mathbf{x}) + g \int_V d\mathbf{x} \; \psi_\uparrow^*(\mathbf{x})\psi_\downarrow^*(\mathbf{x})\psi_\downarrow(\mathbf{x})\psi_\uparrow(\mathbf{x})$$

(3.7)

where $\psi_\sigma(\mathbf{x})$ is the Fermi field operator of the σ component, V the volume of the system, g the interaction coupling constant and, of course, m the mass of the considered species. We also introduce several variables which we will use throughout the chapter, namely the chemical potentials $\mu_{\uparrow,\downarrow} = \mu \pm \delta\mu$ in the grand canonical ensemble, and, in the canonical ensemble, the polarization

$$p = \frac{N_\uparrow - N_\downarrow}{N_\uparrow + N_\downarrow}$$

(3.8)

where $N = N_\uparrow + N_\downarrow$ is the total population of the system split into the two spin families and the population densities are given by

$$n_\sigma = \frac{N}{V}(1 + \mathrm{sgn}(\sigma)p)$$

(3.9)

defining $\mathrm{sgn}(\uparrow) = -\mathrm{sgn}(\downarrow) = +1$. The interaction is modelled as a contact potential interaction through the distribution $g\delta(\mathbf{x} - \mathbf{x}')$ that in the peculiar case of where two dimensions leads to issues of renormalisation discussed further in Chap. 2. The s-wave 2D channel has a scattering amplitude given by

$$f_s(k) = -\frac{4\pi}{2\log(ka_{2D}) - \mathrm{i}\pi + \mathscr{O}(k^2)}$$

(3.10)

as a function of the 2D scattering length $a_{2\mathrm{D}}$. The scattering amplitude can be recovered, from the contact potential, by setting

$$\frac{1}{g} = -\frac{1}{V} \sum_{\mathbf{k}} \frac{1}{2\varepsilon_{\mathbf{k}} + \varepsilon_b} \tag{3.11}$$

and defining

$$\varepsilon_b = \frac{\hbar^2}{ma_{2\mathrm{D}}^2} \tag{3.12}$$

We notice that, in order to have a well defined scattering amplitude, both $a_{2\mathrm{D}}$ and ε_b are required to be positively defined. The binding energy in particular cannot vanish in order to ensure dilation correction and, on the other side, the 2D scattering length cannot prevent the blow up of $\log(ka_{2\mathrm{D}})$ at low energy. The energy of the bound state is negative and given by $E = -\varepsilon_b$.

The sign of the scattering length in two dimensions then discloses the problem of how to relate a 3D scattering length in an actual experimental setting with its 2D counterpart, when a system is brought towards low dimensionality, using a proper aspect ratio. The 3D scattering length describes either a weakly-interacting regime (when small and negative), a strongly-interacting regime (if small and positive) or the unitarity when diverging. Integrating out the unessential direction in the system (namely in this case the axial one) we can relate the 3D scattering length to an effective quasi-2D scattering length [86]

$$\frac{a_{2\mathrm{D}}}{l_z} = \sqrt{\frac{\pi}{B}} \exp\left(-\sqrt{\frac{\pi}{2}} \frac{l_z}{a_{3D}}\right) \tag{3.13}$$

where $l_z = \sqrt{\hbar/(m\omega_z)}$ represents the axial harmonic oscillator typical length, $B = 0.905$ is a constant, moreover the previous approximation is valid when the scattering energy is negligible compared with the strength of the confinement. Typically [50, 60] in 2D, or quasi-2D experiments, the aspect ratio can reach the regime $\omega_z \gg \omega_\rho$ with values around $\lambda \approx 60 - 200$, an axial frequency of $\omega_z/(2\pi) \approx 2.8\mathrm{kHz} - 9\mathrm{kHz}$ and $\omega_\rho/(2\pi) \approx 47\mathrm{Hz} - 440\mathrm{Hz}$. The axial separation produces layered pancake-shaped clouds that can contain orders of thousands of atoms. When the two dimensional regime is reached, the scale of energies can be therefore analysed in terms of the 2D Fermi energy that grows as the square root of the number of particles verifying the law $\varepsilon_F = \sqrt{2N}\hbar\omega_\rho$ that has the order of $10^{-11}\mathrm{eV}$. In actual experiments we remark that the lowest binding energy achievable is strongly related to the lowest temperature that the system can experience. The reference value is around $\beta\varepsilon_b = \frac{T_F}{T}\frac{\varepsilon_b}{\varepsilon_F} \approx 0.26 - 0.46$. Proceeding in this direction, the need for low temperature in an effective 2D, or quasi-2D regime, requires the study of interaction regimes that are neither weak nor close to $\log(k_F a_{2\mathrm{D}}) = 0$. It is indeed pretty straightforward

that under these conditions a pair-fluctuations approach will be essential to treat both critical temperatures of the phases under inspection varying the imbalance in the system. Moreover, since we are considering an imbalanced Fermi gas, we also note that in a quasi-2D regime (where interactions between different clouds of the layered stack are partially occurring) the broadest range of polarisations has been achieved: the ratio of the two populations involved may vary accordingly to $\frac{n_\downarrow}{n_\uparrow} = \frac{1-p}{1+p} \approx 0.1 - 1.1$.

3.2.1 BdG self-consistent method

We considered the most generic LO_g order parameter, accordingly to (3.6). The dependence of the mean field has to be set in a chosen direction, namely the first component of $\mathbf{x} = (x, y)$. The lack of spacial symmetry suggested us to solve the model in the real space rather than in momentum space. We consider the Bogoliubov-de Gennes equations, starting from the Heisenberg equation of motion of the Hamiltonian (4.1). Without any trapping potential, we obtain for the fermionic fields $\psi_\sigma(\mathbf{x}, t)$

$$\mathrm{i}\partial_t \psi_\sigma = \left(-\frac{\hbar^2 \nabla^2}{2m} - \mu_\sigma \mathbb{1}\right)\psi_\sigma - g(\mathrm{sgn}\,\sigma)\psi_{\bar\sigma}^* \psi_\downarrow \psi_\uparrow \tag{3.14}$$

Via the mean-field theory, we can replace the coupled terms with the expectation values

$$- g(\mathrm{sgn}\,\sigma)\psi_{\bar\sigma}^* \psi_\downarrow \psi_\uparrow \approx g n_{\bar\sigma}(\mathbf{x})\psi_\sigma - (\mathrm{sgn}\,\sigma)\Delta(\mathbf{x})\psi_{\bar\sigma}^* \tag{3.15}$$

where we defined the order parameter and the density profiles to be

$$\Delta(\mathbf{x}) = -g\langle\psi_\downarrow(\mathbf{x})\psi_\uparrow(\mathbf{x})\rangle$$
$$n_{\bar\sigma}(\mathbf{x}) = \langle\psi_\sigma^*(\mathbf{x})\psi_\sigma(\mathbf{x})\rangle \tag{3.16}$$

The effective Hamiltonian has now a spin dependency $\mathscr{H}_\sigma = -\nabla_{\mathbf{x}}^2 + g n_{\bar\sigma}(\mathbf{x})\mathbb{1}$, but the renormalisation procedure will send g^{-1} to infinity, hence we can systematically neglect any linear dependency in g when we restore the renormalisation cut-off to infinity: in that case the Hamiltonian lacks the Hartree term $g n_{\bar\sigma}(\mathbf{x})\mathbb{1}$. Indeed we can set $\mathscr{H}_0 = -\nabla_{\mathbf{x}}^2$ obtaining

$$\mathrm{i}\frac{\partial \psi_\sigma}{\partial t}(\mathbf{x}, t) = (\mathscr{H}_0 - \mu_\sigma \mathbb{1})\psi_\sigma(\mathbf{x}, t) - \mathrm{sgn}(\sigma)\Delta(\mathbf{x})\psi_{\bar\sigma}^*(\mathbf{x}, t) \tag{3.17}$$

We insert the standard Bogoliubov transformation

$$\psi_\uparrow(\mathbf{x}, t) = \sum_\eta \left[u_{\eta\uparrow}(\mathbf{x})c_{\eta\uparrow}e^{-\mathrm{i}E_{\eta\uparrow}t} - \overline{v_{\eta\downarrow}(\mathbf{x})}c_{\eta\downarrow}^* e^{\mathrm{i}E_{\eta\downarrow}t}\right]$$
$$\psi_\downarrow^*(\mathbf{x}, t) = \sum_\eta \left[\overline{u_{\eta\downarrow}(\mathbf{x})}c_{\eta\downarrow}^* e^{\mathrm{i}E_{\eta\downarrow}t} + v_{\eta\uparrow}(\mathbf{x})c_{\eta\uparrow}e^{-\mathrm{i}E_{\eta\uparrow}t}\right] \tag{3.18}$$

that also requires the new quasi-particle operators to be fermionic under the usual anti-commutation rules

$$\{c_{\sigma\eta}, c_{\sigma'\eta'}\} = 0 \qquad \{c_{\sigma\eta}^*, c_{\sigma'\eta'}^*\} = 0 \qquad \{c_{\sigma\eta}, c_{\sigma'\eta'}^*\} = \delta_{\sigma\sigma'}\delta_{\eta\eta'}\mathbb{1} \qquad (3.19)$$

and such that the modes are normalised by the choice

$$\int_V d^2x \ \left(|u_{\sigma\eta}(\mathbf{x})|^2 + |v_{\sigma\eta}(\mathbf{x})|^2\right) = 1 \qquad (3.20)$$

The BdG equations, written in the form

$$A_\sigma \begin{pmatrix} u_{\eta\sigma} \\ v_{\eta\sigma} \end{pmatrix} = \begin{pmatrix} \mathscr{H}_0 - \mu_\sigma & -\Delta(\mathbf{x}) \\ -\overline{\Delta(\mathbf{x})} & -(\mathscr{H}_0 - \mu_{\bar\sigma}) \end{pmatrix} \begin{pmatrix} u_{\eta\sigma} \\ v_{\eta\sigma} \end{pmatrix} = E_{\eta\sigma} \begin{pmatrix} u_{\eta\sigma} \\ v_{\eta\sigma} \end{pmatrix} \qquad (3.21)$$

explicitly show a particle-hole symmetry given by the relations

$$A_\uparrow = -D^{-1}\overline{A_\downarrow}D \qquad D = \begin{pmatrix} 0 & 1 \\ -1 & 0 \end{pmatrix} \qquad (3.22)$$

Hence the $\downarrow$ problem is related to the $\uparrow$ problem through the particle-hole transformation

$$-D\overline{\begin{pmatrix} u_{\eta\uparrow} \\ v_{\eta\uparrow} \end{pmatrix}} = \begin{pmatrix} u_{\eta\downarrow} \\ v_{\eta\downarrow} \end{pmatrix} = \begin{pmatrix} -\overline{v_{\eta\uparrow}} \\ \overline{u_{\eta\uparrow}} \end{pmatrix} \qquad E_{\eta\uparrow} = -E_{\eta\downarrow} \qquad (3.23)$$

Without loss of generality, we can define $u_\eta = u_{\eta\uparrow}$, $v_\eta = v_{\eta\uparrow}$ and $E_\eta = E_{\eta\uparrow}$ and the BdG equations become

$$\begin{pmatrix} \mathscr{H}_0 - \mu_\uparrow & -\Delta(\mathbf{x}) \\ -\overline{\Delta(\mathbf{x})} & -\mathscr{H}_0 + \mu_\downarrow \end{pmatrix} \begin{pmatrix} u_\eta \\ v_\eta \end{pmatrix} = E_\eta \begin{pmatrix} u_\eta \\ v_\eta \end{pmatrix} \qquad (3.24)$$

The Bogoliubov transformations redefined the order parameter Δ and the density profiles n_σ through the new quasi-particles creation/annihilation operators. We impose fermionic statistics for excitations, with a defined inverse temperature $\beta = \frac{1}{k_B T}$. The average of an excitation has probability given by the Fermi-Dirac statistics $f(E_{\sigma\eta}) = \frac{1}{1+e^{\beta E_{\sigma\eta}}}$ that leads to the self-consistent definitions of the density profiles

$$n_\uparrow(\mathbf{x}) = \sum_\eta \overline{u_\eta(\mathbf{x})}u_\eta(\mathbf{x})f(E_\eta) \qquad (3.25)$$

$$n_\downarrow(\mathbf{x}) = \sum_\eta \overline{v_\eta(\mathbf{x})}v_\eta(\mathbf{x})f(-E_\eta) \qquad (3.26)$$

and the energy gap order parameter

$$\Delta(\mathbf{x}) = -g \sum_\eta u_\eta(\mathbf{x})\overline{v_\eta(\mathbf{x})}f(E_\eta) \qquad (3.27)$$

The complete study of this system, either at zero or finite temperature, can be done in the canonical ensemble, fixing a total density n and a polarisation $p = \delta n/n$. Similarly, we will perform calculations in the grand canonical ensemble, fixing the chemical potential μ and its variation $\delta\mu$ as described above. The latter case requires us to find the absolute minimum of the thermodynamic potential $\Omega = \Omega(\mu, \delta\mu, \beta) = U - TS - \mu N - \delta\mu\delta N$, where U is the internal energy and S is the entropy. The former case instead requires more effort: since the BdG equations depend on μ and $\delta\mu$, we must self-consistently compute them using the number equations

$$N = -\frac{\partial\Omega}{\partial\mu} \qquad \delta N = -\frac{\partial\Omega}{\partial(\delta\mu)} \tag{3.28}$$

obtaining $\mu(n, \delta n, \beta)$ and $\delta\mu(n, \delta n, \beta)$. The Helmholtz free energy $F = F(n, p, \beta) = U - TS$ is now the quantity to be minimized, otherwise we would have a spontaneous thermodynamic process from the computed ground state towards a more stable state. Any prediction we want to compute of the system requires the knowledge of both the density of the grand canonical Hamiltonian and the entropy. Through the Bogoliubov transformations we can define the profiles for the energy density $e(\mathbf{x})$ and the entropy density $s(\mathbf{x})$ on quasi-particles modes as

$$\begin{aligned}
e(\mathbf{x}) = \frac{1}{V}\langle\mathcal{H}\rangle = &\mu_\uparrow n_\uparrow(\mathbf{x}) + \mu_\downarrow n_\downarrow(\mathbf{x}) - \frac{|\Delta(\mathbf{x})|^2}{g} \\
&+ \sum_\eta \left[(|u_\eta(\mathbf{x})|^2 + |v_\eta(\mathbf{x})|^2)f(E_\eta) - |v_\eta(\mathbf{x})|^2\right]
\end{aligned} \tag{3.29}$$

$$s(\mathbf{x}) = -k_B \sum_\eta \left[f(E_\eta)\log(f(E_\eta)) + f(-E_\eta)\log(f(-E_\eta))\right](|u_\eta(\mathbf{x})|^2 + |v_\eta(\mathbf{x})|^2) \tag{3.30}$$

$$\begin{aligned}
\frac{\Omega}{V} &= \int_V d\mathbf{x} \left(e(\mathbf{x}) - \frac{s(\mathbf{x})}{\beta} - \mu_\uparrow n_\uparrow(\mathbf{x}) - \mu_\downarrow n_\downarrow(\mathbf{x})\right) \\
&= \frac{F}{V} - \int_V d\mathbf{x}\,(\mu_\uparrow n_\uparrow(\mathbf{x}) + \mu_\downarrow n_\downarrow(\mathbf{x}))
\end{aligned} \tag{3.31}$$

In order to obtain concrete results, we discuss the treatment of this system in terms of a hybrid algorithm that considers high-energy contributions to the system as though they were free states, or single-plane-wave functions.

3.2.2 LO$_g$ ansatz implementation

We apply the previous formalism to a two-component Fermi gas with fixed, even though big, number of atoms. In particular, we consider a two-dimensional periodic boundary condition box with side L and area $V = L^2$. The thermodynamic limit to study the Grand Canonical Ensemble will be restored by increasing the size of the box. The high-energy states must be truncated via a cut-off and a renormalisation

procedure that is enforced by checking the independence of the model from the chosen cut-off value.

A two-dimensional fermionic system enjoys the linear relation between the density and the free Fermi energy $k_{F_\sigma}^2 = 4\pi\frac{N_\sigma}{V}$ hence, to approximate the thermodynamic limit, we choose to fix the Fermi energy at vanishing polarisation and establish a linear relation between area and number of particles. Therefore, to approach the limit the number of particles must increase. The periodic boundary conditions allow us the choice of a completely real-valued Hilbert orthonormal basis, that combined with the further choice of a real-valued order parameter, reduces the complexity of the system. We fixed for each $\mathbf{n} = (n_1, n_2) \in \mathbb{N} \times \mathbb{N}$

$$\phi_{\mathbf{n}}^{(2)}(\mathbf{x}) = \phi_{n_1}^{(1)}(x)\phi_{n_2}^{(1)}(y) \tag{3.32}$$

using the tensor product properties on multidimensional boxes and set

$$\phi_n^{(1)}(x) := \begin{cases} L^{-1/2} & \text{if } n = 0 \\ (2/L)^{1/2}\cos\left[n\pi x/L\right] & \text{if } n \text{ is even} \\ (2/L)^{1/2}\sin\left[(n+1)\pi x/L\right] & \text{if } n \text{ is odd} \end{cases} \tag{3.33}$$

with n_1 and n_2 running on non-negative integers. $(\phi_n^{(1)}(x))_n$ is an eigenvector system for the one-dimensional free Hamiltonian $-\frac{\hbar^2}{2m}\frac{d^2}{dx^2}$ with eigenvalues

$$\varepsilon_n := \begin{cases} \pi^2 n^2/L^2 & \text{if } n \text{ is even} \\ \pi^2(n+1)^2/L^2 & \text{if } n \text{ is odd} \end{cases} \tag{3.34}$$

returning an eigenvector basis for $\mathscr{H}_0$ with eigenvalues $\varepsilon_{\mathbf{n}} = \varepsilon_{n_1} + \varepsilon_{n_2}$. Both u_η and v_η are projected on this basis

$$u_\eta(\mathbf{x}) = \sum_{\mathbf{n}} A_{\mathbf{n}}^{(\eta)}\phi_{\mathbf{n}}^{(2)}(\mathbf{x}) \qquad v_\eta(\mathbf{x}) = \sum_{\mathbf{m}} B_{\mathbf{m}}^{(\eta)}\phi_{\mathbf{m}}^{(2)}(\mathbf{x})$$

Equation (3.24), because of orthonormality, can be closed on the left side with a scalar product on every $\mathbf{n}$ and it becomes

$$\sum_{\mathbf{m}} \left[(\varepsilon_{\mathbf{n}} - \mu_\uparrow)\delta_{\mathbf{nm}}A_{\mathbf{n}}^{(\eta)} - \Delta_{\mathbf{nm}}B_{\mathbf{m}}^{(\eta)} \right] = E_\eta A_{\mathbf{n}}^{(\eta)} \tag{3.35}$$

and also

$$\sum_{\mathbf{m}} \left[-(\varepsilon_{\mathbf{n}} - \mu_\downarrow)\delta_{\mathbf{nm}}B_{\mathbf{n}}^{(\eta)} - \overline{\Delta_{\mathbf{nm}}}A_{\mathbf{m}}^{(\eta)} \right] = E_\eta B_{\mathbf{n}}^{(\eta)} \tag{3.36}$$

where

$$\Delta_{\mathbf{nm}} = \int_V d^2x\ \phi_{\mathbf{n}}^{(2)}(\mathbf{x})\Delta(\mathbf{x})\phi_{\mathbf{m}}^{(2)}(\mathbf{x}) \tag{3.37}$$

Notice that so far we didn't imply any other approximation other than the mean field one. We consider now the LO$_\mathrm{g}$ ansatz in (3.6). The periodic boundary conditions

force the Fourier transform of $\Delta(\mathbf{x})$ to be dependent on the discretised modes of the box only. This fixes $Q = 2\pi n/L$ for each non-negative integer $n \in \mathbb{N}$. Albeit the modes might have negative indexes, the LO_g choice rejects them due to the even symmetry of the order parameter. From equation (3.37), using $\phi_\mathbf{n}^{(2)}$ basis sub-orthogonality under projection, we can integrate, for each $\mathbf{n} = (n_1, n_2)$ and each $\mathbf{m} = (m_1, m_2)$, over the variable y defining

$$
\begin{aligned}
\Delta_{\mathbf{nm}} &= \delta_{n_2,m_2} \int_{-L/2}^{L/2} dx \; \phi_{n_1}^{(1)}(x)\Delta(x)\phi_{m_1}^{(1)}(x) \\
&= \delta_{n_2,m_2}\Delta_{n_1,m_1}
\end{aligned}
\tag{3.38}
$$

Moreover, the dependence on the x direction only, through definition (3.27), reduces the complexity of the entire system since giving, for all η

$$
\begin{aligned}
u_\eta(\mathbf{x})\overline{v_\eta(\mathbf{x})} &= \sum_{\mathbf{n},\mathbf{m}} A_\mathbf{n}^{(\eta)} \overline{B_\mathbf{m}^{(\eta)}} \phi_\mathbf{n}^{(2)}(\mathbf{x})\phi_\mathbf{m}^{(2)}(\mathbf{x}) \\
&= \sum_{n_1,n_2}\sum_{n_2,m_2} \left(A_{n_1,n_2}^{(\eta)} \overline{B_{m_1,m_2}^{(\eta)}} \phi_{n_2}^{(1)}(y)\phi_{m_2}^{(1)}(y) \right) \phi_{n_1}^{(1)}(x)\phi_{m_1}^{(1)}(x)
\end{aligned}
\tag{3.39}
$$

The internal part (the content of round brackets in equation (3.39)), depending on n_2 and m_2 has to be constant. In particular, it is constant for $n_2 = m_2 = 0$ with a contribution equal to $1/L$. Moreover, for every combination $n_2 = m_2$ added up with the $n_2 + 1 = m_2 + 1$ term, when n_2 is odd, equation (3.39) verifies

$$
\phi_{n_2}^{(1)}(y)\phi_{m_2}^{(1)}(y) = \frac{2}{L}\sin\left(\frac{(n_2+1)\pi y}{L}\right)^2
\tag{3.40}
$$

$$
\phi_{n_2+1}^{(1)}(y)\phi_{m_2+1}^{(1)}(y) = \frac{2}{L}\cos\left(\frac{(n_2+1)\pi y}{L}\right)^2
\tag{3.41}
$$

Hence we just need to require

$$
A_{n_1,n_2}^{(\eta)} \overline{B_{m_1,m_2}^{(\eta)}} = A_{n_1,n_2+1}^{(\eta)} \overline{B_{m_1,m_2+1}^{(\eta)}} = c\delta_{n_2,m_2}
\tag{3.42}
$$

with $c \in \mathbb{R}$. The $n_2 \neq m_2$ terms must disappear for sure in order to ensure the y independence and we can conclude that either $B_{m_1,m_2}^{(\eta)}$ is the complex conjugate of $A_{n_1,n_2}^{(\eta)}$ or $B_{m_1,m_2}^{(\eta)}$ is real. The former case is not possible because the equations they solve, i.e. (3.35) and (3.36) are not complex conjugate of one another, hence the latter case infers that off-diagonal terms in n_2 and m_2 are both vanishing. Instead of (3.35) and (3.36), we fix n_2 and for notational simplicity we call $A_{k,n_2}^{(\eta)} = A_k$, $B_{k,n_2}^{(\eta)} = B_k$ and summing m_2 we get the most simplified form for the BdG equations

$$
\sum_m \left[-\Delta_{k,m}B_m\right] = (E_\eta - \varepsilon_{k,(n_2)} + \mu_\uparrow)A_k
\tag{3.43}
$$

$$
\sum_m \left[-\Delta_{k,m}A_m\right] = (E_\eta + \varepsilon_{k,(n_2)} - \mu_\downarrow)B_k
\tag{3.44}
$$

for any n_1 non-negative integer and any η.

3.2.3   Treatment of states beyond the cut-off

In the spirit of [47], we introduce a cut-off energy E_c to deal with both renormalisation of the contact potential and the high-lying states that we cannot handle in the eigenvalue problem given by (3.43) and (3.44). We then split each quantity in a discrete part, below the cut-off, that maintains the very same definition stated previously, and a "continuous" part above the cut-off that is treated as a plane wave approximation. From equations (3.25), (3.26) and (3.27) we truncate the sums to get the discrete parts

$$n_{d\uparrow}(\mathbf{x}) = \sum_{|E_\eta|<E_c} \overline{u_\eta(\mathbf{x})} u_\eta(\mathbf{x}) f(E_\eta) \tag{3.45}$$

$$n_{d\downarrow}(\mathbf{x}) = \sum_{|E_\eta|<E_c} \overline{v_\eta(\mathbf{x})} v_\eta(\mathbf{x}) f(-E_\eta) \tag{3.46}$$

$$\Delta_d(\mathbf{x}) = -g \sum_{|E_\eta|<E_c} u_\eta(\mathbf{x}) \overline{v_\eta(\mathbf{x})} f(E_\eta) \tag{3.47}$$

The high-lying states are then recognized by using the condition $|E_\eta| \geq E_c$ and in this regime we consider the quasi-particles modes, since they are very high energy excitations, as plane waves

$$u_\eta(\mathbf{x}) \to \frac{1}{\sqrt{V}} u_k(\mathbf{x}) e^{i\mathbf{k}\cdot\mathbf{x}} \quad v_\eta(\mathbf{x}) \to \frac{1}{\sqrt{V}} v_k(\mathbf{x}) e^{i\mathbf{k}\cdot\mathbf{x}} \tag{3.48}$$

These prescriptions allow us to solve (3.24) again and recompute the part that was neglected above the cut-off. In particular we can define the energies $E_k(\mathbf{x}) = \sqrt{(\varepsilon_k - \mu)^2 + \Delta(\mathbf{x})^2}$ and obtain the continuum corrections

$$n_{c\uparrow}(\mathbf{x}) = \frac{1}{V} \sum_{|\mathbf{k}|^2 > E_c} \left(\frac{1}{2} - \frac{\varepsilon_k - \mu}{2E_k(\mathbf{x})} \right) \vartheta(E_k(\mathbf{x}) + \delta\mu - E_c) \tag{3.49}$$

$$n_{c\downarrow}(\mathbf{x}) = \frac{1}{V} \sum_{|\mathbf{k}|^2 > E_c} \left(\frac{1}{2} - \frac{\varepsilon_k - \mu}{2E_k(\mathbf{x})} \right) \vartheta(E_k(\mathbf{x}) - \delta\mu - E_c) \tag{3.50}$$

$$G(\mathbf{x}) = \frac{1}{V} \sum_{|\mathbf{k}|^2 > E_c} \frac{1}{2E_k(\mathbf{x})} \vartheta(E_k(\mathbf{x}) + \delta\mu - E_c) \tag{3.51}$$

with

$$\frac{1}{g_{\text{eff}}(\mathbf{x})} = \frac{1}{g} + G(\mathbf{x}) \tag{3.52}$$

In the thermodynamic limit, due to the high density of states beyond the cut-off, we swap to a continuous integration that luckily has an analytic primitive. We introduce the cut-off function on the momentum given by

$$k_c(\mathbf{x}) = \left(\mu + \sqrt{(E_c - \delta\mu)^2 - \Delta(\mathbf{x})^2} \right)^{1/2}$$

and we have

$$n_{c\uparrow}(\mathbf{x}) = \frac{1}{8\pi} \left[E_c - \delta\mu + \mu - k_c(\mathbf{x})^2 \right] \tag{3.53}$$

$$n_{c\downarrow}(\mathbf{x}) = \frac{1}{8\pi} \left[E_c + \delta\mu + \mu - k_c(\mathbf{x})^2 \right] \tag{3.54}$$

$$g_{\text{eff}}^{-1}(\mathbf{x}) = -\frac{1}{8\pi} \log \left(\frac{E_c - \delta\mu - \mu + k_c(\mathbf{x})^2}{\varepsilon_b} \right) \tag{3.55}$$

Gathering together all these results we achieved the final form for profiles and order parameter, merging the different contributions

$$n_{\uparrow}(\mathbf{x}) = n_{d\uparrow}(\mathbf{x}) + n_{c\uparrow}(\mathbf{x}) \tag{3.56}$$

$$n_{\downarrow}(\mathbf{x}) = n_{d\downarrow}(\mathbf{x}) + n_{c\downarrow}(\mathbf{x}) \tag{3.57}$$

$$\Delta(\mathbf{x}) = \frac{g_{\text{eff}}(\mathbf{x})}{g} \Delta_d(\mathbf{x}) \tag{3.58}$$

Since both energy density and entropy density depend on sums over the eigenvalues E_η, we can extend the discrete plus continuous strategy to those quantities as well. It is possible to show that the continuous correction to the entropy density is absolutely negligible for high-lying states. Instead, the correction to the free energy is fundamental to ensure the convergence when we restore $1/g \to \infty$ by sending E_c to infinity. Treating the high energy states in the thermodynamic limit we can write $e(\mathbf{x}) = e_d(\mathbf{x}) + e_c(\mathbf{x})$ and we get

$$\begin{aligned}
e_c(\mathbf{x}) = &\frac{\Delta^2}{8\pi} \left[\frac{1}{2} + \log \left(\frac{\sqrt{E_- + \sqrt{E_-^2 - \Delta^2}} \sqrt{E_+ + \sqrt{E_+^2 - \Delta^2}}}{\varepsilon_b} \right) \right] \\
&+ \sum_{\sigma=\pm} \frac{1}{8\pi} \left(\frac{E_\sigma}{2} \sqrt{E_{\bar\sigma}^2 - \Delta^2} - E_c^2 + \delta\mu^2 \right)
\end{aligned} \tag{3.59}$$

where for simplicity we defined $E_\pm = E_c \pm \delta\mu$.

Despite that we decisively reduced a 2D problem to a simpler 1D one, it is intuitive that the introduction of a cut-off is controlling the effective cost of computations in terms of the number of modes that we are going to use in the Bogoliubov transformation of the fermionic fields. Indeed, once a certain mode is fixed in the y direction, let us call it n_2, the problem is directly affected by the cut-off that imposes us to consider any x direction mode such that

$$n_1 < \sqrt{\frac{E_c L^2}{\pi^2} - n_2^2} = \bar{n} \tag{3.60}$$

It is easy now to cast the Bogoliubov equations into their truncate form starting

from (3.43) and (3.44), for each $n_2 < E_c$

$$
\mathbb{M} = \begin{pmatrix}
\varepsilon_{00,n_2} - \delta\mu_\uparrow & \cdots & 0 & -\Delta_{00} & \cdots & -\Delta_{0\bar{n}} \\
\vdots & \ddots & \vdots & \vdots & \ddots & \vdots \\
0 & \cdots & \varepsilon_{\bar{n}\bar{n},n_2} - \delta\mu_\uparrow & -\Delta_{\bar{n}0} & \cdots & -\Delta_{\bar{n}\bar{n}} \\
-\Delta_{00} & \cdots & -\Delta_{0\bar{n}} & -\varepsilon_{00,n_2} + \delta\mu_\downarrow & \cdots & 0 \\
\vdots & \ddots & \vdots & \vdots & \ddots & \vdots \\
-\Delta_{\bar{n}0} & \cdots & -\Delta_{\bar{n}\bar{n}} & 0 & \cdots & -\varepsilon_{\bar{n}\bar{n},n_2} + \delta\mu_\downarrow
\end{pmatrix} \tag{3.61}
$$

$$
\mathbb{M} \begin{pmatrix}
A_{0,n_2}^{(\eta)} \\
\vdots \\
A_{\bar{n},n_2}^{(\eta)} \\
B_{0,n_2}^{(\eta)} \\
\vdots \\
B_{\bar{n},n_2}^{(\eta)}
\end{pmatrix} = E_\eta \begin{pmatrix}
A_{0,n_2}^{(\eta)} \\
\vdots \\
A_{\bar{n},n_2}^{(\eta)} \\
B_{0,n_2}^{(\eta)} \\
\vdots \\
B_{\bar{n},n_2}^{(\eta)}
\end{pmatrix} \tag{3.62}
$$

The solutions to the BdG equations were carried out following an iterative algorithm in order to compute self-consistently the order parameter and the density profiles. Such an algorithm works either in the grand canonical ensemble, fixing the parameters μ and $\delta\mu$ and computing the number of particles N and the polarization p, or in the canonical ensemble, fixing N and p and iteratively computing the right value of μ and $\delta\mu$. These values have to solve the number equations (3.28) and then preserving the number of particles until the convergence is reached. It is important to remark that the nature of the quantities we want to investigate, like the Helmholtz free energy and thermodynamic potential, shows very small variations while changing the thermodynamic variables.

3.3 Results

The results of this work fix the range of critical values, like critical transition temperature for the $\mathrm{LO_g}$ phase, not so far away from the ultracold temperature nowadays achievable. In the specific case we studied the model described in the previous section, with a choice of parameters as close as possible to the experimental data currently available. The reference parameter for a 2D system, to control whether the system lies in the quasi-2D regime or in the exact 2D approximation, is the pure number $\beta\varepsilon_b$. We then decided to study the model in both the weakly-interacting regime $\varepsilon_b \leq 0.10\varepsilon_F$ and in a hybrid regime of $\varepsilon_b = 0.25\varepsilon_F$, that experimentally can be reached, but possibly requires a further study due to Gaussian pair-fluctuations being neither in the weakly-interacting nor in the inherited unitary regime in 2D. Indeed, we mentioned that the 2D case acquires a definition of unitary regime through

the relationship (3.13) and then the unitary regime is defined as an approximation of a three-dimensional behaviour. The results which we are going to provide show that the mean field theory of the LO_g phase is still a very good descriptive starting point for the scenario that we are investigating in a qualitative and, overall, quantitative sense.

The self-consistent method to compute the order parameter gave us a very good insight into the behaviour of the LO_g phase in a broad variety of initial conditions and thermodynamic variables. In actual calculations we also set natural units such that $\hbar = 2m = k_B = 1$. Moreover, in case of a non vanishing polarisation we set $k_F = 1$ where k_F is, at fixed number of particles, the Fermi wave vector of one of the populations when the polarisation is brought to zero. This configuration allowed one of the main computational bottlenecks of the system to arise: the linear relation between the Fermi energy and the density of particles. An increase in the number of particles entails, at least, a quadratic increase of the BdG equations matrix. In a fully parallelised code we have been able to achieve results for $N = 2000$, which means $k_F L \approx 112$. This is comparable with similar results in the 1D case [47]. On the other hand, the cut-off energy E_c must be kept high enough to ensure the independence of the model from the renormalisation procedure: we have been able to achieve this condition setting $E_c \geq 10\varepsilon_F$. The required precision of the algorithm forced us to pick such a value in the interval $16\varepsilon_F \leq E_c \leq 35\varepsilon_F$. A higher E_c slows down the runtime but reduces the number of iterations before convergence, while a small E_c behaves in the opposite way. Since the truncation of a matrix can affect the accuracy of the diagonalisation process, we add extra rows and columns beyond the cut-off and we discard them at the end of the diagonalisation procedure for Eq. (3.62). The integrations performed needed a very large lattice of sampling points that was fixed, depending on the integration routine, in order to achieve the relative error 10^{-7} in the of the thermodynamic potential. The model modifies an initial LO_1 ansatz for $\Delta(x)$ that is provided according to equation (3.5). The finite size of our box forces the frequency Q of the LO_1 ansatz to be less precise than the periodic boundary condition factor $2\pi/k_F L \approx 0.05$. This limitation prevents us from being able to check very low polarizations when $p < 0.02$, but this is relevant in the zero temperature case anyway.

3.3.1 Structure of the LO_g order parameter

At temperature $T/T_F = 0$ and hybrid binding energy $\varepsilon_b = 0.25\varepsilon_F$, the LO_g phase is present and energetically favourable (with respect to the BCS and FF minima) on a broad range of polarizations $0.02 \leq p \leq 0.58$. Above $p > 0.58$ the system falls into the free Fermi gas case unless more complicated LO_2 phases are considered. In
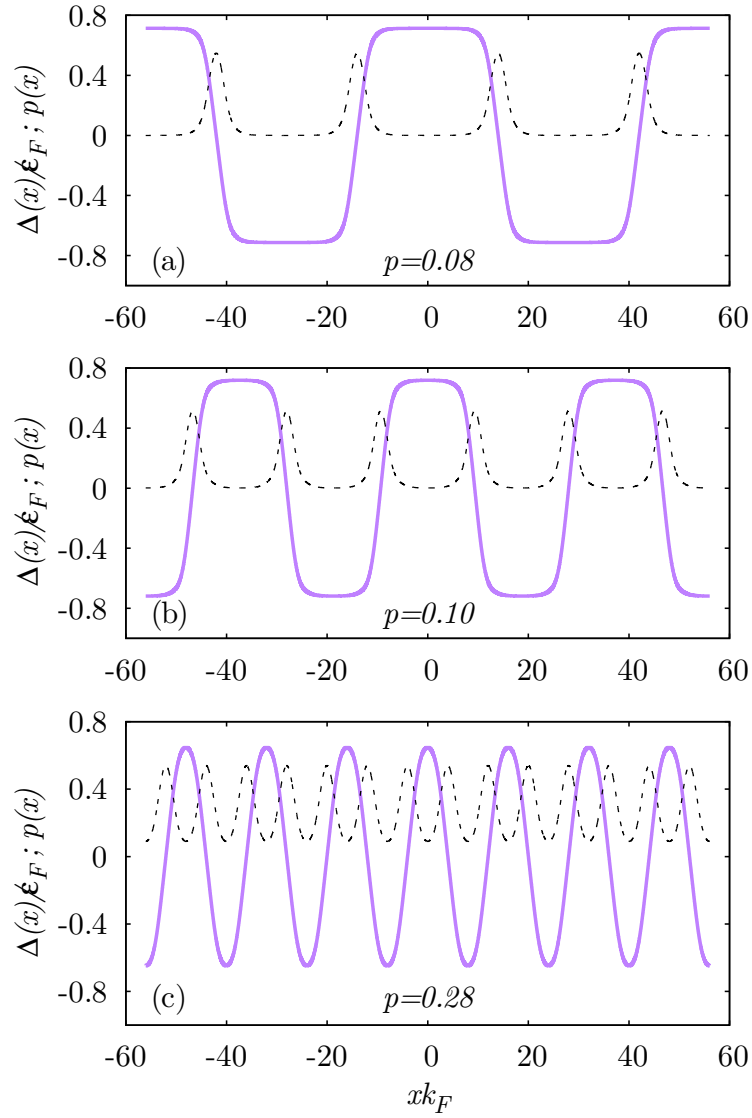
Figure 3.2: *At zero temperature and $\varepsilon_b = 0.25\varepsilon_F$, the structure of the inhomogeneous order parameter $\Delta(x)/\varepsilon_F$ as a function of the x direction (solid line) and the local imbalance $p(x)$ (dashed line) calculated via the self-consistent method, from (a) to (c), increasing the polarization p. From [49].*

the composite Fig. 3.2 the structure of the order parameter is pictured as a function of the x coordinate. Through the different panels, from (a) to (c), the increasing polarization p leads to a higher frequency Q and likewise an increasing matching among effective self-consistent solutions and the original LO_1 initial ansatz. The very same figure presents also the local imbalance as a function of space

$$p(x) = \frac{n_\uparrow(x) - n_\downarrow(x)}{n_\uparrow(x) + n_\downarrow(x)} \tag{3.63}$$

It is interesting to observe the structure imposed to the system by the LO_g phase. It turns out that the most favourable ground state configuration places the imbalanced part of the gas where the pairing gap is lower and keeps the superfluid part firmly under the peaks and valleys. Excitations are most probable to occur on the imbalanced part instead of the superfluid part beneath the pairing gap. If compared with the Helmholtz free energy of both BCS and free Fermi gas theories, the LO_g phase provides the system either with a single absolute minimum of free energy, at low polarization, or many local minima (absolute minimum included) at high polarization. The configuration is energetically favourable in a broad region of polarizations and for finite temperatures always below $T = 0.15T_F$. For a fixed polarization p we define the free Fermi gas Helmholtz free energy at zero temperature $F_{\text{free}}(T = 0, n, p)$ and we introduce a rescaling constant $F_0 = 2\pi \times 10^{-2}\varepsilon_F N$, with N the number of particles, such that we can plot the dimensionless quantity

$$\delta F/F_0 = (F_{\text{LO}_g}(T, n, p) - F_{\text{free}}(T = 0, n, p))/F_0 \tag{3.64}$$

In Fig. 3.3 we show the Helmholtz free energy in two different cases: in panel (a) at zero temperature we let the polarization vary and we show that the minimum of the free energy always lies away from $Q/k_F = 0$ (that is the BCS theory) and keeps increasing proportionally to the polarisation. In panel (b) the polarization is fixed at $p = 0.07$ and we increase the temperature: we notice that there is a transition point between the LO_g phase and the BCS theory roughly around $0.15T_F < T < 0.20T_F$. It is easy to observe that the increase of polarization pushes the minimum to high Q values, while instead the increase of temperature pushes it back towards the BCS phase. In particular we notice that the condition $\varepsilon_b = 0.25\varepsilon_F$ requires a pair-fluctuation treatment because it predicts the transition temperature BCS to normal state at $0.41T_F$ that is well above the experimental observations.

The LO_g can be compared with the LO_1 ansatz via a simple Fourier transform. In particular the pairing gap order parameter has to be an even function of the selected direction in 2D and can be treated with a cosine Fourier transform

$$\Delta_{\text{LO}_g}(x) = \sum_{n=1}^{\infty} \Delta_n \cos\left(\frac{2\pi n}{L}x\right) \tag{3.65}$$
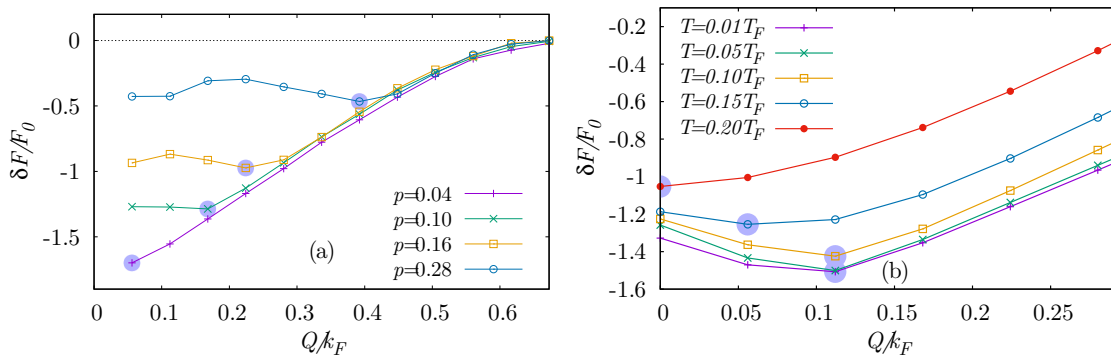
Figure 3.3: *Choosing $\varepsilon_b = 0.25\varepsilon_F$, the Helmholtz free energy difference between the LO_g (for $Q \neq 0$ and BCS at $Q = 0$) and the free Fermi gas free energy rescaled by $F_0 = 2\pi \times 10^{-2} N\varepsilon_F$: (a) at zero temperature varying the polarization, (b) at fixed polarization $p = 0.07$ increasing the temperature. The semi-transparent bullets indicate the absolute minimum position for each configuration. The dashed horizontal line in panel (a) is the free Fermi gas free energy: every time Q is too high the model mimics the free Fermi gas destroying the order parameter. From [49].*

It is straightforward that the LO_g and the LO_1 are the same phase when such Fourier transform has only one mode that doesn't vanish. The self-consistent LO_g phase is a superposition of many Fourier cosine modes and has a main mode occupation that is provided by the LO_1 ansatz that has been given to the model as initial datum. A comparison between the LO_g phase configuration versus the LO_1, choosing the main mode, indicates that the LO_g choice is always energetically favourable. This fact is true at both low and high polarizations where the LO_g and LO_1 phases almost match. In order to enlighten this overlap we studied the percentage of occupation of the main mode and we observe, in Fig. 3.4, that the overlapping between the phases never fully occur. We can then conclude that there is always a combination of modes that enhances the LO_1 phase recombining it in a more energetically favourable LO_g phase.

3.3.2   Phase diagram in the canonical ensemble

The phase transitions can be observed in the canonical ensemble at zero temperature. Theoretically we know that a finite non-zero polarization destroys the BCS phase. Then we expect a transition at very low polarizations $p < 0.02$. Above $p_{c1} = 0.02$, the Helmholtz free energy can be used to check the most favourable configuration amongst the BCS, LO_g and N_{PP}. In Fig. 3.5 it is easy to understand the shape of the phase diagram: the LO_g is dominant in a very broad range $0.02 < p < 0.58$. Above the highest threshold p_{c2} the Helmholtz free energy matches the free Fermi gas one and the pairing gap order parameter disappears. In partic-
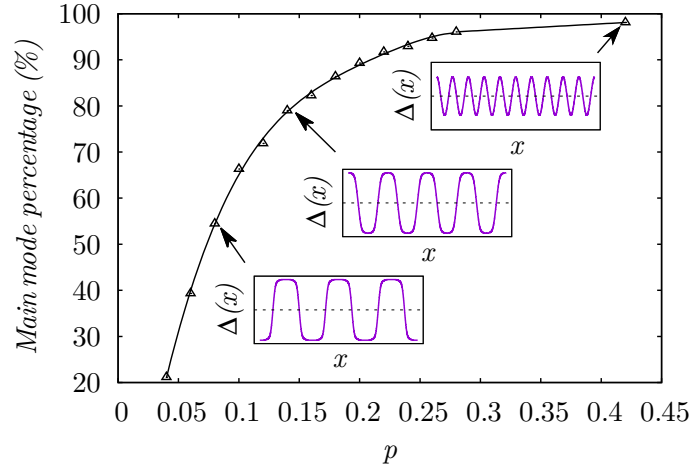
Figure 3.4: *At zero temperature, fixing $\varepsilon_b = 0.25\varepsilon_F$ and according to (3.65), for each polarization p, the weight of the main Fourier mode at that polarization is compared in percentage with respect to the other non vanishing modes. An occupancy of 100% denotes the overlapping between the LO_g and LO_1 phase that never occurs, although the inset graphs show that the energy gap parameter, $\Delta(x)$, approaches a perfect cosine function for high values of polarization. From [49].*
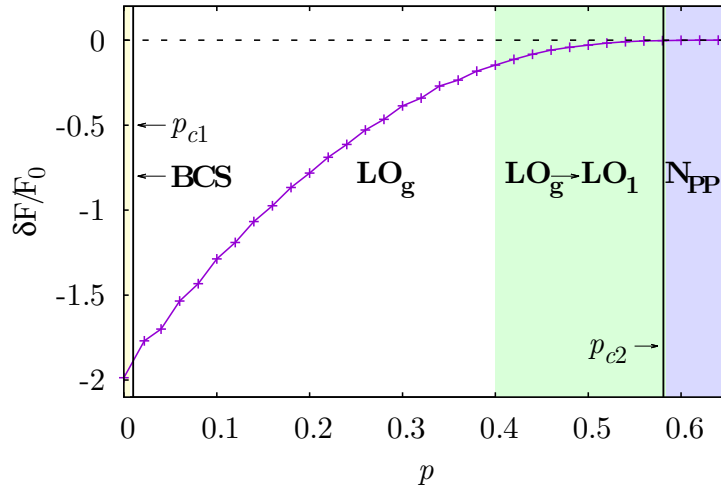

Figure 3.5: *The behaviour at zero temperature of the Helmholtz free energy F_{LO_g} with respect to the free Fermi gas one. The former is referred to the free Fermi gas through $\delta F = F_{LO_g} - F_{free}$ and re-scaled for graphic purposes through the constant $F_0 = 2\pi \times 10^{-2} N\varepsilon_F$. The transition polarization $p_{c1} \approx 0.01$, from BCS to LO_g, and $p_{c2} = 0.58$, from LO_g to N_{PP}, are denoted by bold black vertical lines. The region $p > 0.4$ denotes the LO_g phase that has a main Fourier cosine mode weight that is bigger than 95% of the whole transform. From [49].*
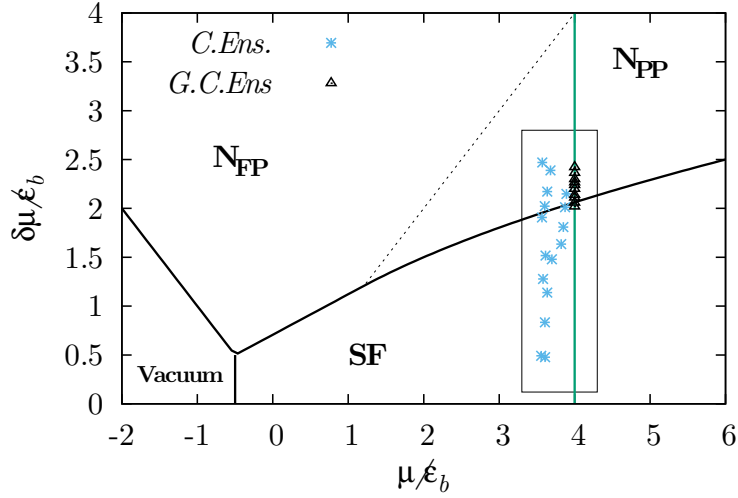
Figure 3.6: *$\delta\mu$ as a function of μ. The blue stars represent the computations $\delta\mu(\mu)$ done at zero temperature for polarizations between $0.02 \leq p \leq 0.58$. The green bold line is the choice $\mu = \varepsilon_F$ at $\varepsilon_b = 0.25\varepsilon_F$. The black triangles are the computed data in the grand canonical ensemble after the choice $\delta\mu = \varepsilon_F$ and $\delta\mu \approx p$. The fully polarized phase is not at all involved in our computations. All the computed configurations lay in the strip $0.86\varepsilon_F \leq \mu \leq 1.0\varepsilon_F$. Analytic results (black bold lines and dashed line) are from [87].*

ular, at high polarizations $0.40 < p < 0.58$ the LO_g and LO_1 phase are basically merged.

Although the canonical ensemble can tell us most of the properties of the model at zero temperature, it is interesting mainly from the experimental point of view to know the nature of phase transitions and the transition temperature of the phases we described so far. The self-consistent method we used to compute the real order parameter Δ in the Canonical Ensemble, at fixed density n and polarization p, grants us to compute the functions $\mu(n, \delta n)$ and $\delta\mu(n, \delta n)$ where $\delta n = np$ at least at zero temperature. The knowledge of those values helped us to perform a proper choice of the chemical potential μ and its variation $\delta\mu$ during the further investigations in the grand canonical ensemble. The underlying theory in 2D for the equation of state of the BCS mean field theory has been studied in [87] in the zero temperature case where the 2D integral measure allows to carry out most of the integrations analytically and study the regions of the $\delta\mu$ versus μ phase diagram that involve the transition between BCS phase and the free Fermi gas. In Fig. 3.6 we observe that the region close to $\mu = 4\varepsilon_b$ shows configurations where the LO_g phase is present and energetically favourable. The choice we kept throughout the chapter sets the binding energy $\varepsilon_b = 0.25\varepsilon_F$ that suggested us to study the chemical potential around $\mu \approx \varepsilon_F$ (it will be numerically justified in the next section). The distinction between the fully polarized normal Fermi gas N_{FP} and the partially polarized N_{PP}, which

occurs when $\delta\mu > \mu$, is not taken into account here and we will use the notion of free Fermi gas for the N_{PP} phase. We observe that both μ and $\delta\mu$ achieve an almost direct proportionality with the density n and the polarization p whenever $\delta\mu$ is high enough. Although, the model could then be affected too much by a rigid choice of μ and $\delta\mu$ we will observe that the phase transitions will occur in such high $\delta\mu$ regime.

3.3.3 Phase diagram in the grand canonical ensemble

The phase transitions can be properly studied by looking at the grand canonical ensemble. The position of the absolute minimum of the thermodynamic potential, at a fixed temperature, denotes the most energetically favourable state for the system. Moreover, the absolute minimum moves through the landscape of the thermodynamic potential, giving us an insight as to the order of each phase transition.

Instead of computing the chemical potentials $\mu_{\uparrow,\downarrow}$ self-consistently through the number equations (3.28) in the canonical ensemble, in the current grand canonical setting we must set an appropriate value for the chemical potentials that redirects to an appropriate density of particles and polarization. Thus, we need to study the behaviour of μ and $\delta\mu$ with respect to a fixed density $n = 2\pi k_F^2$ and varying polarization. At zero temperature, the BCS phase is favourable only at $p = 0$. In 2D we can analytically obtain

$$\mu_{\text{BCS}} = \frac{\pi\hbar^2}{m}n - \frac{\varepsilon_b}{2} \qquad 0 \le \delta\mu < \frac{\Delta_0}{\sqrt{2}} \tag{3.66}$$

In particular $\delta\mu$ may take any value below the Clogston-Chandrashekar (CC) limit and we cannot appreciate any net polarization. The picture, in either the FF or LO_g phase, changes and close to the CC limit a new phase arises. We consider the case of $\mu/\varepsilon_F = 1$ and then vary $\delta\mu$ through the CC limit at different binding energies. The case of the FF ansatz in 2D has been recently studied [88] and we know that there is a transition line, for each $\varepsilon_b < 0.8\varepsilon_F$, between the FF phase and the N_{PP} gas. In particular this line is above the CC limit. The LO_g phase shows a similar behaviour at least in a range of binding energies that represent the weakly-interacting regime and the region close to the 2D-inherited unitarity. As previously discussed, from equation (3.13), once we fixed the ratio l_z/k_F, we could send $(k_F a_{3D})^{-1}$ to zero and obtain a reference position for the three-dimensional unitary regime in the two-dimensional case. We take as a reference for l_z/k_F the typical values of [50].

Without an exotic phase with an inhomogeneous pairing gap, the BCS theory predicts the CC limit, in two dimensions, to occur, at zero temperature, when

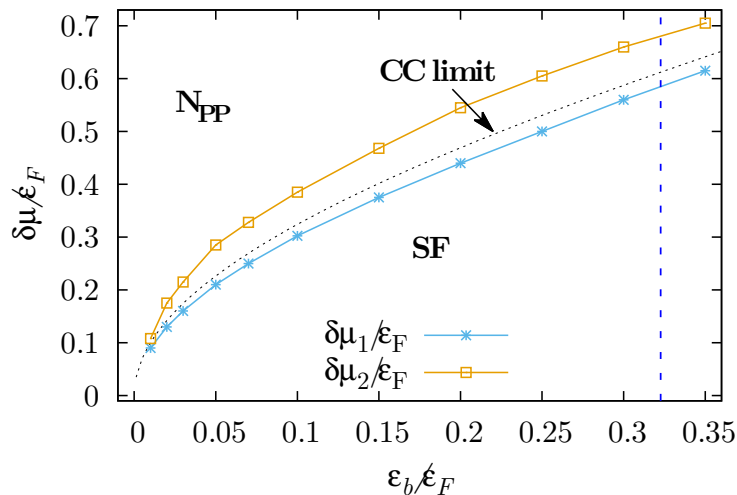$$\delta\mu_{CC} = \sqrt{\frac{\varepsilon_b^2}{2} + \mu\varepsilon_b} \tag{3.67}$$

Figure 3.7: *At zero temperature, the phase diagram of $\delta\mu$ as a function of the increasing binding energy ε_B. From left (weakly-interacting regime) to the right (inherited unitary regime), the LO_g phase embraces the CC limit (3.67) providing two different phase transition critical values: $\delta\mu_1$ from the BCS superfluid (SF) to LO_g and $\delta\mu_2(\varepsilon_B)$ from LO_g to N_{PP}. The bold blue vertical line represents the inherited unitary regime for the 2D experimental setting suggested by [50]. From [49]*

From Fig. 3.7 we can observe that the LO_g phase provides two transition lines that we will denote with $\delta\mu_1$ below the CC limit and $\delta\mu_2$ above it. In particular the $\delta\mu_2$ line is in agreement with the results provided by the FF line in [88], despite the LO_g critical line that suffers an intrinsic difficulty to be computed due to the smooth nature of the LO_g-N_{PP} transition as we will discuss later. It is interesting to observe how the reduced dimensionality of the problem, at least at zero temperature, enhances the effect of both the FF and the LO_g phase. In particular, in 3D it is possible to estimate that the FFLO phase is available for roughly 4% of the $\delta\mu$ values for which a superfluid phase is favourable, either BCS or FF. This percentage can be evaluated from the phase diagram temperature versus magnetization in [89]. Instead, the LO_g phase occupies, at a fixed binding energy, roughly 17% of the phase diagram in Fig. 3.7 at zero temperature.

The main property of the LO_g phase is that it is largely energetically favourable with respect to the FF phase computed in [88]. In Fig. 3.8 we intersect the absolute minima of the thermodynamic potential of three different theories: BCS, FF and LO_g self-consistent results. Varying the difference of chemical potentials $\delta\mu$ we span the region that is affected by the LO_g phase: the contact points of different ansatzes are the critical values $\delta\mu_1$, BCS to LO_g transition, and $\delta\mu_2$, LO_g to N_{PP} transition as referred in Fig. 3.7 in two different binding energy configurations. The FF line of minima is always above the LO_g line close to the BCS line. Instead, at high $\delta\mu$ values,
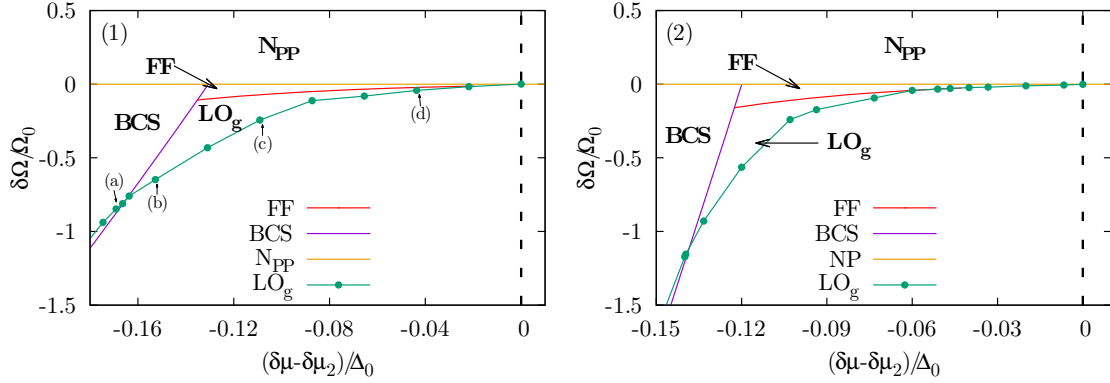
Figure 3.8: *At zero temperature, the figure shows the absolute minima of FF, BCS and LO_g mean field theory thermodynamic potentials with respect to the free Fermi gas partially polarized N_{PP}. The upper panel (1) is at $\varepsilon_b = 0.10\varepsilon_F$ while panel (2) is at $\varepsilon_b = 0.25\varepsilon_F$. The critical $\delta\mu_2$ denotes the LO_g to N_{PP} transition and Δ_0 is the BCS energy gap at zero temperature. The thermodynamic potentials are referred to the free Fermi gas one through $\delta\Omega = \Omega - \Omega_{free}$ over a re-scaling constant $\Omega_0 = 2\pi \times 10^{-3} N\varepsilon_F$. In panel (1), labels from (a) to (d) refer to Fig. 3.9 and denote the configurations for which we studied the shape of the thermodynamic potential itself. From [49]*

the model accuracy doesn't allow us to conclude whether there is, or isn't, another transition FF-LO_g. Besides, we must say that it is very inessential because at high $\delta\mu$ the pairing gap parameter reduces continuously its amplitude until it vanishes and the difference between the magnitude of the two ansatzes might be negligible. Moreover, at high $\delta\mu$ values it is, as discussed in Section 3.1, the presence of an LO_2 phase even more likely. The latter might actually be favourable with respect to both FF and LO_g.

A closer look at Fig. 3.8 suggested to us that the phase transitions at $\delta\mu_1$ and $\delta\mu_2$ might have been of a different nature. A second order phase transition moves the absolute minimum of the thermodynamic potential with continuity. It appears that the LO_g to N_{PP} transition is smooth while the BCS to LO_g one entails a certain discontinuity. Although not easy to observe, the order of the latter transition is easy to probe when we increase the binding energy ε_b towards the inherited unitary limit. In Fig. 3.9, we combine the shape of the thermodynamic potential at $\varepsilon_b = 0.10\varepsilon_F$ and its sections sliced at different $\delta\mu$ values. The comparison between panels (c) and (d) indicates the second order nature of the LO_g-N_{PP} phase transition. In this part of the phase diagram, an increase of $\delta\mu$ leads to: (i) an increase of the order parameters main frequency, (ii) the order parameter amplitude squeezes until it vanishes in $\delta\mu_2$ and (iii) the order parameter matches the LO_1 initial ansatz. The BCS-LO_g phase transition can be studied by observing the evolution of the thermodynamic potential through panels (a) and (b). It is known that the FF ansatz undergoes a first order
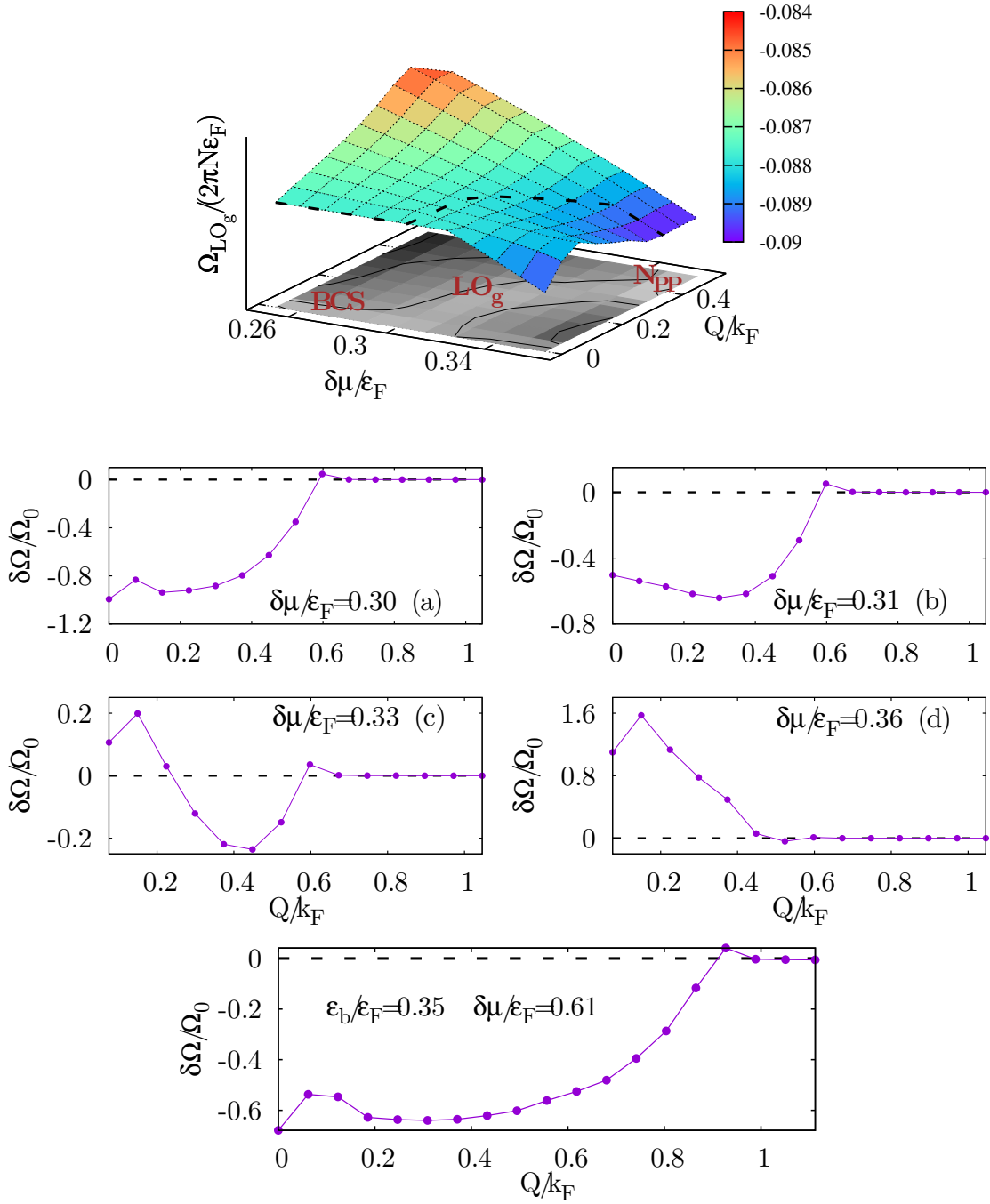
Figure 3.9: *(Upper panel) At zero temperature and $\varepsilon_b = 0.10\varepsilon_F$, the thermodynamic potential of the LO_g mean field theory as a function of $\delta\mu$ and the order parameter frequency Q. The dashed line is the evolution of the absolute minimum that is emphasized by the brighter stripe in the bottom part of the graph. (Middle panel) With reference to Fig. 3.8, at $\varepsilon_b = 0.10\varepsilon_F$ and from (a) to (d) increasing $\delta\mu$, the sections of the thermodynamic potential: (a) is before the first order BCS-LO_g transition, (b) and (c) in LO_g phase and (d) before the second order LO_g-N_{PP} transition. (Lower panel) BCS-LO_g transition at higher binding energy $\varepsilon_b = 0.35\varepsilon_F$ to emphasize the first order nature of the transition. The thermodynamic potential is referred to the free Fermi gas through $\delta\Omega = \Omega - \Omega_{free}$ over a re-scaling constant $\Omega_0 = 2\pi \times 10^{-3} N\varepsilon_F$. From [49].*
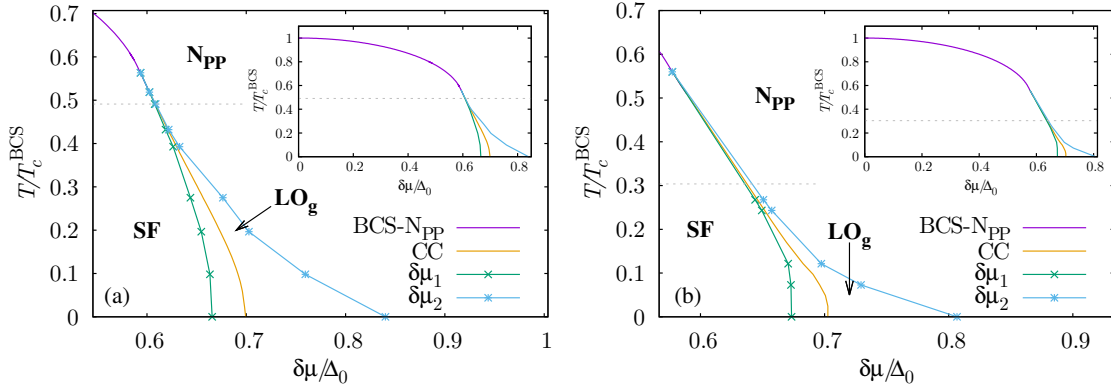
Figure 3.10: *Critical temperatures of various phase transitions with respect to the chemical potential variation $\delta\mu$ at (a) $\varepsilon_b = 0.10\varepsilon_F$ and (b) $\varepsilon_b = 0.25\varepsilon_F$. The BCS-$N_{PP}$ is the second order phase transition due to the BCS theory. CC is the Clogston-Chandrashekar limit that is completely substituted by the first order phase transition BCS-LO_g through $\delta\mu_1(T)$ and the second order phase transition LO_g-N_{PP} through $\delta\mu_2(T)$. The graph is scaled with respect to the BCS critical temperature T_c^{BCS} at $\delta\mu = 0$ and the BCS energy gap at zero temperature Δ_0. The whole graph is contained in the inset and the grey dashed line is the BKT transition temperature. From [49].*

phase transition with the BCS and, in a weakly-interacting regime, it appears to be the same case as well. Anyway, the presence of a maximum is required for a first order phase transition and at low binding energy this maximum is represented, within our accuracy, by a single point only. Indeed, it is possible to increase the binding energy thereby enhancing the shape of the phase transition and actually at $\varepsilon_b = 0.35\varepsilon_F$ the maximum becomes more evident, supporting the first order nature of the BCS-LO_g transition.

3.3.4 Finite temperature

With the zero temperature model, including the Fermi-Dirac statistics, we have actually opened up the possibility of studying the LO_g phase at finite temperatures. A rough estimation of the BCS critical temperature T_c^{BCS} can be approximated from the pairing gap equation in 2D and provides

$$T_c^{\text{BCS}} \approx \frac{2}{\pi} e^{\gamma - \log(k_F a_{2\text{D}})} T_F \tag{3.68}$$

where γ is the Euler-Mascheroni constant. Moreover, we can estimate the tri-critical point (TCP) temperature, where BCS, CC limit and FFLO phase intersect, with the numerical value

$$T_{\text{TCP}} \approx 0.56 T_c^{\text{BCS}} \tag{3.69}$$

We observe from Fig. 3.10 the critical temperatures at which the phase transitions occur. The BCS theory infers a second order phase transition between BCS

phase and N_{PP} when the temperature is above the TCP. The CC limit, that would be first order, is at finite temperature, and is entirely contained in between the LO_g transition temperatures at any relevant $\delta\mu$ value. Moreover, the order of the phase transitions is preserved: the second order phase transition between the BCS and N_{PP} phase is unaffected by an increasing temperature below TCP; the second order LO_g-N_{PP} is preserved within the accuracy described before. In the weakly-interacting regime $\varepsilon_b = 0.10\varepsilon_F$, the T_c^{BCS} is roughly $0.25T_F$. It appears that the mean field treatment requires a pair fluctuation approach to take into account the fact there is no superfluid behaviour below the BKT temperature $T_{BKT} = 0.125T_F$. Besides, we observe that most of the LO_g phase lays below T_{BKT} providing preliminary interesting results at least in the weakly-interacting regime.

3.4 Superfluid density of the LO$_g$ phase

According to [90] the superfluid density of a Fermi gas can be studied, in the canonical ensemble, by fixing the total density and the polarization. Fig. 3.5 shows that when the polarization is larger than $p \simeq 0.02$, at zero temperature, we actually meet the LO_g phase. If we fix neither μ nor $\delta\mu$ we might encounter a system where different phases coexist (the so-called phase superposition). The superfluid part of the system, if it exists, cannot react to small excitations like a normal gas: it must create a superfluid current that is related to the actual magnitude of the superfluid density contained in the coexistent phases. The case of a pairing gap order parameter that is provided with a "phase twist" must produce a superfluid current, according to [91]. Hence we modify the pairing gap in equation (3.24) using

$$\Delta(\mathbf{x}) \mapsto \Delta(\mathbf{x})e^{i\mathbf{Q}_s \cdot \mathbf{x}} \tag{3.70}$$

The superfluid velocity $\mathbf{v}_s$ associated to the twist frequency $\mathbf{Q}_s$ is given by

$$\mathbf{v}_s = \frac{\mathbf{Q}_s}{2m} \tag{3.71}$$

Moreover the Helmholtz free energy F must increase if we impose an extra flow in the superfluid phase. The shape of the free energy for small twists is shown [90] to behave like a square of the phase twist frequency magnitude around the point $F(\mathbf{Q}_s = \mathbf{0})$. In particular

$$\frac{\delta F}{V} = \frac{F(\mathbf{Q}_s) - F(\mathbf{0})}{V} \underset{|\mathbf{Q}_s| \to 0}{\approx} \frac{|\mathbf{Q}_s|^2}{2V} \left(\frac{\partial^2 F(\mathbf{Q}_s)}{\partial |\mathbf{Q}_s|^2} \right)_{\mathbf{Q}_s = \mathbf{0}} \tag{3.72}$$

The superfluid density ρ_s then can be computed from the parabolic coefficient and it is given by

$$\rho_s = 4m \left(\frac{\partial^2 F(\mathbf{Q}_s)}{\partial |\mathbf{Q}_s|^2} \right)_{\mathbf{Q}_s = \mathbf{0}} \tag{3.73}$$
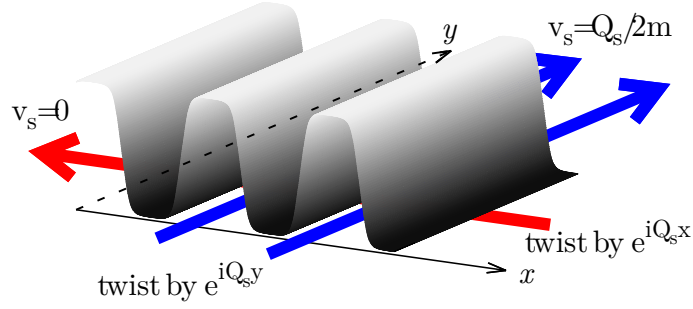
Figure 3.11: *Effect of a phase twist attached to the pairing gap parameter. The parallel direction (red line) doesn't produce any current velocity, while the perpendicular (blue line) doesn't disturb the regions where the imbalance is high (in between a valley and a peak in Fig. 3.2(a)) and lets the current flow. From [49].*

while the normal part density must be $n_n = n - \rho_s$. The definition of the macroscopic quantity superfluid velocity $\mathbf{v}_s$ gives us also a useful picture of what could mean, in our two-dimensional system, to induce a superfluid current. Due to the particular case of the LO$_g$ order parameter, the symmetry breaking, induced by neglecting a spatial direction, leads to interesting consequences in terms of the superfluidity. We can observe in Fig. 3.11 an idea of what actually might happen when we induce a superfluid density that is either parallel or perpendicular to the order parameter. We recall, from our knowledge of the LO$_g$ order parameter in Fig. 3.2, that the local imbalance is peaked where Δ is vanishing and then travels in the y direction as a barrier. Hence we cannot force a macroscopic velocity alongside x without intersecting the regions where the LO$_g$ phase is placing the imbalance. We expect instead a massive presence of superfluid density alongside the y direction where the superfluid is free to flow without touching regions where the energy gap is vanishing and could allow low-energetic excitations. In particular we define two different phase twists in equation (3.72) forcing $\mathbf{Q}_s$ to be either parallel to the pairing gap function or perpendicular. The setting $\mathbf{Q_s} = Q_s \hat{\mathbf{x}}$ doesn't produce any superfluid density. The numerical results in this case return a superfluid density that is larger than the total density. This is due to the fact that the twist method is inaccurate to predict the 4$^{\text{th}}$ order Taylor coefficient, hence it cannot really reproduce a vanishing 2$^{\text{nd}}$ order Taylor coefficient. The perpendicular case instead, choosing $\mathbf{Q_s} = Q_s \hat{\mathbf{y}}$, allows us to compute the superfluid density via the equation (3.73). Thus we briefly explain how it is possible to modify the model of Section 4.3. The matrix (3.21) now is complex valued and needs to be re-cast in a real-valued form. In order to

achieve it we have to consider again the Heisenberg equations (3.17) and perform a brand-new Bogoliubov transformation attaching the twist, as in equation (3.70), to the order parameter. The new modes will be decomposed as follows

$$
\psi_\uparrow(\mathbf{x}) = \sum_\eta \left[u_{\eta Q\uparrow}(\mathbf{x}) c_{\eta Q\uparrow} e^{-\mathrm{i}E_{\eta Q\uparrow}t} - \overline{v_{\eta Q\downarrow}(\mathbf{x})} c^*_{\eta Q\downarrow} e^{\mathrm{i}E_{\eta Q\downarrow}t} \right]
$$
$$
\psi^*_\downarrow(\mathbf{x}) = \sum_\eta \left[\overline{u_{\eta Q\downarrow}(\mathbf{x})} c^*_{\eta Q\downarrow} e^{\mathrm{i}E_{\eta Q\downarrow}t} + v_{\eta Q\uparrow}(\mathbf{x}) c_{\eta Q\uparrow} e^{-\mathrm{i}E_{\eta Q\uparrow}t} \right]
\tag{3.74}
$$

that yield

$$
M_\uparrow \begin{pmatrix} u_{\eta Q\uparrow} \\ v_{\eta Q\uparrow} \end{pmatrix} = \begin{pmatrix} -\nabla^2_\mathbf{x} - \mu_\uparrow \mathbb{1} & -\Delta(\mathbf{x})e^{\mathrm{i}\mathbf{Q}\cdot\mathbf{x}} \\ -\overline{\Delta(\mathbf{x})}e^{-\mathrm{i}\mathbf{Q}\cdot\mathbf{x}} & \nabla^2_\mathbf{x} + \mu_\downarrow \mathbb{1} \end{pmatrix} \begin{pmatrix} u_{\eta Q\uparrow} \\ v_{\eta Q\uparrow} \end{pmatrix} = E_\eta \begin{pmatrix} u_{\eta Q\uparrow} \\ v_{\eta Q\uparrow} \end{pmatrix}
\tag{3.75}
$$

Again we expect the $\uparrow$ and $\downarrow$ problem to be unitary related and that through a slightly modified transformation we can get rid of the complex exponentials in the order parameter definition. This good feature can be obtained using

$$
A = \begin{pmatrix} e^{-\frac{\mathrm{i}}{2}\mathbf{Q}\cdot\mathbf{x}} & 0 \\ 0 & e^{\frac{\mathrm{i}}{2}\mathbf{Q}\cdot\mathbf{x}} \end{pmatrix} \qquad M_\uparrow \mapsto A M_\uparrow A^*
\tag{3.76}
$$

and we get

$$
A M_\uparrow A^* = \begin{pmatrix} -\left(\nabla - \mathrm{i}\frac{\mathbf{Q}}{2}\right)^2 - \mu_\uparrow & -\Delta(\mathbf{x}) \\ -\overline{\Delta(\mathbf{x})} & \left(\nabla + \mathrm{i}\frac{\mathbf{Q}}{2}\right)^2 + \mu_\downarrow \end{pmatrix}
\tag{3.77}
$$

As it happened before we can study the $\uparrow$ problem only and we define $u_{\eta Q\uparrow} = u_{\eta Q}$ and $v_{\eta Q\uparrow} = v_{\eta Q}$. We decompose these modes on a new basis to restore a real-valued BdG matrix. It is pretty obvious that now a complex-valued function basis is required and for instance we can choose

$$
\phi_\mathbf{k}(\mathbf{x}) = \frac{e^{\mathrm{i}\mathbf{k}\cdot\mathbf{x}}}{\sqrt{V}}
$$

defining consequently

$$
u_{\eta Q} = \sum_\mathbf{k} A^{(\eta Q)}_\mathbf{k} \phi_\mathbf{k} \qquad v_{\eta Q} = \sum_\mathbf{k} B^{(\eta Q)}_\mathbf{k} \phi_\mathbf{k}
$$

We plug this choice into the BdG equation and apply the Hermitian product of the Hilbert space $L^2(V, d\mathbf{x})$ to isolate a single mode. We require $\Delta(\mathbf{x})$ to be real-valued, one-direction dependent only and to be an $\mathrm{LO_g}$ function. Moreover we define

$$
\Delta_{k'_1 k_1} = \frac{1}{L} \int_{-L/2}^{L/2} dx_1 \ \cos((k'_1 - k_1)x_1)\Delta(x_1)
\tag{3.78}
$$

As in Section 4.3 we obtain a diagonal matrix in k_2 that can be fixed and removed from the equations

$$
\sum_{k_1} \left\{ \left[\left(\mathbf{k} - \frac{\mathbf{Q}}{2}\right)^2 - \mu_\uparrow \right] A^{(\eta Q k_2)}_{k_1} \delta_{k'_1 k_1} - \Delta_{k'_1 k_1} B^{(\eta Q k_2)}_{k_1} \right\} = E_{\eta Q k_2} \sum_{k_1} A^{(\eta Q k_2)}_{k_1} \delta_{k'_1 k_1}
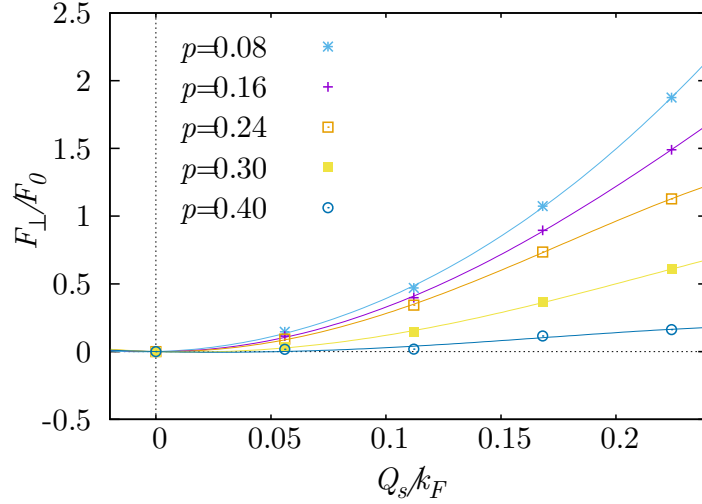\tag{3.79}
$$

Figure 3.12: *The perpendicular variation of the Helmholtz free energy $\delta F_\perp$ as a function of the phase phase twist, for various polarizations. The free energy variation is given by $\mathbf{Q}_\perp = Q_s \hat{y}$ and $\delta F_\perp = F(\mathbf{Q}_\perp) - F(\mathbf{0})$ over a rescaling constant $F_0 = 2\pi \times 10^{-3} N \varepsilon_F$. The continuous lines are data fits of a two-parameter polynomial curve $ax^2 + bx^4$. The parabolic dependency in Q_s can only be seen in the perpendicular case. The parabolic coefficient a is proportional to the superfluid part of the system using the equation (3.73). From [49].*

$$\sum_{k_1} \left\{ -\Delta_{k_1' k_1} A_{k_1}^{(\eta Q k_2)} - \left[\left(\mathbf{k} + \frac{\mathbf{Q}}{2} \right)^2 - \mu_\downarrow \right] B_{k_1}^{(\eta Q k_2)} \delta_{k_1' k_1} \right\} = E_{\eta Q k_2} \sum_{k_1} B_{k_1}^{(\eta Q k_2)} \delta_{k_1' k_1} \tag{3.80}$$

Finally we define a new energy function

$$\varepsilon_{k_1' k_1}^\sigma (k_2, \mathbf{Q}) = \delta_{k_1' k_1} \left[\left(\mathbf{k} - \operatorname{sgn}(\sigma) \frac{\mathbf{Q}}{2} \right)^2 - \mu_\sigma \right] \tag{3.81}$$

and we re-introduce a cut-off $|k_1| \leq \bar{n}(k_2)$. The model can be solved numerically in the same way as before, using the diagonalisation of matrix (3.62). However, the choice of the cut-off energies has to be matched between the two methods to obtain the same results of the free Helmholtz energy in the original model and the superfluid one at $Q_s = 0$. Once done it is necessary to double check that the new model has the same accuracy and independence from the cut-off. In Fig. 3.12 we show the shape of the variation of Helmholtz free energy under a phase twist Q_s in the perpendicular direction, increasing the twist frequency magnitude. The results have been tested with a fit containing a linear term in Q_s that turned out to be null within the errors on $\delta F_\perp$ and Q_s. As previously remarked, the only way to increase the precision of this method is to reduce the gap between the box modes. This can be done by increasing the number of particles but might cause several troubles in terms of computational costs. Previous computations related to
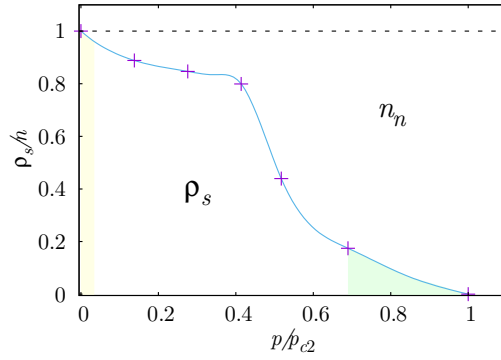
Figure 3.13: *The ratio between the superfluid density ρ_s and the total density n with respect to the polarization p. At $\varepsilon_b = 0.25\varepsilon_F$ the polarization is rescaled by the critical polarization $p_{c2} = 0.58$ at which the LO_g-N_{PP} transition occurs. The green and yellow regions correspond to the $LO_g{\rightarrow}LO_1$ and BCS regions of Fig. 3.5 respectively. The bold line is a guide line. From [49].*

the FF phase [92], using similar methods, have been able to dramatically increase the accuracy of Q_s, to be roughly 10 times better that our resolution. Anyway, the parabolic coefficients, at least in the perpendicular case are meaningful and give a good idea of the superfluidity of the LO_g phase in 2D. We observe that an increase of polarization increases the frequency of the pairing gap, as remarked in Fig. 3.2(c). The local imbalance becomes more spread in space and triggers the decrease of the superfluid density. Using these results it has been possible to compute, with sufficient precision, the shape of the superfluid density as a function of the polarization. Fixing $\varepsilon_b = 0.25\varepsilon_F$, at zero temperature, we can increase the polarization between the critical values $p_{c1} \approx 0.02$ and $p_{c2} = 0.58$ and study the variation of the parabolic coefficients in Fig. 3.12. In Fig. 3.13 we present the results of the superfluid density ρ_s and normal phase density n_n at different polarizations.

Chapter 4

The dimensional crossover of a strongly-interacting Fermi gas

In this chapter we address the interplay between the BCS-BEC crossover and the reduction of dimensionality below three dimensions (3D). Experimentally an ultracold gas is contained in a chamber by employing different trapping methods and it occurs that a well engineered geometrical combination of traps grants the access to regimes [93, 94] in which the dynamic of the system happens on a two-dimensional plane (2D) or in one dimension. Reaching these configurations involves typically three harmonic traps that freeze out one or two directions depending on the ratio between the harmonic oscillator frequencies along the orthogonal axes. Specific techniques can be used in the 2D case in order to obtain either a single 2D disk [95] or a pancake of almost-independent 2D layers utilizing a CO_2 laser standing wave trap [60, 65]. An eventual residual presence of coupling between different layers, in the latter case, or a similar magnitude between the typical confinement energy and the Fermi energy of the system is often called quasi-2D regime.

The interest for these low-dimensional systems is mainly due to the fact that they provide a benchmark to explore phenomena that are boosted or triggered by strong fluctuations of the superfluid phase. Also, the presence of the Berezinskii-Kosterlitz-Thouless quasi-long range phase transition recovers the superfluidity [96–98] that would be otherwise denied by the Mermin-Wigner theorem in 2D and 1D, while a 2D Fermi gas with spin population imbalance may reveal the existence of exotic inhomogeneous superfluid phases since they would produce an enhanced signature with respect to their 3D counterparts [49, 99, 100].

Although the BCS-BEC crossover has been investigated both in 3D and pure 2D regimes [51, 66, 95], and the 3D case has been widely experimentally probed, the behaviour of the BCS-BEC crossover when a third direction is progressively frozen out is still to be understood. Theoretically it is known that when approaching 2D,

the mean field (MF) theory of the crossover fails to predict the behaviour of the thermodynamic quantities [87] when the dynamics spans from a weakly to a strongly interacting regime. Though the implementation of beyond MF methods, quantum Monte Carlo simulations [101–106] and Gaussian pair fluctuations (GPF) [47, 107] provided a remarkable improvement. Moreover, experimentally, the trapping techniques previously described must deal with an intrinsic non-uniform particle density and, at the same time, with how properly the extra directions have been frozen out. These limitations open up the need for an effective theory that connects the BCS-BEC crossover in the 3D to the 2D regime via a continuous squeezing of a selected direction. It is also important to establish criteria and conditions that quantitatively separate different dimensional configurations.

The recent implementation of a hard-wall (HW) trapping potential [68, 95] as a confining configuration for ultracold gases allowed to obtain apparata that display uniform particle density and don't rely on models involving local density approximation methods. It better reproduces dilute gases and reduces the occurrence of three-body scattering events. Motivated by these developments we address the study of an ultracold interacting atomic Fermi gas with two balanced spin populations when the dimensionality is brought from 3D to 2D. When the interactions are tuned by a broad Feshbach resonance, we explore the BCS-BEC crossover and how it is affected by the progressive reduction of dimensionality.

In 3D, the interacting system can be characterized, through the BCS-BEC crossover, by a unique dimensionless tuning parameter, $1/(k_F^{3D} a_{3D})$, where k_F^{3D} is the 3D Fermi wave vector and a_{3D} is the 3D s-wave scattering length. The weakly-interacting regime is denoted by a negative a_{3D}. Strong interactions occur when it is positive and its divergence, for $1/(k_F^{3D} a_{3D}) = 0$, is denoted as unitarity. In 2D, the BCS-BEC crossover is tuned by $\ln(k_F^{2D} a_{2D})$, where k_F^{2D} is the 2D Fermi wave vector and a_{2D} is the 2D s-wave scattering length. Moreover, the 2D BCS-BEC crossover doesn't have an evident definition of unitarity. On the other side, if we choose to confine the gas through a HW potential box, we can describe the dimensionality of the system by the ratio of the side lengths of such box.

Realizing a quasi-2D environment is a task that experimentally has been successfully accomplished, via different techniques. In particular, we would like to stress how the combination of HW potential shape (impenetrable outside a fixed radius) can be employed in all three directions with different methods, e.g. an in-plane configuration (xy plane), with large radius, compared with an optical lattice confinement on the remaining axial direction. The latter confinement, alongside z, provides a profile of the particle density, $n(z)$, that mimics a narrow HW potential. We can address the theoretical description of this setup combining different methods to reach a satisfactory qualitative description of the BCS-BEC crossover,

beyond MF theory, varying the axial confinement length.

A balanced 2-spin population Fermi gas, when confined in a HW box, gives rise to finite volume effects that can be studied, at the MF level, by solving the appropriate Bogoliubov-de Gennes (BdG) equations. A beyond MF approach, in this case, is not straightforward viable for an actual self-consistent computation of the superfluidity's order parameter, but we will show that it is possible to identify an effective region, in the centre of the axial side, in which both particle density and order parameter display a uniform constant behaviour. This remarkable feature allows us to investigate the system via a hybrid thermodynamic limit, with in-plane infinite area plus periodic boundary conditions (PBC) on the axial direction. The side length, l_z, must then play the role of a tuning parameter for the dimensional crossover from 3D to quasi-2D and eventually to 2D, since when it is of similar magnitude to the other two side lengths it represents a full 3D thermodynamic limit.

We show that the case of a non-interacting Fermi gas, with HW or PBC on a selected direction, gives clear motivations to the use of the axial side length, l_z, as dimensional tuning parameter. We discuss the proper interaction parameter, l_z/a_{3D}, that tunes the BCS-BEC crossover for several values of l_z and we compute the thermodynamic variables from weak to strongly-interacting regime. The chemical potential matches the values expected for the 3D and 2D regimes when the suitable limit for l_z is taken. The quasi-2D regime is shown to be a dimensional configuration in which the thermodynamic variables behave differently from the 3D and 2D cases and, moreover, distinguish the quasi-2D configuration as a separate environment. The study of the superfluid critical velocity turns out to be the pivotal parameter to quantitatively separate the different dimensionality. It is well know that in 3D the MF predicts a maximum value for the superfluid critical velocity, $v_c^{\max}$, very close to the unitarity, at $1/(k_F^{3D} a_{3D}) \simeq 0.07$. The behaviour of the location of this maximum in the BCS-BEC crossover, $(l_z/a_{3D})_{v_c^{\max}}$, while varying l_z, marks the transition between different dimensional configurations. The quasi-2D regime also predicts the presence of pair-breaking excitations along the z direction, according to what is experimentally expected from a system that is almost-2D-confined but fails to freeze out completely the z direction. The dynamic structure factor, that can be directly probed by Bragg spectroscopy, is computed and provides a good description of these axial excitations due to the quasi-2D regime.

4.1 BdG equations for an axially confined Fermi gas

We start our investigation dealing with the case of a balanced 2-spin population Fermi gas confined in a 3D box. In particular, we model the in-plane xy-directions using PBC with a large length L, in order to mimic the thermodynamic limit, while in the z-direction the fermionic fields are treated with two different conditions, firstly with HW potential, which implies that such fields must vanish at a certain distance, $l_z^{\mathrm{hw}}/2$, from the centre. This setting is then compared with the case of PBC, with l_z^{pbc} length, on the axial direction as well. In both cases we consider the conditions $l_z^{\mathrm{hw}} \ll L$ and $l_z^{\mathrm{pbc}} \ll L$.

4.1.1 Theoretical model

In presence of a broad Feshbach resonance and in the regime of a dilute Fermi gas, at zero temperature, we model the interactions via a two-body contact potential, with spatial in-plane coordinates, $\mathbf{x} = (x, y)$, plus the axial z, combined in the shorthand notation $(\mathbf{x}, z)$. The system is then well described by the grand canonical Hamiltonian density (see Chap. 2),

$$
\begin{aligned}
\mathcal{H} = \sum_{\sigma=\uparrow,\downarrow} \psi_\sigma^\dagger(\mathbf{x}, z) \left(-\frac{\hbar^2}{2m}\nabla^2 - \mu + V_{\mathrm{ext}}(z) \right) \psi_\sigma(\mathbf{x}, z) \\
- U_0 \psi_\uparrow^\dagger(\mathbf{x}, z)\psi_\downarrow^\dagger(\mathbf{x}, z)\psi_\downarrow(\mathbf{x}, z)\psi_\uparrow(\mathbf{x}, z),
\end{aligned}
\tag{4.1}
$$

where ψ_σ are the annihilation field operators for the two spin populations labelled by $\sigma =\uparrow,\downarrow$, μ is the chemical potential, m is the mass of the fermions, and $U_0 > 0$ is the s-wave attractive interaction coupling constant of the contact potential. Moreover, in the case of HW potential we define the external potential

$$
V_{\mathrm{ext}}(z) = \begin{cases} 0 & \text{if } |z| < l_z^{\mathrm{hw}}/2 \\ \infty & \text{otherwise.} \end{cases}
\tag{4.2}
$$

which instead is set to zero, all over the real axis, in the case of PBC alongside z. We can solve the associated BdG problem in the Heisenberg picture by moving the external potential constraint onto the initial data of the BdG equations, setting $V_{\mathrm{ext}} = 0$, and obtaining

$$
\begin{cases} i\partial_t \psi_\sigma(\mathbf{x}, z, t) = [\mathcal{H}, \psi_\sigma(\mathbf{x}, z, t)]_-\,, \\[2mm] \psi_\sigma(\mathbf{x}, -l_z^{\mathrm{hw}}/2, t) = \psi_\sigma(\mathbf{x}, l_z^{\mathrm{hw}}/2, t) = 0, \end{cases}
\tag{4.3}
$$

where $[\ ,\ ]_-$ is the operators commutator. The initial data in the PBC instead reads

$$
\psi_\sigma(\mathbf{x}, -l_z^{\mathrm{pbc}}/2, t) = \psi_\sigma(\mathbf{x}, l_z^{\mathrm{pbc}}/2, t).
\tag{4.4}
$$

The MF approximation in Eq. (4.1) is introduced via the order parameter,

$$\Delta(\mathbf{x}, z) = U_0 \langle \psi_\downarrow(\mathbf{x}, z) \psi_\uparrow(\mathbf{x}, z) \rangle_{\text{GS}}, \tag{4.5}$$

where GS is the ground state, which simplifies Eq. (4.3) to

$$\mathrm{i}\partial_t \psi_\sigma(\mathbf{x}, z, t) = \left[-\frac{\hbar^2}{2m}(\nabla_\mathbf{x}^2 + \partial_z^2) - \mu \right] \psi_\sigma(\mathbf{x}, z, t) + + \mathrm{sgn}(\sigma)\Delta(\mathbf{x}, z)\psi_{\bar\sigma}^\dagger(\mathbf{x}, z, t). \tag{4.6}$$

denoting with $\bar\sigma$ the opposite of the σ-spin and defining $\mathrm{sgn}(\uparrow) = -\mathrm{sgn}(\downarrow) = 1$. We use the Bogoliubov automorphism on the fermionic fields that defines the quasi-particle modes $u_{\eta\sigma}$ and $v_{\eta\sigma}$ altogether with the quasi-particle creation and annihilation operators $c_{\eta\sigma}^\dagger$ and $c_{\eta\sigma}$ via

$$\psi_\uparrow(\mathbf{x}, z, t) = \sum_\eta \left[u_{\eta\uparrow}(\mathbf{x}, z)c_{\eta\uparrow}e^{-\mathrm{i}E_{\eta\uparrow}t} + + \overline{v_{\eta\downarrow}(\mathbf{x}, z)}c_{\eta\downarrow}^\dagger e^{\mathrm{i}E_{\eta\downarrow}t} \right],$$

$$\psi_\downarrow^\dagger(\mathbf{x}, z, t) = \sum_\eta \left[\overline{u_{\eta\downarrow}(\mathbf{x}, z)}c_{\eta\downarrow}^\dagger e^{\mathrm{i}E_{\eta\downarrow}t} + - v_{\eta\uparrow}(\mathbf{x}, z)c_{\eta\uparrow}e^{-\mathrm{i}E_{\eta\uparrow}t} \right], \tag{4.7}$$

which leads to the familiar form of the BdG equations

$$\begin{pmatrix} -\frac{\hbar^2}{2m}(\nabla_\mathbf{x}^2 + \partial_z^2) - \mu & \Delta(\mathbf{x}, z) \\ \overline{\Delta(\mathbf{x}, z)} & \frac{\hbar^2}{2m}(\nabla_\mathbf{x}^2 + \partial_z^2) + \mu \end{pmatrix} \begin{pmatrix} u_{\eta\sigma} \\ v_{\eta\sigma} \end{pmatrix} = E_{\eta\sigma} \begin{pmatrix} u_{\eta\sigma} \\ v_{\eta\sigma} \end{pmatrix}. \tag{4.8}$$

We reduce the complexity of the problem via the standard particle-hole symmetry unitary transformation,

$$\begin{pmatrix} u_{\eta\downarrow} \\ v_{\eta\downarrow} \end{pmatrix} = \begin{pmatrix} -\overline{v_{\eta\uparrow}} \\ \overline{u_{\eta\uparrow}} \end{pmatrix}, \qquad E_{\eta\downarrow} = -E_{\eta\uparrow}, \tag{4.9}$$

remove the $\downarrow$-components, and set $u_\eta = u_{\eta\uparrow}$ and $v_\eta = v_{\eta\uparrow}$. Due to the balanced condition on the spin populations, the particle density profile is given by

$$n(\mathbf{x}, z) = 2 \sum_\eta |u_\eta(\mathbf{x}, z)|^2 f(E_{\eta\sigma}), \tag{4.10}$$

and the order parameter profile by

$$\Delta(\mathbf{x}, z) = U_0 \sum_\eta u_\eta(\mathbf{x}, z)\overline{v_\eta(\mathbf{x}, z)}f(E_{\eta\sigma}), \tag{4.11}$$

introducing the zero temperature Fermi-Dirac distribution,

$$f(x) = \frac{1}{1 + e^{x/(k_B T)}} \xrightarrow{T \to 0} \Theta(-x), \tag{4.12}$$

where T is the temperature and Θ is the Heaviside step function. The phase choice on u_η and v_η allows us to decompose them on a real-valued Hilbert basis. For the

in-plane part of the system we use an all-real-valued Hilbert space basis which runs over non-negative integers,

$$\chi_n(x) = \begin{cases} 1/\sqrt{L} & \text{if } n = 0, \\ \sqrt{2/L}\cos(\beta_n x) & \text{if } n \neq 0 \text{ and } n \text{ is even,} \\ \sqrt{2/L}\sin(\beta_{n+1} x) & \text{if } n \text{ is odd,} \end{cases} \tag{4.13}$$

where $\beta_n = n\pi/L$. A further combination of this basis maps the 2D portion of the system (along x and y) via the tensor product,

$$\chi_{\mathbf{n}}^{(2)}(\mathbf{x}) = \chi_{n_1}(x) \otimes \chi_{n_2}(y), \tag{4.14}$$

with free eigenvalues

$$\frac{2m}{\hbar^2}\varepsilon_n = \begin{cases} \beta_n^2 & \text{if } n \text{ is even,} \\ \beta_{n+1}^2 & \text{if } n \text{ is odd.} \end{cases} \tag{4.15}$$

solving $-\hbar^2/(2m)\partial_x^2\chi_n(x) = \varepsilon_n\chi_n(x)$.

The HW boundaries are recovered through

$$\Phi_q(z) = \begin{cases} \sqrt{2/l_z^{\mathrm{hw}}}\cos(\alpha_q z) & \text{if } q \text{ is odd,} \\ \sqrt{2/l_z^{\mathrm{hw}}}\sin(\alpha_q z) & \text{if } q \text{ is even,} \end{cases} \tag{4.16}$$

for each $q \in \mathbb{N}_0$ (excluding $q = 0$), introducing the Fourier modes $\alpha_q = q\pi/l_z^{\mathrm{hw}}$ that solve $-\partial_z^2\Phi_q(x) = \alpha_q^2\Phi_q(x)$. We define the eigenenergies,

$$\varepsilon_{\mathbf{n},q} = \varepsilon_{n_1} + \varepsilon_{n_2} + \hbar^2/(2m)\alpha_q^2 \tag{4.17}$$

where $\mathbf{n} \in \mathbb{N}^2$ and $q \in \mathbb{N}_0$ and decompose all the quantities onto this basis getting

$$u_\eta(\mathbf{x}, z) = \sum_{\mathbf{n},q} A_{\mathbf{n},q}^{(\eta)}\left[\chi_{\mathbf{n}}^{(2)}(\mathbf{x}) \otimes \Phi_q(z)\right]$$

$$v_\eta(\mathbf{x}, z) = \sum_{\mathbf{n},q} B_{\mathbf{n},q}^{(\eta)}\left[\chi_{\mathbf{n}}^{(2)}(\mathbf{x}) \otimes \Phi_q(z)\right] \tag{4.18}$$

The BdG equations (4.8) then reduce to the matrix form

$$\sum_{q' \in \mathbb{N}_0} \begin{pmatrix} (\varepsilon_{\mathbf{n},q} - \mu)\delta_{qq'} & \Delta_{qq'} \\ \Delta_{qq'} & (-\varepsilon_{\mathbf{n},q} + \mu)\delta_{qq'} \end{pmatrix} \begin{pmatrix} A_{\mathbf{n},q'}^{(\eta)} \\ B_{\mathbf{n},q'}^{(\eta)} \end{pmatrix} = E_{\eta,\mathbf{n}} \begin{pmatrix} A_{\mathbf{n},q}^{(\eta)} \\ B_{\mathbf{n},q}^{(\eta)} \end{pmatrix} \qquad \text{for each } \mathbf{n} \in \mathbb{N}^2, \tag{4.19}$$

where $\delta_{qq'}$ is the Kronecker symbol and we defined

$$\Delta_{qq'} = \int_{-l_z^{\mathrm{hw}}/2}^{l_z^{\mathrm{hw}}/2} dz\,\Phi_q(z)\Delta(z)\Phi_{q'}(z), \tag{4.20}$$

since, *due to the symmetry of the system*, the order parameter must be constant on **x**. The PBC case can be solved with the same formalism of Eq. (4.19), just replacing $\Phi_q(z)$ with

$$\chi_q^{\text{pbc}}(z) = \begin{cases} 1/\sqrt{l_z^{\text{pbc}}} & \text{if } q = 0 \\ \sqrt{2/l_z^{\text{pbc}}} \cos\left(\gamma_q x\right) & \text{if } 0 \neq q \text{ is even} \\ \sqrt{2/l_z^{\text{pbc}}} \sin\left(\gamma_{q+1} x\right) & \text{if } q \text{ is odd} \end{cases}, \qquad (4.21)$$

and the free eigenvalues

$$\frac{2m}{\hbar^2}\varepsilon_q^{\text{pbc}} = \begin{cases} \gamma_q^2 & \text{if } q \text{ is even} \\ \gamma_{q+1}^2 & \text{if } q \text{ is odd} \end{cases}, \qquad (4.22)$$

defining $\gamma_q = q\pi/l_z^{\text{pbc}}$, which substitutes α_q in Eq. (4.17), and re-defining

$$\Delta_{qq'} = \int_{-l_z^{\text{pbc}}/2}^{l_z^{\text{pbc}}/2} dz \chi_q^{\text{pbc}}(z)\Delta(z)\chi_{q'}^{\text{pbc}}(z), \qquad (4.23)$$

which, anyway, is kept independent from the in-plane coordinates.

We solve both problems, HW and PBC, computing the order parameter and the axial particle density profile self-consistently, in the canonical ensemble, fixing the total number of particles N. The contact interaction, in the HW case, cannot be straightforwardly renormalized, as explained in the next section, while the renormalisation of the PBC case is treated in details in Sec. 4.2.2. However, we can introduce an energy cut-off E_c on Eq. (4.19). A large cut-off cures the ultra-violet divergence of the interaction and allows us to neglect the dependency on z of the bare interaction strength U_0. It is possible to renormalise U_0 to a constant interaction strength g (see Sec. 4.1.2) by relating them through

$$\frac{1}{g} = \frac{1}{U_0} + \mathcal{O}(U_0, E_c). \qquad (4.24)$$

for large E_c values. The g parameter then can be fixed as a constant and tuned to span the BCS-BEC crossover. Despite that the PBC case can be exactly renormalized, establishing a relation between the scattering length and the binding energy, in this section we treat both HW and PBC with large cut-off and constant g in order to ensure a useful comparison of the two cases across the BCS-BEC crossover. An iterating routine can solve Eq. (4.19) updating the chemical potential, μ, until the exact number of particles is reached.

4.1.2 Renormalisation with HW boundaries

We describe how to exactly treat the renormalisation of the contact potential when the system boundaries are assumed to be hard walls. The renormalisation

typically provides a connection between the bare interaction strength, U_0, and the binding energy. Alternatively, like in the 3D BCS regime, U_0 becomes a function of the scattering length. We show why to fully treat the HW case requires the solution of a system with an extra variable, namely the centre-of-mass coordinate, which would make our BdG equations to be very hard to compute. Moreover, we show how to obtain the constant interaction strength, g, from the bare U_0, in order to make sense of Eq. (4.24).

In the 3D thermodynamic limit, the two-body scattering cannot explicitly depend on the centre-of-mass position of the colliding particles. For a system with infinite volume, we can examine the scattering process from the centre-of-mass frame without loss of generality, while for the PBC it can be thought of as a system with infinite copies of itself placed one next to the other, again falling in a case in which the centre-of-mass frame can be used, removing such coordinate from the problem. It becomes clear from the last remark that both centre-of-mass and relative position must be affected by HW boundaries: the scattering occurring close to the boundaries (centre-of-mass position) must be highly suppressed because there are very few particles in that region (almost zero particle density). In other words, the scattering close to the boundaries counts less in the relation between bare interaction strength and the scattering length.

The two-body problem can be, anyway, fully solved in the HW case, where the resulting two-body time-independent free Schrödinger equation is

$$\mathcal{H}_{\text{hw}}^{(0)}\Psi(\mathbf{x}, z) = E\Psi(\mathbf{x}, z), \tag{4.25}$$

with $E \in \mathbb{R}$ and Hamiltonian

$$\mathcal{H}_{\text{hw}}^{(0)} = -\frac{\hbar^2}{2m}\left[2\nabla_{\mathbf{x}}^2 + \partial_{z_1}^2 + \partial_{z_2}^2\right] + V_{\text{ext}}(z_1) + V_{\text{ext}}(z_2) \tag{4.26}$$

where V_{ext} is defined in Eq. (4.2) for a fixed l_z^{hw}, z_1 and z_2 are the axial positions of the two particles and $\mathbf{x}$ is the in-plane components of the relative position. The free Green's function, $\mathcal{G}_0(\mathbf{x}, z_1, z_2; E)$, is defined as the inverse of the resolvent operator of $\mathcal{H}_{\text{hw}}^{(0)}$, which amounts to solve

$$(\mathcal{H}_{\text{hw}}^{(0)} - E)\mathcal{G}_0(\mathbf{x}, z_1, z_2; E) = -\delta(\mathbf{x})\delta(z_1)\delta(z_2) \tag{4.27}$$

The anti-Fourier transform, in presence of HW confinement, can be computed using the HW case's Hilbert basis Φ_q and its eigenvalues α_q, given by Eq. (4.16), combined with the plane wave basis to map out the in-plane part, treated with PBC. We can obtain the anti-Fourier transform of the Green's function as

$$\mathcal{G}_0(\mathbf{x}, z_1, z_2; E) = \sum_{\substack{\mathbf{k} \in \mathbb{Z}^2 \\ q, q' \in \mathbb{N}_0}} \tilde{\mathcal{G}}_0(\mathbf{k}, q, q'; E)\Phi_q(z_1)\Phi_{q'}(z_2)\frac{e^{i\mathbf{k}\cdot\mathbf{x}}}{L^2}, \tag{4.28}$$

as well as the distribution kernel of the Dirac delta

$$\delta(\mathbf{x})\delta(z_1)\delta(z_2) = \sum_{\mathbf{k}\in\mathbb{Z}^2}\sum_{q,q'\text{ odd}} \Phi_q(z_1)\Phi_{q'}(z_2)\frac{e^{i\mathbf{k}\cdot\mathbf{x}}}{L^2}. \tag{4.29}$$

Plugging Eq. (4.28) and Eq. (4.29) back in Eq. (4.27) we obtain the Fourier modes

$$\tilde{\mathcal{G}}_0(\mathbf{k}, q, q'; E) = \begin{cases} -(E_{\mathbf{k},q,q'} - E)^{-1} & q, q' \text{ odd} \\ \\ 0 & \text{otherwise} \end{cases} \tag{4.30}$$

where we introduced the dispersion relation $E_{\mathbf{k},q,q'} = \frac{\hbar^2}{2m}(2\mathbf{k}^2 + \alpha_q^2 + \alpha_{q'}^2)$. We then consider the interacting case which defines the full scattering Hamiltonian by

$$\mathcal{H}_{\text{hw}} = \mathcal{H}_{\text{hw}}^{(0)} - U_0\delta(\mathbf{x} - \mathbf{y})\delta(z_1 - z_2), \tag{4.31}$$

The interacting Green's function $\mathcal{G}(\mathbf{x} - \mathbf{y}, z_1, z_2; E)$ is then given by

$$\mathcal{G}(\mathbf{x} - \mathbf{y}, z_1, z_2; E) = \mathcal{G}_0(\mathbf{x} - \mathbf{y}, z_1, z_2; E) - \frac{\mathcal{G}_0(\mathbf{x}, z_1, 0; E)\mathcal{G}_0(\mathbf{y}, 0, z_2; E)}{U_0^{-1} + \mathcal{G}_0(0, z_{\text{cm}}/2, z_{\text{cm}}/2; E)} \tag{4.32}$$

where $z_{\text{cm}} = z_1 + z_2$ is the the centre-of-mass position. The bare interaction strength must create a pole in the interacting Green's function, at a negative binding energy, $-|E|$, solving

$$0 = U_0^{-1} + \mathcal{G}_0(0, z_{\text{cm}}/2, z_{\text{cm}}/2; -|E|), \tag{4.33}$$

which returns U_0 as a function of the binding energy, $-|E|$, as follows

$$\frac{1}{U_0(z_{\text{cm}})} = \frac{1}{L^2}\sum_{\mathbf{k}\in\mathbb{Z}^2}\sum_{q,q'\text{ odd}} \frac{\Phi_q(z_{\text{cm}}/2)\Phi_{q'}(z_{\text{cm}}/2)}{E_{\mathbf{k},q,q'} + |E|}. \tag{4.34}$$

The bare-interaction strength assumes an explicit dependence on the centre-of-mass position and such two-body scattering cannot be implemented directly in our solution scheme of Eq. (4.3) as the fields would take a dependency from another co-ordinate. This would require to solve a system with four variables, both in the HW and PBC case. The computational complexity would rise too much. Also, including z_{cm}, raises the dimensionality of $U_0(z_{\text{cm}})^{-1}$ to *energy× (length)*^{4} and cannot be compared with the bare interaction strength in the 3D case, which is *energy× (length)*^{3}, as it has been done in Ref. [108].

Despite these hurdles we successfully attempted a different renormalisation scheme, introducing a cut-off energy E_c. It has been shown [49, 76] that a cut-off energy renormalises, the order parameter, in the BdG equations scheme, into

$$\Delta(z) = g_{\text{eff}}(z, E_c)\sum_{|E_\eta|<E_c} u_\eta(\mathbf{x}, z)\overline{v_\eta(\mathbf{x}, z)}f(E_\eta), \tag{4.35}$$
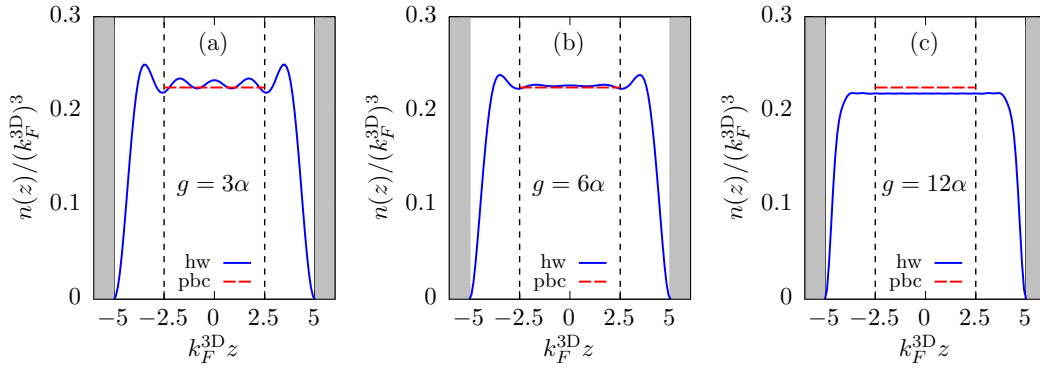
Figure 4.1: *The particle density profile $n(z)$ as a function of the axial displacement z, for hard-wall boundaries at $k_F^{3D} l_z^{hw} = 10$ (solid blue) and PBC at $k_F^{3D} l_z^{pbc} = 5$ (dashed red) across the BCS-BEC crossover tuned by g/α and $\alpha = 2m k_F^{3D}/\hbar^2$: (a) far BCS, (b) at the ratio $\Delta(0)/\varepsilon_F^{box} \sim 0.65$ and (c) far BEC. The vertical dashed black lines represent the portion of the system that is compared with the PBC case. From [67].*

where

$$\frac{1}{g_{\text{eff}}(z, E_c)} = \frac{1}{U_0} + f(z, E_c) \tag{4.36}$$

with a function $f(z, E_c)$ that explicitly depends on z. The choice of a large cut-off reduces the dependency on spatial coordinates providing a constant factor, g, according to

$$\frac{1}{g_{\text{eff}}(z, E_c)} \sim_{E_c \to \infty} \frac{1}{g} + \mathcal{O}_f(z, E_c) \tag{4.37}$$

where $\mathcal{O}_f \ll g^{-1}$ for large E_c. In the case of an explicit dependency on z_{cm} as well, we follow exactly the same procedure obtaining the constant parameter g used in Eq. (4.24).

4.1.3 Results and comparison

The presence of a finite volume effect, in the case of HW confinement, leads to non-uniform profiles for particle density and order parameter, in the axial direction. This behaviour is, however, different from the case of a quasi-2D system that is realized using harmonic oscillator confinement with a suitable aspect ratio of the harmonic frequencies. When the experimental setup relies on harmonic confinement, the effective chemical potential must be corrected with a local density approximation, which makes it non-uniform all over the axial direction. HW boundaries, instead, preserve locally the uniformity of the particle density, and thus a constant chemical potential, in a finite part, say $l_z < l_z^{\text{hw}}$, in the centre of the axial side span $[-l_z^{\text{hw}}/2, l_z^{\text{hw}}/2]$.
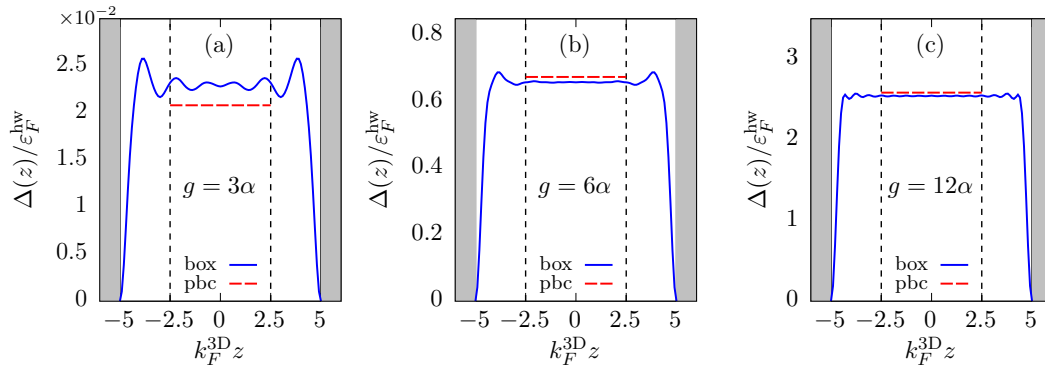
Figure 4.2: *The order parameter $\Delta(z)$, in units of the Fermi energy of the box ε_F^{hw}, as a function of the axial displacement z, for HW boundaries at $k_F^{3D} l_z^{hw} = 10$ (solid blue) and PBC at $k_F^{3D} l_z^{pbc} = 5$ (dashed red) across the BCS-BEC crossover tuned by g/α and $\alpha = 2mk_F^{3D}/\hbar^2$: (a) far BCS, (b) at the ratio $\Delta(0)/\varepsilon_F^{hw} \sim 0.65$ and (c) far BEC. From [67].*

We know that the PBC case, in return, predicts constant density and order parameter all over the axial span $[-l_z^{pbc}/2, l_z^{pbc}/2]$. Hence it is natural to compare the results of HW boundaries for a fixed length l_z^{hw} with the PBC case by setting $l_z^{pbc} = l_z$ (see Fig. 4.1).

In actual computations we introduce a length scale by fixing the number of particles to $N = 2 \times 10^4$, such that if we solve for $l_z^{hw} \sim L$, we obtain

$$\frac{N}{L^2 l_z^{hw}} \sim n_{3D} = \frac{1}{3\pi^2}(k_F^{3D})^3 \tag{4.38}$$

where n_{3D} is the free Fermi gas 3D density and k_F^{3D} the corresponding Fermi momentum. Moreover, we fix the cut-off to $E_c = 35\varepsilon_F^{3D}$ in order to satisfy the requests of the constant g renormalisation procedure (see Sec. 4.1.2). Finally, to ensure the independence of the theory from E_c, we tested our routines for several values of $E_c > 15\varepsilon_F^{3D}$.

In Fig. 4.1 we plot the profiles of the particle density as a function of the axial coordinate, z. The HW range is fixed to $k_F^{3D} l_z^{hw} = 10$, then the bare interaction strength, g, is tuned from the BCS to the BEC regime. In the far BCS regime, we measured the effective $k_F^{3D} l_z^{pbc} = 5$, solved the related BdG problem and compared the profiles. In particular, the role of g in spanning the BCS-BEC crossover can be probed by checking the magnitude of the order parameter in the centre of the axial direction $\Delta(0)$, in terms of the HW case intrinsic energy unit, ε_F^{box}, that is defined as the chemical potential when $g = 0$ (free Fermi gas). Figure 4.1 then combines (a) the BCS regime when $\Delta(0)$ is around $10^{-2}\varepsilon_F^{box}$, (b) the unitarity-like configuration $\Delta(0)/\varepsilon_F^{box} \sim 0.65$ and (c) the BEC regime for large values of g.

Figure 4.3 completes the description of the thermodynamic variables by showing
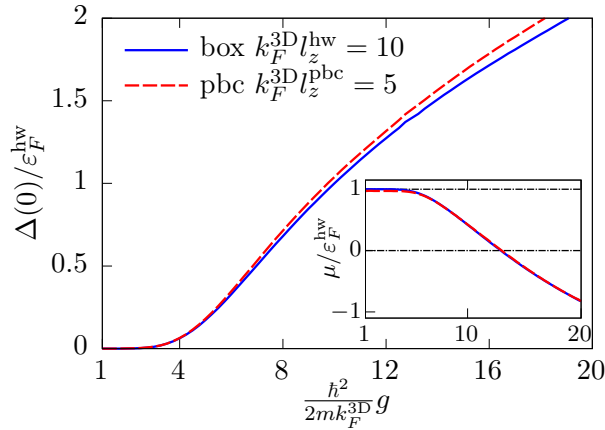
Figure 4.3: *The order parameter at the centre of the box $\Delta(0)$ as a function of the bare interaction strength g, for HW boundaries at $k_F^{3D} l_z^{hw} = 10$ (solid blue) and PBC at $k_F^{3D} l_z^{pbc} = 5$ (dashed red) mapping the full BCS-BEC crossover. The inset shows the the chemical potential, μ, with the same parameters l_z^{hw} and l_z^{pbc} varying g. The dashed-dotted black lines mark the free Fermi gas regime $\mu = \varepsilon_F^{box}$ and transition to a negative μ. From [67]*

the overall behaviour of $\Delta(0)$ and μ (inset) across the BCS-BEC crossover tuned by g. We observe a remarkable matching between the two boundary conditions, provided we select the correct ratio l_z^{hw}/l_z^{pbc}. In particular, the minor discrepancies of density and order parameter are small enough to be well within the experimental measurement errors. In the PBC case, where the renormalisation assumes an analytic form, we observe that the interaction strength is modulated by an inverse hyperbolic sine. This means that small values of g would cover a larger part of the BCS-BEC crossover, namely the whole BCS regime and a large portion around $\mu = 0$. Enlightened by this fact we can also minimize the problem of the increasing mismatch of $\Delta(0)$, in Fig. 4.3, between HW and PBC, for very large values of g.

We finally stress the fact that the described HW configuration has been experimentally investigated in an ultracold Fermi gas setup. The density profile alongside the axial axis can be probed and the definition of an effective l_z^{pbc} is, as well, experimentally viable. Typical values for experimental applications implement a circular in-plane HW confinement, with diameter $D \sim 50 - 200$ μm, and a HW axial confinement, with length $l_z^{hw} \sim 2.9$ μm, obtaining a ratio $l_z^{hw}/D \sim 0.06 - 0.014$. By comparison, if we set L to be of the same magnitude of D, both larger than $1/k_F^{3D}$, HW and PBC are almost identical in the in-plane directions (we treated the in-plane still with PBC), and our ratio takes values around $l_z^{hw}/L = 0.1 - 0.05$. Indeed, the strategy to associate an l_z^{pbc} to an l_z^{hw}, can be easily extended and applied to smaller values of $k_F^{3D} l_z^{hw} \sim 5$ in order to better approach the experimental data.

4.1.4 Order parameter in the HW case and the extension to smaller l_z^{hw}

We address in more details the behaviour of the order parameter in the HW case, which extends the general discussion held in the previous section. We also show that the strategy to define an effective l_z^{pbc} inside l_z^{hw} provides good results also when $k_F^{\mathrm{3D}} l_z^{\mathrm{hw}} < 10$. In particular we approach better the experimental ratio l_z^{hw}/D mentioned in Sec. 4.1.

In Fig. 4.2 we observe, for $k_F^{\mathrm{3D}} l_z^{\mathrm{hw}} = 10$ and $k_F^{\mathrm{3D}} l_z^{\mathrm{pbc}} = 5$ the comparison of the order parameter's profiles across the BCS-BEC crossover, as a function of the axial coordinate $k_F^{\mathrm{3D}} z$. The order parameter is normalized in units of the HW case Fermi energy, $\varepsilon_F^{\mathrm{hw}}$, and we observe again, as in the case of the density profile in Fig. 4.1 a good agreement in (a) far BCS regime, (b) when $\Delta(0)$ approaches values similar to the 3D unitarity, and (c) the far BEC regime. When the system is in BCS regime we notice how the interactions are not strong enough to flatten the profiles of both Fig. 4.1(a) and Fig. 4.2(a). This fact weakens the matching between the HW and PBC case that anyway is strongly recovered when we access a region of the BCS-BEC crossover with larger g. The strategy of an inner l_z^{pbc}, smaller than l_z^{hw}, performs well in order to describe all the relevant quantities, such as the profiles in Fig. 4.1 and Fig. 4.2, the overall order parameter in the centre of the system, in Fig. 4.3 and the chemical potential in the inset of the latter.

In Fig. 4.4 we show the results for the density profile when we reduce the HW length to $k_F^{\mathrm{3D}} l_z^{\mathrm{hw}} = 5$. Again we observed such profile and we matched the HW case with a smaller PBC length. In particular, we choose $k_F^{\mathrm{3D}} l_z^{\mathrm{pbc}} = 2$ and we observe and increasing matching when the interaction strength gets to large values. The same behaviour, like in Fig. 4.2, can be found in the $k_F^{\mathrm{3D}} l_z^{\mathrm{hw}} = 5$, as well as the matching behaviour of the chemical potential, completely equivalent to the case shown in Fig. 4.3. Moreover such matching evaluates the quality of our choice of the matching l_z^{pbc} for a given l_z^{hw}.

Remarks on the HW and PBC interplay

We introduce an energy cut-off, $E_c > 10\varepsilon_F^{\mathrm{3D}}$, large enough such that the renormalisation of g doesn't depend on z and z_{cm}. We are not able to compute the exact dependence of the renormalised g on a_{3D}, l_z and the cut-off, but a large value is enough to control the BCS-BEC crossover by tuning directly g.

In the presence of the box the density of particles is not anymore a constant function, hence the equation $n_{\mathrm{2D}}/l_z = n_{\mathrm{3D}}$ doesn't reproduce the 2D limit of the dimensional crossover. The only alternative is to fix the number of particles N to a large enough number compared with our scales of L and l_z. In Fig. 4.1 we show

how to compare the hard-wall boundaries with the PBC, solving the systems with the following steps:

(i) We fix the number of particles to $N = 2 \times 10^4$ (of the same order as our effective thermodynamic limit for $l_z = L = 100/k_F^{3D}$ in order to have a 3D density of $(k_F^{3D})^3/(3\pi^2))$.

(ii) We first solve the hard-wall case for a fixed $k_F^{3D} l_z$ tuning the dimensionless parameter $\hbar^2 g/(2mk_F^{3D})$, defining the BEC-BCS crossover.

(iii) In the far BCS regime we estimated the region (see Fig. 4.1(a)) in which the density profile is almost constant, defining a $k_F^{3D} l_z^{\text{eff}}$, we then integrate the density on l_z^{eff} and obtain the number of particles in that region, N_{eff}.

(iv) We then solve, with the same range of g, the PBC problem for a system of axial periodicity l_z^{eff} and density $N_{\text{eff}}/(V l_z^{\text{eff}})$ and compare when the densities are similar.

(v) When we have carried out the computations of the PBC case we can compare the order parameter across the BCS-BEC crossover (Fig. 4.2) and at the centre of the box (Fig. 4.3)), and the chemical potential (inset of Fig. 4.3), confirming that we span the whole interacting regime.

The comparison of all the thermodynamic quantities strongly suggests that the BCS side, for very weak interaction, is the most affected by the hard-wall potential, but as soon as we increase the order parameter around the order of $0.2\varepsilon_F^{\text{box}}$ we observe a satisfying similarity between the two systems. The BCS side suffers more differences when we shrink l_z further, but the majority of the crossover is in general not affected. In Figs. 4.4-4.5 we present the case of $k_F^{3D} l_z = 5$ and $k_F^{3D} l_z^{\text{eff}} = 2$, which further shows that the hard wall and PBC systems can be compared.

4.2 Dimensional crossover with PBC

We have seen how it is possible to study a Fermi gas confined in a HW potential, with axial size l_z^{hw}, via a smaller axial length l_z^{pbc} and changing the boundary conditions to the PBC. The thermodynamic quantities and the superfluid order parameter maintain a good agreement in these two cases, but the study of the PBC opens up many different techniques to go beyond the MF theory presented in Sec. 4.1. Hence we are going to address in details the PBC confinement, fixing a new generic axial length $l_z = l_z^{\text{pbc}}$.

We start with a Fermi gas in the in-plane plus PBC axial configuration. The in-plane part will be sent to the thermodynamic limit and the axial kept with PBC
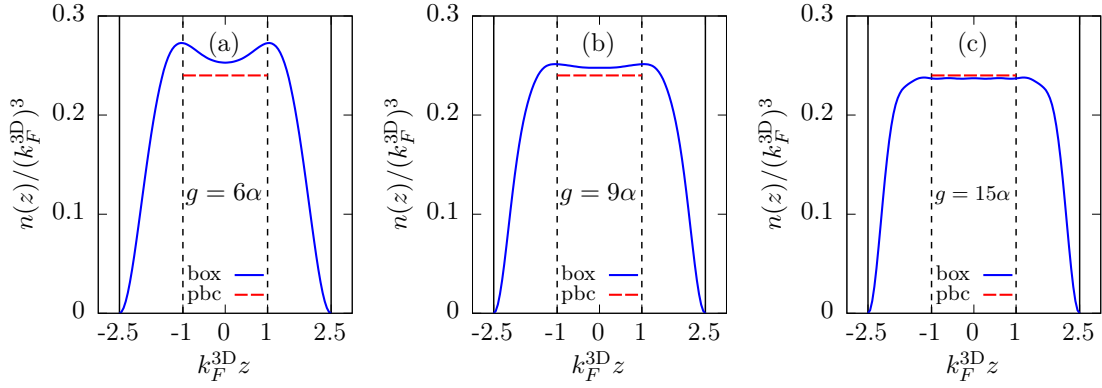
Figure 4.4: *The particle density profile $n(z)$ as a function of the axial displacement z, for hard-wall boundaries at $k_F^{3D}l_z = 5$ (solid blue) and PBC at $k_F^{3D}l_z^{eff} = 2$ (dashed red) across the BCS-BEC crossover tuned by g/α and $\alpha = 2mk_F^{3D}/\hbar^2$: (a) far BCS, (b) at the ratio $\Delta(0)/\varepsilon_F^{(box)} \approx 1.5$ and (c) far BEC.*

Figure 4.5: *The order parameter $\Delta(z)$, in units of the Fermi energy of the box $\varepsilon_F^{(box)}$, as a function of the axial displacement z, for hard-wall boundaries at $k_F^{3D}l_z = 5$ (solid blue) and PBC at $k_F^{3D}l_z^{eff} = 2$ (dashed red) across the BCS-BEC crossover tuned by g/α and $\alpha = 2mk_F^{3D}/\hbar^2$: (a) far BCS, (b) at the ratio $\Delta(0)/\varepsilon_F^{(box)} \approx 1.5$ and (c) far BEC.*
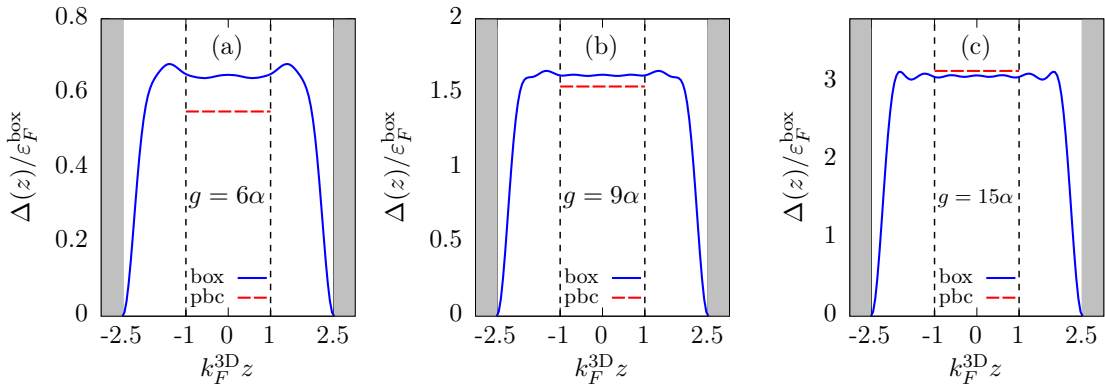
length l_z. In momentum space we use a combined coordinates notation, $(\mathbf{k}, k_z)$, merging the in-plane directions in $\mathbf{k}$ and, aside, the axial dependency with k_z. The plane waves of the axial direction are discretised and they have a momentum,

$$k_z = \frac{2\pi n_z}{l_z} \tag{4.39}$$

where n_z is an integer number. We address here the choices of the tuning parameter for the dimensional crossover and the BCS-BEC crossover.

4.2.1 Dimensional crossover parameter η

The non-interacting case, at zero temperature, can be addressed comparing the particle densities in the 3D, quasi-2D and 2D regimes. The PBC choice doesn't influence the 3D particle density, n_{3D}, and thus we set,

$$n = n_{3D} = \frac{n_{2D}}{l_z} \tag{4.40}$$

where n and n_{2D} respectively represent the particle densities in the quasi-2D and 2D cases. In the free Fermi gas model, these densities have a direct relation with the Fermi momenta, k_F^{3D} and k_F^{2D},

$$k_F^{3D} = (3\pi n_{3D})^{1/3} \quad \text{and} \quad k_F^{2D} = (2\pi n_{2D})^{1/2}. \tag{4.41}$$

The quasi-2D density is obtained by the number equation, $N = -\partial \Omega_{\text{free}}/\partial \mu$, on the free thermodynamic potential at zero temperature, Ω_{free},

$$\Omega_{\text{free}} = 2 \sum_{\mathbf{k}, k_z} \left(\frac{\hbar^2 (\mathbf{k}^2 + k_z^2)}{2m} - \mu \right) \Theta \left(\frac{\hbar^2 (\mathbf{k}^2 + k_z^2)}{2m} - \mu \right) \tag{4.42}$$

where the chemical potential, μ, is by definition the quasi-2D Fermi energy, $\varepsilon_F = \hbar^2 k_F^2/(2m)$ and k_F is the quasi-2D Fermi momentum for a fixed l_z. We obtain a non trivial dependence of n on k_F,

$$n = \frac{1}{2\pi l_z} \sum_{n_z = -n_{\text{max}}}^{n_{\text{max}}} \left[k_F^2 - \left(\frac{2\pi n_z}{l_z} \right)^2 \right], \tag{4.43}$$

where n_{max} is the largest integer smaller than $k_F l_z/(2\pi)$. We solve Eq. (4.40) and we obtain,

$$\frac{k_F^{2D}}{k_F^{3D}} = \sqrt{\frac{2k_F^{3D} l_z}{3\pi}}, \tag{4.44}$$

$$k_F = k_F^{2D} \quad \text{if} \quad k_F^{3D} l_z \leq \pi 6^{1/3}. \tag{4.45}$$
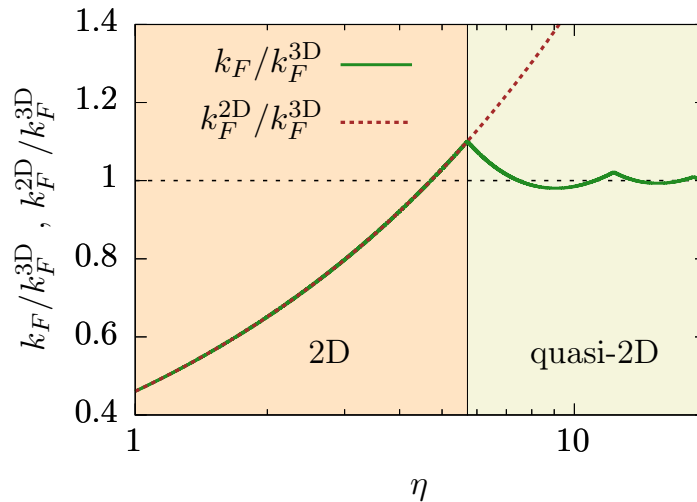
Figure 4.6: *The quasi-2D and 2D Fermi momenta, k_F and k_F^{2D}, with respect to the 3D Fermi momentum, k_F^{3D}, as the dimensional parameter η (in logarithmic scale) varies from the 3D to the 2D regime. The vertical line at $\eta = \pi 6^{1/3}$ denotes the transition between the quasi-2D and the 2D regime while the perfect 3D is obtained in the limit $\eta \to \infty$ only.*

Higher values of $k_F^{3D} l_z$ lead to more a complicated dependence of the ratio $k_F/(k_F^{3D})$ on the parameter $k_F^{3D} l_z$. Beside, Eq. (4.45) suggests the primary role of the parameter $\eta \equiv k_F^{3D} l_z$ as a good tuning quantity to describe the crossover. Figure 4.6 shows the sharp transition at $\eta = \pi 6^{1/3}$ from the quasi-2D and the 2D regime that it is due to the fact that the PBC forces the second lowest energetic eigenfunction of the box to be placed outside the first Brillouin zone. When $\eta < \pi 6^{1/3}$, the system is forced to be composed by copies of the same 2D system with a unique state available in the z direction. Restoring the 3D thermodynamic limit, for $\eta \to \infty$, we obtain that the 2D and quasi-2D Fermi energies are not anymore comparable and the quasi-2D Fermi momentum approaches the 3D one.

4.2.2 Exact renormalisation of the PBC case and BCS-BEC crossover parameter l_z/a_{3D}

We recall the Hamiltonian that describes the Fermi gas from Eq. (4.1) and, since we are treating the PBC case, we set $V_{\text{ext}} = 0$. The contact potential of Eq. (4.1) is given by the distribution,

$$U((\mathbf{x}, z) - (\mathbf{x}', z')) = -U_0 \delta(\mathbf{x} - \mathbf{x}')\delta(z - z'), \qquad (4.46)$$

which is essentially 3D and hence it doesn't require dilation correction. Moreover the renormalisation of U shows some resemblance with the 2D contact potential renormalisation supporting always a bound state with binding energy $-B_0$ and

$B_0 > 0$. Starting from the Schrödinger equation over the space $\mathbb{R}^2 \times [-l_z/2, l_z/2]$,

$$\left[-\frac{\hbar^2}{m} \left(\nabla_{\mathbf{x}}^2 + \partial_z^2 \right) - U_0 \delta(\mathbf{x}) \delta(z) \right] \psi(\mathbf{x}, z) = -B_0 \psi(\mathbf{x}, z), \qquad (4.47)$$

we obtain the regularization

$$\frac{1}{U_0} = \frac{1}{(2\pi)^2 l_z} \sum_{k_z} \int_{\mathbb{R}^2} \frac{d^2 k}{\hbar^2 (\mathbf{k}^2 + k_z^2)/m + B_0}. \qquad (4.48)$$

which, as mentioned before, is convergent for small $|(\mathbf{k}, k_z)|$ values but needs to be cured by a cut-off at large momenta. In order to give meaning to the quasi-2D binding energy $-B_0$, we require that when the 3D thermodynamic limit is restored, for $l_z \to \infty$, that we obtain $B_0 = \varepsilon_B^{3D}$, where the 3D binding energy, ε_B^{3D}, is related to the 3D s-wave scattering length, a_{3D}, by

$$\varepsilon_B^{3D} = \begin{cases} 0 & \text{if} \quad a_{3D} < 0 \\ \hbar^2/(ma_{3D}^2) & \text{if} \quad a_{3D} > 0 \end{cases} \qquad (4.49)$$

The study of such relation is carried out by comparing the two-body T-matrix in the quasi-2D and 3D case in the 3D thermodynamic limit [70, 108],

$$\lim_{l_z \to \infty} \left(\int_{\mathbb{R}^3} \frac{d\mathbf{k} dk_z}{\hbar^2 (\mathbf{k}^2 + k_z^2)/m + \varepsilon_B^{3D}} - \frac{2\pi}{l_z} \sum_{n_z = -\infty}^{\infty} \int_{\mathbb{R}^2} \frac{d\mathbf{k}}{\hbar^2 (\mathbf{k}^2 + k_z^2)/m + B_0} \right) = 0. \qquad (4.50)$$

The binding energy B_0 can be written as a function of a_{3D} with a clear dependency on l_z giving,

$$B_0 = \frac{4\hbar^2}{m l_z^2} \operatorname{arcsinh}^2 \left(\frac{e^{l_z/(2a_{3D})}}{2} \right). \qquad (4.51)$$

It appears from Eq. (4.51) that the contact potential in the quasi-2D regime supports, for any finite positive value of l_z and any finite non-zero value of a_{3D}, a bound state with binding energy $-B_0$. In Fig. 4.7 we plot the behaviour of B_0 over a_{3D} and we observe that Eq. (4.51) becomes dependent on the ratio l_z/a_{3D} only. While $1/(k_F^{3D} a_{3D})$ is the tuning parameter of the BCS-BEC crossover in 3D, l_z/a_{3D}, featuring a length scale change towards a more suitable quasi-2D parameter, is the natural candidate for the role of tuning parameter of the BCS-BEC crossover. This elegant change of length scale turns out to be even more interesting when we study the limit for the 2D regime, attempting the $\eta \to 0$ limit. The similarities between the 2D and quasi-2D T-matrices suggest to define the 2D binding energy $\varepsilon_B^{2D} = \hbar^2/(ma_{2D}^2)$ through the limit,

$$\lim_{l_z \to \infty} \left(\int_{\mathbb{R}^2} \frac{d\mathbf{k}}{\hbar^2 \mathbf{k}^2/m + \varepsilon_B^{2D}} - \sum_{n_z = -\infty}^{\infty} \int_{\mathbb{R}^2} \frac{d\mathbf{k}}{\hbar^2 (\mathbf{k}^2 + k_z^2)/m + B_0} \right) = 0. \qquad (4.52)$$
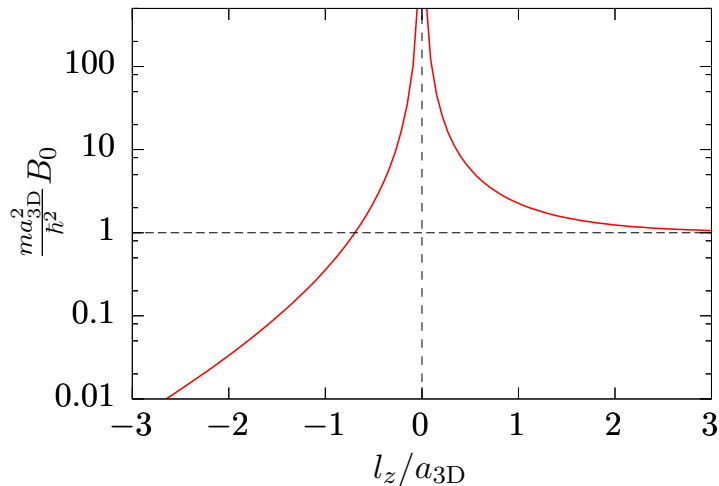
Figure 4.7: *The quasi-2D binding energy (in logarithmic scale), B_0, rescaled by the 3D scattering length, a_{3D}, as a function of the quasi-2D BCS-BEC crossover tuning parameter, l_z/a_{3D}. When $a_{3D} > 0$, the graph is equivalent to the ratio B_0/ε_F^{3D} and approaches 1 for large l_z values.*

Curing the divergence with a cut-off renormalisation on both integrals, it is possible to show that B_0 must verify,

$$\lim_{l_z \to 0} B_0 = \varepsilon_B^{2D} \tag{4.53}$$

This further remark suggests to introduce a quasi-2D s-wave scattering length, a, that is related with the binding energy through,

$$B_0 = \frac{\hbar^2}{ma^2} \tag{4.54}$$

and converges to the exact 2D scattering length when η is sent to zero. This choice turns out again to be very useful to describe the BCS-BEC crossover when η is close to zero. The presence of a proper quasi-2D scattering length allows us to define the parameter $\ln(k_F a)$ that converges, for $\eta \to 0$, to the BCS-BEC crossover tuning parameter in 2D, $\ln(k_F^{2D} a_{2D})$, according to Eqs. (4.45) and (4.53).

4.3 Quasi-2D BCS-BEC crossover: Theory

4.3.1 Mean field theory

Once we obtained the combination of parameters that spans both the dimensional and BCS-BEC crossover, we can address the study of the quantities that characterize the strongly interacting regime. For a fixed value of l_z, we consider the Hamiltonian density in Eq. (4.1) and we compute the thermodynamic potential at the mean field

level at zero temperature. We follow a similar scheme to Chap. 2, by introducing the Hubbard-Stratonovich transformation which introduces the auxiliary bosonic quantum field $\hat{\Delta}(\mathbf{x}, z) = -U_0 \psi_\downarrow(\mathbf{x}, z)\psi_\uparrow(\mathbf{x}, z)$ that is approximated, at the mean field level by its average on the ground state $\Delta = \langle \hat{\Delta} \rangle$. The themodynamic potential is now composed by its mean field contribution, Ω_{MF}, that is given by,

$$\frac{\Omega_{\text{MF}}}{V} = \frac{\Delta^2}{U_0} + \frac{1}{V}\sum_{\mathbf{k},k_z}(\xi_{\mathbf{k},k_z} - E_{\mathbf{k},k_z}) \tag{4.55}$$

where V is the volume of the box. We also introduced a modified version of the notation in Eq. (2.59) due to the quasi-2D case, where for a generic momentum k we have $\varepsilon_k = \hbar^2 k^2/(2m)$ and we subsequently define $\xi_{\mathbf{k},k_z} = \varepsilon_\mathbf{k} + \varepsilon_{k_z} - \mu$ and $E_{\mathbf{k},k_z} = \sqrt{\xi_{\mathbf{k},k_z}^2 + \Delta^2}$.

The order parameter, Δ, in the ground state configuration has to be a point of minimum of the thermodynamic potential by solving the gap equation,

$$0 = \frac{\partial \Omega_{\text{MF}}}{\partial \Delta} = \Delta \sum_{\mathbf{k},k_z} \left(\frac{1}{\varepsilon_\mathbf{k} + \varepsilon_{k_z} + B_0/2} - \frac{1}{E_{\mathbf{k},k_z}} \right). \tag{4.56}$$

Then it is possible to compute μ through the number equation, $n = -V^{-1}\partial_\mu\Omega_{\text{MF}}$, fixing the density n to the real density of Eq. (4.43).

A very useful simplification occurs on Δ and Ω_{MF} when we send the two transverse directions to the thermodynamic limit. It is possible to shift the chemical potential to $\mu_z = \mu - \varepsilon_{k_z}$ and analytically solve the 2D integration, as it is well know that the 2D MF is analytically solvable. The gap equation then becomes,

$$0 = \Delta \sum_{k_z} \ln\left(\frac{-\mu_z + \sqrt{\mu_z^2 + \Delta^2}}{2\varepsilon_{k_z} + B_0} \right) \tag{4.57}$$

The gap equation has a non trivial solution when $\Delta = 0$ and the chemical potential assumes the critical value,

$$\mu_c = -\frac{B_0}{2} \tag{4.58}$$

that, as in the 2D case, denotes the transition between the particle vacuum and a finite particle density. Moreover, the MF part of the thermodynamic potential can be simplified further obtaining,

$$\frac{\Omega_{\text{MF}}}{V} = \frac{m}{2\pi\hbar^2 l_z} \sum_{k_z} \left[\frac{\Delta^2}{2} \ln\left(\frac{-\mu_z + \sqrt{\mu_z^2 + \Delta^2}}{2\varepsilon_{k_z} + B_0} \right) - \frac{1}{4}\left(\mu_z + \sqrt{\mu_z^2 + \Delta^2} \right)^2 \right]. \tag{4.59}$$

In Fig. 4.8 we plot the behaviour of the chemical potential, μ, shifted by the binding energy B_0. The large η cases, in panel (a), show, as expected, that it is possible to recover the actual 3D thermodynamic limit by increasing the thickness
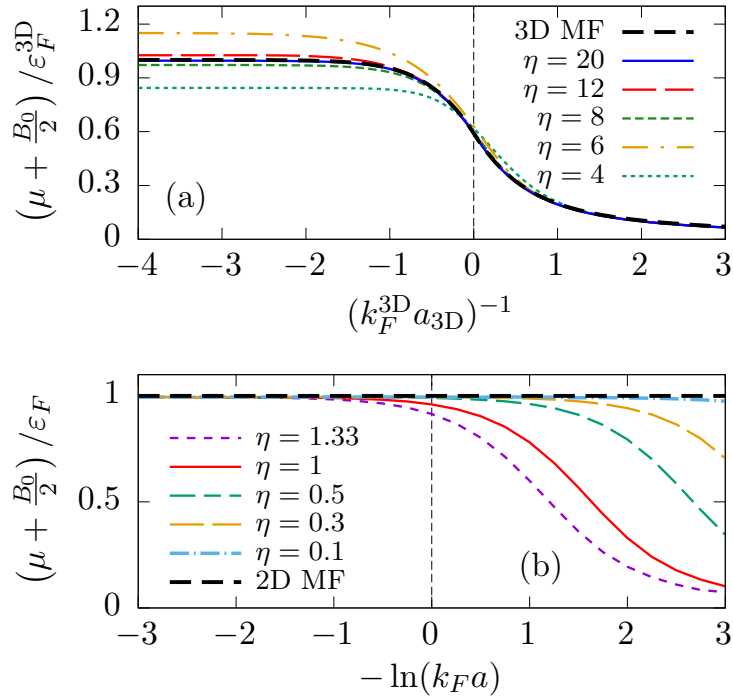
Figure 4.8: *The chemical potential μ, shifted by the binding energy $B_0/2$ across the BCS-BEC crossover for several values of η. (a) For large η values the crossover is tuned by the 3D parameter, $1/(k_F^{3D}a_{3D})$, and the energy is in units of the 3D Fermi energy. (b) For small η the crossover is tuned by the function $\ln(k_F a)$ that recovers the 2D tuning parameter for $η \to 0$, while the energy is in units of the quasi-2D Fermi energy that is equal to the 2D Fermi energy when $η \leq π6^{1/3}$.*

of the axial direction. However, in the BCS limit, since we expect the chemical potential to approach the Fermi energy, each value of η sends μ to the respective Fermi energy, ε_F, which according to Fig. (4.6) is not exactly the 3D Fermi energy. Beside, we observe an overall agreement with the 3D case, for each $\eta \geq 8$, while decreasing η we keep a 3D behaviour in the BEC regime only. In panel (b) we observe how, for $\eta < 2$, in the proper BCS-BEC crossover tuning parameter $\ln(k_F a)$, that the chemical potential goes towards the analytic solution of the MF in 2D,

$$n_{2D} = \frac{1}{2\pi} \left(\mu + \frac{B_0}{2} \right) \tag{4.60}$$

It is then impossible, as in the 2D case, to recover the BCS-BEC crossover behaviour of μ when we approach $\eta \to 0$. The fluctuations there have a dominant contribution to the particle density.

4.3.2 Gaussian pair fluctuations

We then consider the fluctuations correction to the MF at zero temperature, using a scheme that has been found accurate in both 3D and 2D regimes. The auxiliary bosonic field of the Hubbard-Stratonovich transformation is approximated to the next leading order, $\hat{\Delta}(\mathbf{x}, z) = \Delta(\mathbf{x}, z) + \chi(\mathbf{x}, z)$, where χ is the fluctuations field around the MF order parameter. The contribution to the thermodynamic potential, Ω_{GPF}, is given, at finite temperature $k_B T = \beta^{-1}$, by

$$\Omega_{\mathrm{GPF}} = -\frac{1}{\beta} \ln \int \mathcal{D}\chi^* \mathcal{D}\chi \exp\left[\mathscr{S}_{\mathrm{GPF}}(\chi^*, \chi) \right] \tag{4.61}$$

where k_B is the Boltzmann constant and the GPF action, $\mathscr{S}_{\mathrm{GPF}}$, can be written as

$$\mathscr{S}_{\mathrm{GPF}} = \frac{\beta V}{2} \sum_Q \left(\chi^*(Q) \quad \chi(-Q) \right) \mathbb{M}(Q) \begin{pmatrix} \chi(Q) \\ \chi^*(-Q) \end{pmatrix} \tag{4.62}$$

where we introduced the multi-index notation $Q \equiv (\mathbf{q}, q_z, \mathrm{i}q_\nu)$ featuring the Fourier spatial momenta, $(\mathbf{q}, q_z)$, of ϕ and $q_\nu = 2\pi\nu/\beta$, for $\nu \in \mathbb{Z}$, the bosonic Matsubara frequencies. Moreover, the matrix $\mathbb{M}$, can be written by components, again by slightly modifying Eqs. (2.56) and (2.57) into

$$\mathbb{M}_{11} = \frac{1}{U_0} + \frac{1}{V} \sum_{\mathbf{k}, k_z} \left(\frac{u_+^2 u_-^2}{\mathrm{i}q_\nu - E_+ - E_-} - \frac{v_+^2 v_-^2}{\mathrm{i}q_\nu + E_+ + E_-} \right),$$

$$\mathbb{M}_{12} = \frac{1}{V} \sum_{\mathbf{k}, k_z} \left(-\frac{u_+ u_- v_+ v_-}{\mathrm{i}q_\nu - E_+ - E_-} + \frac{u_+ u_- v_+ v_-}{\mathrm{i}q_\nu + E_+ + E_-} \right),$$

$$\mathbb{M}_{22}(Q) = \mathbb{M}_{11}(-Q), \qquad \mathbb{M}_{21}(Q) = \mathbb{M}_{12}(Q). \tag{4.63}$$

with $E_\pm = \sqrt{\xi_\pm^2 + \Delta^2}$ and $\xi_\pm \equiv \xi_{\mathbf{k}\pm\frac{\mathbf{q}}{2},k_z\pm\frac{q_z}{2}}$. According to the discussion in Chap. 2, the GPF correction needs regularization for large values of the Matsubara frequencies, but at zero temperature, for $\beta \to \infty$, we can introduce [75] the auxiliary convergent part of $\mathbb{M}_{11}$,

$$\mathbb{M}_{11}^C(Q) = \frac{1}{U_0} + \sum_{\mathbf{k},k_z} \frac{u_+^2 u_-^2}{\mathrm{i}\,q_\nu - E_+ - E_-}, \qquad (4.64)$$

and Wick rotate the Matsubara frequencies, $\mathrm{i}\,q_\nu \mapsto \omega$, swapping the sum on $\mathrm{i}\,q_\nu$ with an integration on ω, obtaining the convergent form,

$$\Omega_{\mathrm{GPF}} = \sum_{\mathbf{q},q_z} \int_0^\infty \frac{d\omega}{2\pi} \ln \Gamma^{-1}(\mathbf{q}, q_z, \omega) \qquad (4.65)$$

where

$$\Gamma^{-1}(Q) = \frac{\mathbb{M}_{11}(Q)\mathbb{M}_{11}(-Q) - \mathbb{M}_{12}(Q)^2}{\mathbb{M}_{11}^C(Q)\mathbb{M}_{11}^C(-Q)} \qquad (4.66)$$

We modify the thermodynamic potential in order to include fluctuations, $\Omega = \Omega_{\mathrm{MF}} + \Omega_{\mathrm{GPF}}$, and we impose that the order parameter is computed at the MF level only. This feature guarantees the Goldstone's theorem. Indeed, if Δ is given by Eq. (4.57) only, we verify that for $Q = 0$, the determinant $\mathbb{M}_{11}^2(0) - \mathbb{M}_{12}^2(0) = 0$. The lowest-lying collective mode has to be gapless and display a linear behaviour of the dispersion relation when $|(\mathbf{q}, q_z)|$ is small, where the dispersion of the Goldstone mode is given by the roots $\omega_0(\mathbf{q}, q_z)$ of the determinant,

$$\det \mathbb{M} = \mathbb{M}_{11}(Q)\mathbb{M}_{11}(-Q) - \mathbb{M}_{12}^2(Q) = 0. \qquad (4.67)$$

Finally, the chemical potential, at the GPF level, is found by solving the modified number equation,

$$n = -\frac{1}{V}\frac{\partial\Omega}{\partial\mu}. \qquad (4.68)$$

It is now possible to span the PBC periodicity η and the BCS-BEC crossover tuning parameter, l_z/a_{3D} in order to obtain μ and the order parameter, Δ.

In Fig. 4.9 we plot the results for the chemical potential, μ, including the GPF contribution to the thermodynamic potential. We observe in panel (a) that, for $\eta \geq 8$, we recover, once again, the results in the 3D thermodynamic limit across the entire BCS-BEC crossover. The quasi-2D regime manifests itself when $\eta < 8$ when the BCS regime deviates from the 3D case and the BEC regime is almost recovered. In panel (b) we perform a change in the tuning parameter and we rescale the energy in terms of the quasi-2D Fermi energy. The characteristic decreasing slope of the BCS-BEC crossover is recovered when $\eta \gtrsim 1$ but we observe a drift of the crossover towards the BCS side. Then, in panel (c), we overtake the drift
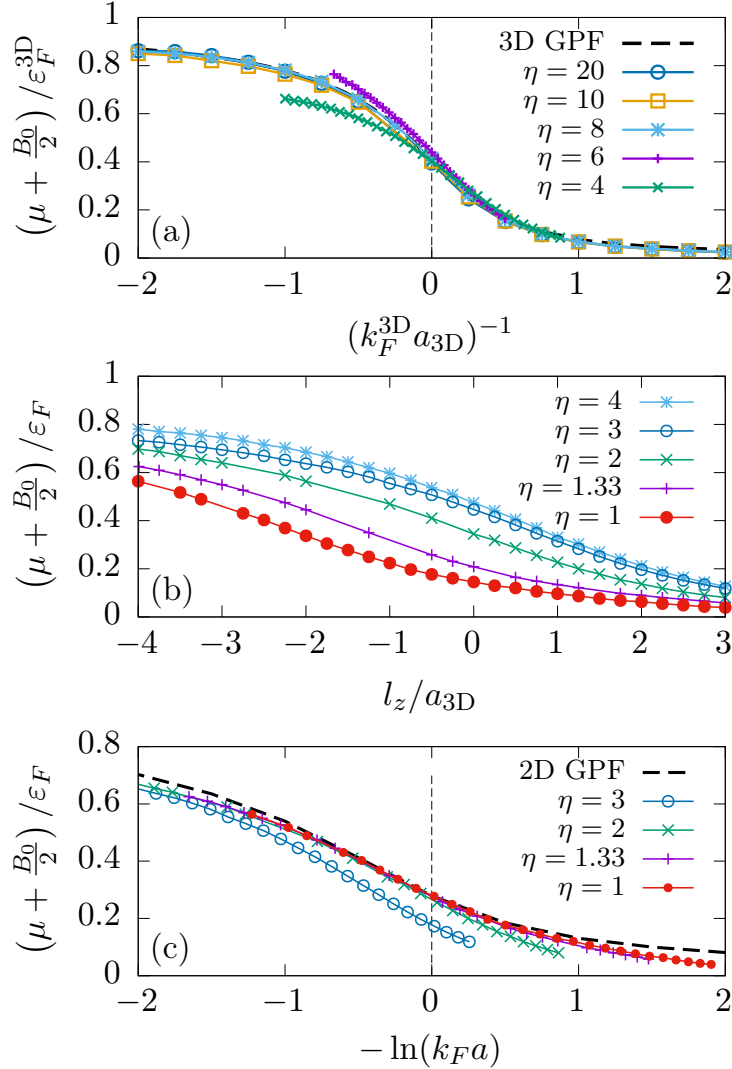
Figure 4.9: *The chemical potential μ, shifted by the binding energy $B_0/2$ across the BCS-BEC crossover for several values of η. (a) For large η values the crossover is tuned by the 3D parameter, $1/(k_F^{3D}a_{3D})$, and the energy is in units of the 3D Fermi energy. (b) For $1 \leq \eta \leq 4$, the crossover is tuned by the quasi-2D parameter, l_z/a_{3D}, and energy is in quasi-2D Fermi energy units. (c) For small η the crossover is tuned by the function $\ln(k_F a)$ that recovers the 2D tuning parameter for $\eta \to 0$, while the energy is in units of the quasi-2D Fermi energy that is equal to the 2D Fermi energy when $\eta \leq \pi 6^{1/3}$. From [67].*

Figure 4.10: *The order parameter, Δ, in units of the quasi-2D Fermi energy, ε_F, as a function of the quasi-2D tuning parameter l_z/a_{3D}, for several values of $\eta < 8$.*

of panel (b) imposing the 2D BCS-BEC crossover tuning parameter $\ln(k_F a)$ that exactly matches the 2D case when $\eta \to 0$. The data for $\eta > 3$ tend 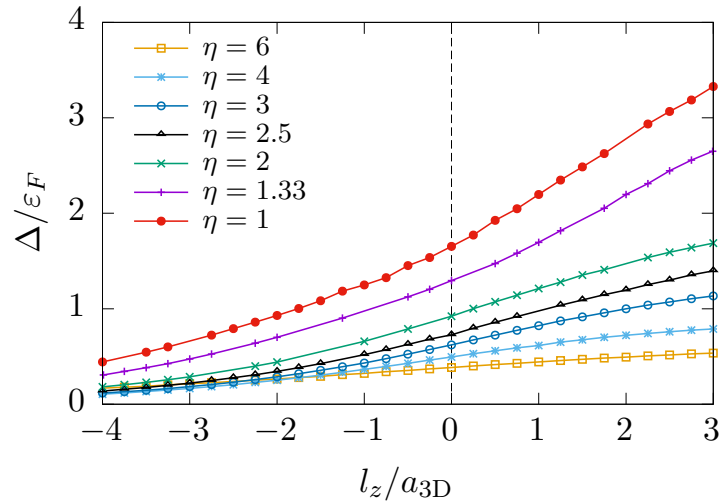to approach the BCS-BEC crossover in 2D. At first glance, we remark the existence of at least three regimes that require different tuning parameters in order to display the full BCS-BEC crossover. In Fig. 4.10, we plot the order parameter, Δ, as a function of the quasi-2D BCS-BEC crossover tuning parameter. We observe that, on the BCS side of the crossover, the order parameter maintains a similar behaviour when $2 \leq \eta \leq 6$, but below $\eta = 2$ there is a sudden increase of the magnitude of Δ. We will see that this is another effect that can be corrected by imposing the change of tuning parameter to $\ln(k_F a)$.

4.4 Quasi-2D BCS-BEC crossover: Experimental considerations

4.4.1 Collective modes

In order to provide a quantitative criterion to experimentally distinguish between different dimensional regimes, we extend our analysis including the study of collective modes. In particular, we will see that the study of the superfluid critical velocity provides a straightforward parameter to separate the values of η when the system is 3D, quasi-2D or 2D. The function $\Gamma(\mathbf{q}, q_z, \omega)$ in Eq. (4.66) is the vertex function of the Goldstone mode and provides [77, 109] the dispersion relations for the superfluid collective modes. The presence of a gap in the excitation spectrum
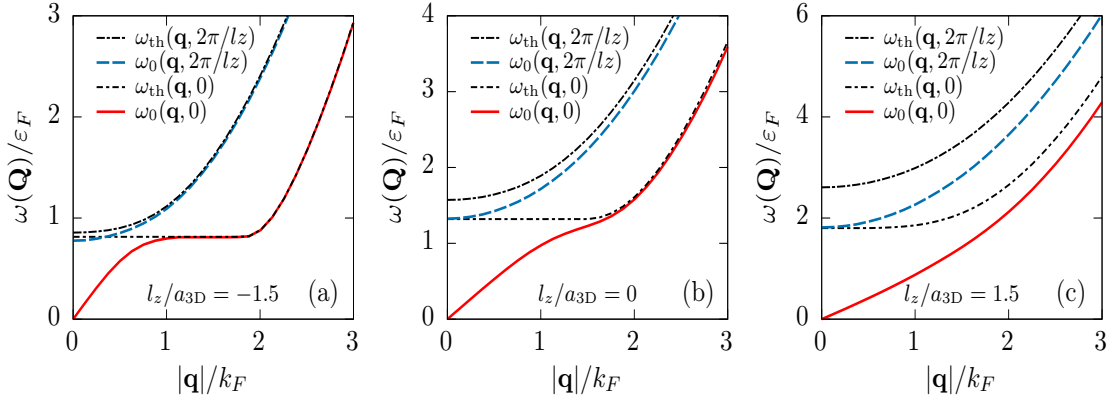
Figure 4.11: *The collective mode dispersion relations $\omega_0(\mathbf{Q})$ as a function of the excitation momentum $\mathbf{q}$, for $\eta = 4$. Each collective mode is compared with the threshold $\omega_{th}(\mathbf{Q})$ when the excitation is in-plane only, $q_z = 0$ and adding the lowest axial component to the excitation, $q_z = 2\pi/l_z$. The panel plots the (a) far BCS regime, for $l_z/a_{3D} = -1.5$, (b) at 3D unitarity, for $l_z/a_{3D} = 0$, and (c) far BEC regime, for $l_z/a_{3D} = 1.5$.*

entails that below a certain threshold an excitation has to be collective because the energy provided is not enough to break a pair of coupled fermions. The poles of Γ are responsible for this behaviour and Eq. (4.67) admits simple zeros only if $\omega < E_+ + E_-$ for arbitrary $(\mathbf{k} \pm \mathbf{q}/2, k_z \pm q_z/2)$ and a given chemical potential, μ, and order parameter, Δ. Thus, we address the study of the minimization problem

$$\omega_{th}(\mathbf{q}, q_z) = \min_{\mathbf{k}, k_z}\{E_+ + E_-\} \tag{4.69}$$

for given $(\mathbf{q}, q_z)$. The function $E_+ + E_-$ can be embedded in $\mathbb{R}^3$, and it is possible to perform a coordinates rotation in such a way that we obtain a solution that is an analogue of the 3D case [109]. We introduce the momentum $\mathbf{Q}$ with magnitude $|\mathbf{Q}| = \sqrt{\mathbf{q}^2 + q_z^2/4}$ and the threshold is given by,

$$\omega_{th}(\mathbf{Q}) = \begin{cases} 2\Delta & \text{if } \mu > 0 \text{ and } \hbar^2\mathbf{Q}^2 \leq 8m\mu \\ 2\sqrt{\mu_\mathbf{Q}^2 + \Delta^2} & \text{otherwise} \end{cases} \tag{4.70}$$

with $\mu_\mathbf{Q} = \mu - \hbar^2\mathbf{Q}^2/(8m)$. We can focus on a specific regime of the dimensional crossover, η, at fixed interaction strength, by choosing l_z/a_{3D} and plug in Eq. (4.70) the results for μ and Δ obtained by the GPF calculations in Sec. 4.3.2. Next, we compute the collective mode threshold and the simple poles of the vertex function Γ considering different combinations of in-plane, $\mathbf{q}$, and axial, q_z, excitation momenta.

In Fig. 4.11 we display the behaviour of the collective modes $\omega_0(\mathbf{q}, q_z)$, below the threshold $\omega_{th}(\mathbf{q}, q_z)$, for different combinations of in-plane $\mathbf{q}$ excitation momentum or a combined in-plane and axial, $(\mathbf{q}, q_z)$, momentum. The dimensional crossover has been fixed to $\eta = 4$ in order to represent the broadest collection of the collective

modes properties in every regime. In particular when $\eta \to 0$, we expect l_z to be smaller and the gap between axial momenta to spread. Hence the axial contribution disappears along with the decrease of η. In the opposite case, when $\eta \to \infty$, many axial contributions merge together closer to the lowest axial momentum contribution, for $q_z = 0$, and reconstruct the 3D case where the rotational symmetry of Eq. (4.69) is restored. In the 3D case thus any axial excitation can be displayed through the in-plane excitation dispersion. We observe that across the BCS-BEC crossover, tuned by l_z/a_{3D}, the relation between the collective mode $\omega_0(\mathbf{q}, 0)$ and the related threshold $\omega_{\text{th}}(\mathbf{q}, 0)$ appears to be exactly as in the 3D case [109]. In panel (a), the BCS regime forces the collective mode to join the threshold line at low momenta, while moving towards the BEC regime we observe a gradual change in the shape of ω_0 that clearly detaches from the threshold, in panel (b), and becomes increasing monotonic, in panel (c). The addition of an axial component to the excitations doesn't change this overall trend, maintaining the increasing monotonic behaviour and detaching from its threshold line.

The study of the lowest energy collective mode is pivotal to understand the regime of superfluidity and how the interactions change the response of the system upon an external momentum injection. In the BCS regime of the crossover, since the superfluid is composed by weakly-bounded Cooper pairs, we expect the pair-breaking energy to be the primary source of destruction of superfluidity, while in the BEC regime the pairs are so tightly bounded that the phonon mode, at low energy, is the first responsible to destabilize the system.

4.4.2 Dimensional crossover diagram

This consideration leads to the study of the superfluid critical velocity. The pair-breaking velocity can be analytically computed once the chemical potential is known, from Landau criterion,

$$v_{\text{pb}} = \min_k \left\{ \frac{E_k}{k} \right\} = \left[\left(\sqrt{\Delta^2 + \mu^2} - \mu \right) / m \right]^{1/2} \qquad (4.71)$$

At the same time the phonon excitation provides the first speed of sound, c_s, that is given by the linear behaviour of $\omega_0(\mathbf{q}, 0)$ when $|\mathbf{q}| \to 0$,

$$c_s = \lim_{|\mathbf{q}| \to 0} \frac{\omega_0(\mathbf{q}, 0)}{|\mathbf{q}|} \qquad (4.72)$$

The Landau criterion also states that the superfluid critical velocity has to be, at any interaction strength, the minimum between the pair-breaking velocity and the speed of sound, obtaining

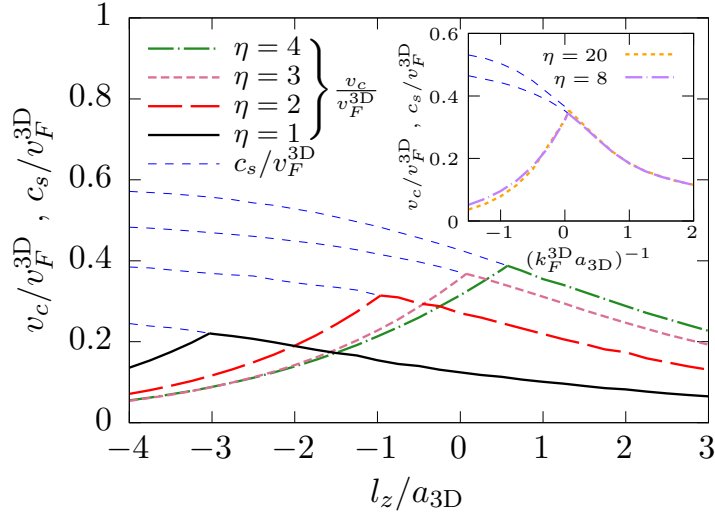$$v_c = \min\{v_{\text{pb}}, c_s\} \qquad (4.73)$$

Figure 4.12: *The critical velocity, v_c, in units of the 3D Fermi velocity, v_F^{3D}, across the BCS-BEC crossover for several values of the dimensional crossover parameter, η. For small η the interactions are tuned by the quasi-2D parameter, l_z/a_{3D}, while, in the inset, for large η, the 3D parameter $1/(k_F^{3D}a_{3D})$ is used. At the right hand side of the critical velocity maximum the Landau criterion ensures that the speed of sound, c_s, is the critical velocity. From [67].*

In the BEC regime of Fig. 4.11(c), the monotonicity of ω_0 leads to the equivalence between the critical velocity and the speed of sound.

In Fig. 4.12 we show the behaviour of the critical velocity for several values of η, spanning from the 3D (in the inset) towards the 2D regime. In the 3D case we notice that, in the 3D scale $1/(k_F^{3D}a_{3D})$, the position of the peak doesn't vary while minor differences in the pair-breaking velocity in the far BCS regime are present due to the difference of the Fermi energy for $\eta = 8$ and $\eta = 20$. The magnitude of the maximum critical velocity decreases, in units of v_F^{3D}, when we reduce η towards 1. This is expected because v_F^{3D} fails to be a good scale in 2D. Moreover, we observe that the maximum critical velocity drifts towards the quasi-2D BCS regime $l_z/a_{3D} < 0$ for small values of η. The maximum of the critical velocity is indeed a good mark of the type of dimensional regime η tunes. Fixing η, we can denote with $(l_z/a_{3D})_{v_c^{\max}}$ the position at which the maximum $v_c^{\max}$ lies and map out how it evolves with η.

In Fig. 4.13 we draw the BCS-BEC crossover evolution through the dimensional tuning of η. The line $(l_z/a_{3D})_{v_c^{\max}}$ separates the BCS regime, when l_z/a_{3D} is below it, from the BEC regime denoted by l_z/a_{3D} values above the line. The MF theory (bold dashed) gives a qualitative understanding of the dimensional crossover that is enhanced by the GPF approach. We observe that the 2D regime is reached when the drift of the maximum critical velocity becomes logarithmic, justifying the change of tuning parameter to $\ln(k_F a)$ in the inset. The 3D regime must be linear in η and the
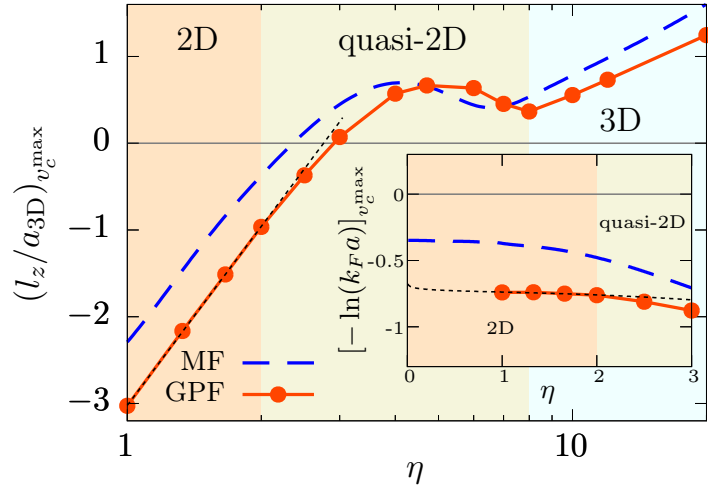
Figure 4.13: *The dimensional crossover diagram tuned by the dimensional parameter, η, in logarithmic scale, and by the position on the BCS-BEC crossover, $(l_z/a_{3D})_{v_c^{\max}}$ of the peak of the critical velocity, $v_c^{\max}$. The asymptotic behaviour of $(l_z/a_{3D})_{v_c^{\max}}$ determines the separation between a 2D ($\eta < 2$), quasi-2D ($2 < \eta < 8$) and 3D ($\eta > 8$) regime. In the inset the position of $v_c^{\max}$ is referred to the 2D BCS-BEC crossover tuning parameter for small η values (in linear scale), showing the expected position in 2D of $v_c^{\max}$. Partially from [67].*

linear coefficient provides a prediction of the position of the 3D maximum critical velocity in terms of the parameter $1/(k_F^{3D}a_{3D})$. The MF theory predicts the critical velocity to be slightly on the BEC side at approximately $1/(k_F^{3D}a_{3D})_{v_c^{\max}} \simeq 0.07$ [109] while within the GPF approach we fit the linear behaviour for large η and we obtain $(1/k_F^{3D}a_{3D})_{v_c^{\max}} \simeq 0.056$. In the 2D limit we consider the relation between the 2D and the quasi-2D tuning parameters,

$$\frac{1}{k_F a} = \frac{\sqrt{6\pi}}{\eta^{3/2}} \text{arcsinh}\left[\frac{1}{2}\exp\left(\frac{l_z}{2a_{3D}}\right)\right]. \tag{4.74}$$

It is reasonable to assume that, at the position where the Landau critical velocity takes the maximum value, we have a finite limit $\lim_{\eta \to 0}[\ln(k_F a)]_{v_c^{\max}}$, which means we must impose a logarithmic decay of $(l_z/a_{3D})_{v_c^{\max}}$ as a function of η. We observe that Eq. (4.74) implies

$$\left(\frac{l_z}{a_{3D}}\right)_{v_c^{\max}} \sim_{\eta \to 0} -2\ln(k_F a) - \ln\frac{3\pi}{2} + 3\ln\eta \tag{4.75}$$

We thus can compute the position of the Landau critical velocity peak in the 2D limit fitting our data and we obtain,

$$\ln(k_F^{2D}a_{2D}) = \lim_{\eta \to 0}[\ln(k_F a)]_{v_c^{\max}} \simeq 0.72 \tag{4.76}$$

as represented by the inset of Figure 4.13. This extracted position of the peak of the Landau critical velocity in the 2D limit is consistent with the position of the peak of the contact, $\ln(k_F^{2D} a_{2D}) \sim 1$, obtained recently via auxiliary-field Monte Carlo simulations for a 2D interacting Fermi gas [104].

4.4.3 Dynamic structure factor

A practical way to measure both the speed of sound, c_s, and the order parameter, Δ, is via Bragg spectroscopy. The spectroscopic response probes the dynamic structure factor [110–112], which in the case of a Fermi superfluid exhibits a peak corresponding to the Bogoliubov-Anderson phonon mode and a continuum of particle-hole excitations [109]. The experimental probing of excitation spectra is a well-established tools in ultracold gases: shining two lasers with the same frequency at a different incidence angle allows the transfer of a net amount of momentum (cft. Ref. [113]).

Due to the presence of a pairing gap in the excitation spectrum, an external excitation of momentum $\mathbf{Q}_r$ is collective if it does not break pairs when it excites states with energy below the threshold,

$$
\omega_{\text{th}}(\mathbf{Q}_r) = \begin{cases} 2\Delta & \mu > 0 \text{ and } \hbar^2 \mathbf{Q}_r^2 \leq 8m\mu \\ 2\sqrt{\mu_{\mathbf{Q}_r}^2 + \Delta^2} & \text{otherwise} \end{cases}, \tag{4.77}
$$

where $\mu_{\mathbf{Q}_r} = \mu - \hbar^2 \mathbf{Q}_r^2/(8m)$, and for our dimensional crossover system with finite transverse periodic length l_z, we have set $\mathbf{Q}_r = (q_r, q_z)$, a combination of an in-plane momentum q_r, and a transverse excitation, $q_z = 2\pi n_z/l_z$ for fixed integer n_z (see Eq.(4.70)). We note that the calculation of the dynamic structure factor $S(\mathbf{Q}_r, \omega)$ within the GPF theory is notoriously difficult [74], so we instead use the random phase approximation within the mean-field framework [114].

In Fig. 4.14, we plot the dynamic structure factor in the quasi-2D regime at $\eta = 4$, normalized by the number of particles N and recoil energy $\omega_r = \hbar \mathbf{Q}_r^2/(2m)$ for three different recoil momenta, (a) $\mathbf{Q}_r = (3.2k_F, 0)$, (b) $\mathbf{Q}_r = (0.6k_F, 0)$ and (c) $\mathbf{Q}_r = (0, 2\pi/l_z)$. One observes in Figs. 4.14(a)-(b) that the response is similar to the 3D case [114], showing the characteristic peaks in the continuum spectrum for $\omega > \omega_{\text{th}}$, and the presence of the phonon mode. We note the appearance of a second peak, marked by $\omega_{\text{th}}(q_r, 4\pi/l_z)$ (green dashed) in Fig. 4.14(a), corresponding to the generation of a transverse excitation. The response at $\omega_{\text{th}}(q_r, 2\pi/l_z)$ is absent, due to the need of the system to excite two modes along z with opposite momenta, in order to conserve the total momentum. The same structure, present in Fig. 4.14(b), is not resolved due to the energy required at this momentum.
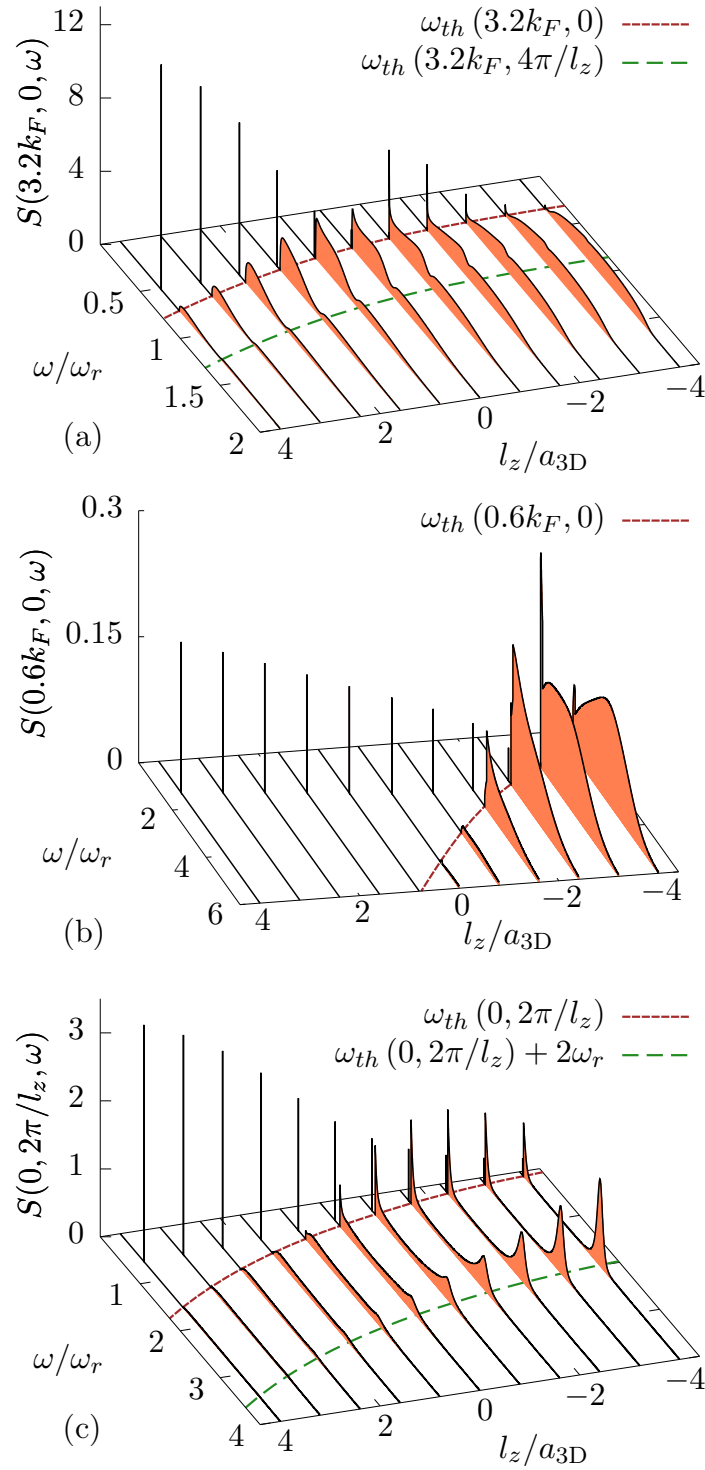
Figure 4.14: *The density DSF $S(\mathbf{Q}_r, \omega)$ scaled by the ratio ω_r/N, where ω_r is the recoil energy and N the particle number, in the quasi-2D regime for $\eta = 4$ at various interaction strengths l_z/a_{3D}, with the in-plane recoil momentum $\mathbf{Q}_r = (3.2k_F, 0)$ (a), $\mathbf{Q}_r = (0.6k_F, 0)$ (b) and transverse recoil momentum $\mathbf{Q}_r = (0, 2\pi/l_z)$ (c). The spectral width of the Bogoliubov-Anderson phonon peak is illustrated by the height of the delta function. From [67].*

The dynamic response of the system, for a transverse recoil momentum $\mathbf{Q}_r = (0, 2\pi/l_z)$, is shown in Fig. 4.14(c), and has a specific structure due to the quasi-2D regime. Conservation of total momentum forces in-plane excitations to place the second continuum peak at $\omega_{\mathrm{th}}(4\pi/l_z, 2\pi/l_z)$ and gives no response at $\omega_{\mathrm{th}}(2\pi/l_z, 2\pi/l_z)$, which would break momentum conservation. We expect this to be a signature of the quasi-2D regime, as in 3D the pairing gap between box modes, $2\pi/l_z$, goes to zero and the isolated peaks merge in a continuous structure, while in 2D, the peak $\omega_{\mathrm{th}}(0, 2\pi/l_z) + 2\omega_r$ moves too far away from the main spectrum.

Chapter 5

Breathing mode frequency of a trapped ultracold Fermi gas

Expanding the research outlined in the previous chapter, we exploit the low dimensional crossover setup to address the quantum anomaly associated with the breathing mode frequency of a harmonically trapped gas. As we briefly described in the introduction (see Sec. 1.3.3), the low-dimensional regimes are experimentally achieved by using a combination of harmonic oscillator (HO) traps [93, 94], whose oscillating frequencies are tuned in order to reach both two-dimensional (2D) pancake [66, 115] and one-dimensional (1D) cigar traps [116].

The interest around low-dimensional quantum gases, in particular for the 2D case, is further emphasized by the features associated with phenomena that don't have a classical counterpart. In two dimensions, the dynamics Hamiltonian may present itself with invariance under length scaling, but, upon quantisation, the introduction of a scattering length a_{2D}, breaks the scale invariance of the associated classical Hamiltonian and leads to the phenomenon of the so-called *quantum anomaly* [117].

When an ultracold quantum gas is confined via harmonic trapping, with a selected aspect ratio (see Sec. 1.3.2), a small perturbation of the transverse harmonic frequency $\omega_\perp$ induces a breathing mode excitation whose frequency is given by $\omega_B = 2\omega_\perp$ [118, 119]. This classical result is modified when the scattering T-matrix of the system is healed from symmetry failure. The breathing mode frequency gains a dependence on a_{2D} and deviates from the classical value, $\omega_B = 2\omega_\perp$, within a range of $5 - 10\%$ [71, 120, 121]. This should be contrasted with the case of a three-dimensional gas, in which the classical Hamiltonian is in general not invariant under length scaling, with the only notable exception of the 3D unitarity limit, where the scattering length diverges, $a_{3D} = \pm\infty$, and the quantum Hamiltonian becomes again scale invariant. As a result of the restored scale invariance, the breathing mode does

not depend on the temperature [122].

Motivated by the recent experimental activities at Swinburne University of Technology [123, 124], we address the role of dimension and interaction on the breathing mode frequency and the quantum anomaly. As already pointed out, low dimensionality requires a beyond mean-field (MF) treatment, which is made possible through the framework of the dimensional crossover described in Chap. 4, while the effect of harmonic trapping in the transverse direction on the integrated 2D density distribution can be well described by some schemes of local density approximation (LDA).

By using a sum-rule approach, in the spirit of Ref. [125], we determine the breathing mode frequency while changing the dimensional regime and tuning the scattering length. We further address a comparison with the previous results of the breathing mode frequency in the purely 2D regime [71, 121, 126].

5.1 Theoretical models

5.1.1 Homogeneous strongly interacting Fermi gases at the dimensional crossover

In the spirit of Ref. [67] and the discussion presented in Chap. 4, we introduce the tuning parameters of the dimensional crossover as follows: the in-plane coordinates are sent to the thermodynamic limit, while we require PBC to hold in the axial direction. The characteristic PBC length l_z tunes the dimensional crossover from the 3D (large l_z) limit towards the 2D (small l_z) regime. We define the characteristic Fermi momentum k_F and Fermi energy $\varepsilon_F = \hbar^2 k_F^2/(2m)$ from the free Fermi density n_f. That is, for a fixed box length l_z, we take the discretisation of momenta in the z direction, $k_z = 2\pi N_z/l_z$, for any integer N_z. The free Fermi density is then given by,

$$n_f = \frac{1}{2\pi l_z} \sum_{N_z=-N_{\max}}^{N_{\max}} \left[k_F^2 - \left(\frac{2\pi N_z}{l_z} \right)^2 \right], \tag{5.1}$$

where $N_{\max}$ is the largest natural number smaller than $k_F l_z/(2\pi)$. In the 2D and 3D limits, the Fermi momentum k_F should approach respectively their limiting values, k_F^{2D} and k_F^{3D}, which can be defined by the 2D and 3D free Fermi densities $n_{2D} = n_f l_z$ and $n_{3D} = n_f$ in the usual way. For convenience, we introduce the *dimensional crossover tuning parameter* via the 3D Fermi momentum k_F^{3D}:

$$\eta \equiv k_F^{3D} l_z. \tag{5.2}$$

We renormalise the bare interaction strength, U_0, by requiring that the two-body T-matrices in the quasi-2D and 3D regimes match when $l_z \to \infty$, which

defines a quasi-2D binding energy B_0 [70, 108] as a function of a_{3D}, with an explicit dependence on l_z,

$$B_0 = \frac{4\hbar^2}{ml_z^2} \operatorname{arcsinh}^2 \left[\frac{e^{l_z/(2a_{3D})}}{2} \right]. \qquad (5.3)$$

The binding energy fixes the *BCS-BEC crossover tuning parameter* l_z/a_{3D} which spans from negative (BCS) to positive (BEC) values. When $l_z \to 0$, the quantity $B_0/(2\varepsilon_F)$ is well defined and spans the 2D BCS-BEC crossover by introducing

$$-\ln\left(k_F^{2D} a_{2D}\right) = -\ln\sqrt{\frac{B_0}{2\varepsilon_F}}. \qquad (5.4)$$

Finally, we can define the density of the system as a function of two parameters, namely the chemical potential, μ, and the PBC length, l_z, via the number equation

$$n(\mu, l_z) = -\frac{1}{V} \frac{\partial \Omega(\mu, l_z)}{\partial \mu} \bigg|_{\mu; \Delta(\mu)}, \qquad (5.5)$$

where the thermodynamic potential is given by the same procedure of Sec. 4.3.2, for each pair (μ, l_z), $\Delta(\mu)$ means that we have solved the gap equation before taking the derivative.

5.1.2 Local density approximation

As we shall see, the breathing mode frequency in the transverse plane can be calculated from the integrated 2D density,

$$n_{2D}(\rho = \sqrt{x^2 + y^2}) = \int dz\, n(\rho, z), \qquad (5.6)$$

by using a sum-rule approach. We now discuss how to determine the column density using the uniform density equation of state Eq. (5.5) and the LDA approach, in the presence of a harmonic trapping potential in the xy-plane and two types of confinement in the axial direction [72]:

$$V_T(\rho, z) = \frac{1}{2} m\omega_\perp^2 \rho^2 + \begin{cases} V_\infty \Theta\left[|z| - l_z/2\right], \\ \frac{1}{2} m\omega_z^2 z^2, \end{cases} \qquad (5.7)$$

where the potential $V_\infty \Theta[|z| - l_z/2]$, with $V_\infty \to \infty$ and step function $\Theta(x)$ simulates a hard-wall box confinement that may be realized in future experiments. The energy $m\omega_z^2 z^2/2$ is the standard harmonic trapping potential [66, 115]. In both cases, the trap aspect ratio, characterized by $\lambda = \hbar/(m\omega_\perp l_z^2)$ under the hard-wall confinement and $\lambda = \omega_z/\omega_\perp$ in the case of harmonic potential, should be larger than 1.

To calculate the column density, let us first clarify the different dimensional regimes. Starting from Chap. 4, the dimensional crossover of a PBC system, which

could be used to describe a nearly homogeneous quasi-2D Fermi gas with hard-wall confinement, is split into three regimes. The position of the maximum of the superfluid critical velocity, v_c^{max}, which has a non-trivial dependence on the dimensional parameter, η (see Chap. 4), marks the different dimensional regimes [67]. For $\eta \leq 2$ the maximum of the superfluid velocity is logarithmically dependent on η, and we denote this as the 2D regime. The maximum of the superfluid velocity becomes linear in η when $\eta \geq 8$ marking the 3D regime (see Fig. 4.13). The non-monotonic region contained between the 2D and 3D regimes is the quasi-2D regime. We determine the appropriate PBC length scale by approximating

$$l_z \sim l_z^{\text{HO}} = \sqrt{\frac{\hbar}{m\omega_z}}. \tag{5.8}$$

and by doing so, Eq. (5.5) depends on l_z as an external parameter fixed by the axial harmonic frequency ω_z. We then compare l_z with k_F^{3D} and obtain a simple relation to compare the PBC to the harmonically trapped system,

$$\eta \sim k_F^{\text{3D}} l_z^{\text{HO}} = \sqrt{\frac{2\varepsilon_F^{\text{3D}}}{\hbar\omega_z}}. \tag{5.9}$$

The single-particle criterion for the harmonically trapped Fermi gas in the 2D regime is given by requiring: (1) $k_B T \ll \varepsilon_F$ to avoid thermal excitations of the axial harmonic oscillator ground state, and (2) $\hbar\omega_z > \varepsilon_F$ to ensure that the whole system is contained in the ground state. By solving $n_{\text{3D}} = n_f$, we see that from Eq. (5.1) we always have $\varepsilon_F < \varepsilon_F^{\text{3D}}$ for $\eta < 3\pi/2$. By taking $k_F^{\text{3D}} l_z^{\text{HO}} < \sqrt{2}$, we may interpret $k_F^{\text{3D}} l_z < \sqrt{2}$ as a good approximate regime of the 2D limit for the trapped case. We denote this regime as the harmonic oscillator (HO) 2D regime. This distinguishes between the PBC 2D regime and the 2D regime for a harmonically trapped Fermi gas.

5.1.3 LDA schemes

For a hard-wall confinement along the axial direction, the density distribution is nearly uniform as a function of z. The work on the dimensional crossover can thus be quantitatively applicable. The column density is given by,

$$n_{2D} [\mu(\rho)] = l_z n [\mu(\rho), l_z], \tag{5.10}$$

where $n[\mu(\rho), l_z]$ can be calculated using Eq. (5.5), once a local chemical potential $\mu(\rho)$ is given as a function of the 2D plane radius. For a slowly varying transverse potential $m\omega_\perp^2 \rho^2/2$, the assignment of a local chemical potential is known to be a good approximation, as the surface energy related to the potential change becomes

negligible compared to the bulk energy scale. We have a local chemical potential in Eq. (5.10):

$$\mu\left(\rho\right) = \mu_g - \frac{1}{2}m\omega_\perp^2\rho^2, \tag{5.11}$$

where the chemical potential at the trap center μ_g should be adjusted to return the total number of atoms N, i.e.,

$$N = 2\pi\int_0^\infty \rho n_{2D}\left(\rho\right)d\rho. \tag{5.12}$$

In the following, this LDA scheme is referred to as the *in-plane* LDA.

The situation becomes harder for a harmonic axial trapping potential. This soft-wall potential allows density variation also in the axial direction and independence from the axial direction cannot be inferred. As the confinement is tight along the z-direction, we are of course not allowed to use Eq. (5.5) to calculate $n_{2D}\left(\rho\right)$. However, as all the atoms are confined in the ground state of the tight confinement, the in-plane motion of the atoms should be universally described by the same 2D Hamiltonian, regardless of the detailed form of the confinement. This implies that the 2D density equation of state $n_{2D}(\mu)$ should be independent of the form of tight confinement, as far as the confinement gives the same 2D binding energy or 2D scattering length [72]. Therefore, we could still use Eq. (5.10) to determine the column density, provided that the length l_z is accurately approximated in the presence of the axial harmonic trapping potential. Away from the deep 2D limit, we expect this approximation to increasingly fail in describing the harmonically confined system when the dimensional parameter η moves towards the quasi-2D and 3D regimes of the PBC confined model. Fortunately, in the deep 3D regime, the axial trapping potential $m\omega_z^2 z^2/2$ becomes slowly varying in space as well. In this case, we may implement an *all-direction* LDA scheme, by setting

$$\mu(\rho, z) = \mu_g - \frac{1}{2}m\omega_\perp^2\rho^2 - \frac{1}{2}m\omega_z^2 z^2. \tag{5.13}$$

We can introduce a new set of variables, $\xi^2 = \rho^2 + \lambda^2 z^2$ and $\tan\psi = \lambda z/\rho$, and rewrite the chemical potential as a function of ξ only: $\mu(\xi) = \mu_g - m\omega_\perp^2\xi^2/2$, for a fixed aspect ratio λ. The number of particles, N, of the system approximated with LDA, in cylindrical coordinates, is given by

$$N = 2\pi\int_{-\infty}^\infty dz\int_0^\infty d\rho\,\rho\,n\left[\mu(\rho, z)\right]. \tag{5.14}$$

The above equation can be used as well for the in-plane LDA to replace Eq. (5.12), if we require $n(\rho, l_z) = n(\rho)$ when $z \in [-l_z/2, l_z/2]$ and $n(\rho, l_z) = 0$ otherwise.

As a brief summary, in the presence of an axial harmonic trapping potential, we will use the in-plane LDA in the 2D regime and the all-direction LDA in the

3D regime, as an accurate description for the column density equation of state. At
the 2D-3D crossover, we take interpolation between these two limits and obtain a
qualitative description.

5.1.4   Breathing mode frequency

When the particle density assumes a poly-tropic form,

$$\mu(n_{2D}) \propto n_{2D}^{\gamma}, \tag{5.15}$$

it is very simple to infer the breathing mode frequency associated with small per-
turbations, in the deep 2D limit, of the transverse harmonic trapping. The weak
violation of the scale invariance implies that [71, 126]

$$\gamma_{2D} \sim 1, \tag{5.16}$$

regardless of the type of the tight axial confinement. In the 3D regime, considering
a unitary Fermi gas, the equation of state is given by

$$\mu = \xi \varepsilon_F \propto n^{2/3}, \tag{5.17}$$

where ξ is the Bertsch parameter [93], and it returns,

$$\gamma_{3D}^{(\text{HW})} = 2/3, \tag{5.18}$$

$$\gamma_{3D}^{(\text{HO})} = 1/2, \tag{5.19}$$

where the labels "HW" and "HO" separate the hard-wall and harmonic axial trap-
ping potentials cases. The second result is justified by the discussion at the begin
of this chapter.

When the particle density is known, as a function of the chemical potential, the
breathing mode frequency associated with collective oscillations of the Fermi gas can
be derived from the hydrodynamic treatment of the system [125, 127]. The sum-rule
methods, presented in Refs. [121, 128], return the breathing mode frequency, ω_B, as

$$\hbar^2 \omega_B^2 = \frac{M_1}{M_{-1}}. \tag{5.20}$$

M_1 is given by the energy weighted moment of the density (second order central
momentum of the density distribution), $M_1 = 2N\hbar^2 \langle \rho^2 \rangle / m$, and M_{-1} is related to
a perturbation of the radial coordinate, $M_{-1} = N\delta \langle \rho^2 \rangle / \varepsilon$, where $\delta \langle \rho^2 \rangle$ represents
the second order momentum when the transverse harmonic oscillator potential is
perturbed by $-\varepsilon \rho^2$. The expectation value of the radius squared is given by,

$$\langle \rho^2 \rangle \propto \int_0^\infty \rho^3 n_{2D}(\rho) d\rho \tag{5.21}$$

and we can recast the perturbation of the radial coordinate to a perturbation of $\omega_\perp$, obtaining the closed form [125]

$$\hbar^2 \omega_B^2 = -2\langle \rho^2 \rangle \left[\frac{d\langle \rho^2 \rangle}{d(\omega_\perp^2)} \right]^{-1}. \tag{5.22}$$

From Eq. (5.22) we observe that we need to know $\langle \rho^2 \rangle$ up to any constant which doesn't implicitly depend on $\omega_\perp$ and we will show how Eq. (5.22) doesn't depend on the number of particles when we divide the equation by the factor $\omega_\perp$. In case of a poly-tropic equation of state, the sum-rule method becomes exact [129, 130],

$$\frac{\omega_B}{\omega_\perp} = \sqrt{2 + 2\gamma}. \tag{5.23}$$

Therefore, we anticipate that in different dimensional regimes the breathing mode frequency may behave like,

$$\omega_{B,2D} \sim 2\omega_\perp, \tag{5.24}$$

$$\omega_{B,3D}^{(HW)} = \sqrt{10/3}\,\omega_\perp, \tag{5.25}$$

$$\omega_{B,3D}^{(HO)} = \sqrt{3}\,\omega_\perp. \tag{5.26}$$

The latter two results hold for a unitary Fermi gas only.

5.2 Sum rule for the breathing mode frequency

According to Eq. (5.22), we need to know $\langle \rho^2 \rangle$ up to any constant which is not dependent on $\omega_\perp$, and prove the independence of the ratio $\frac{\omega_B}{\omega_\perp}$ from the number of particles.

5.2.1 The in-plane LDA case

Starting from Eq. (5.21), we impose $n_{2D}(\rho) = l_z n(\rho)$, since $n(\rho, z) = n(\rho)$ when $z \in [-l_z/2, l_z/2]$ and vanishing otherwise. We then apply the LDA and we require $n(\rho) \equiv n[\mu(\rho)]$ where

$$\mu(\rho) = \mu_g - \frac{1}{2} m \omega_\perp^2 \rho^2 \tag{5.27}$$

and μ_g is a constant. Thus we can compute Eq. (5.14) and Eq. (5.21) employing a change of variables from ρ to μ,

$$-\frac{d\mu}{m\omega_\perp^2} = \rho d\rho, \qquad \rho = \frac{1}{\omega_\perp} \sqrt{\frac{2}{m}(\mu_g - \mu)}, \tag{5.28}$$

with $\mu(\rho = 0) = \mu_g$ and $\mu(\rho = \infty) = -\infty$. We thus obtain, from Eq. (5.14)

$$\frac{Nm}{2\pi l_z} \omega_\perp^2 = \int_{-\infty}^{\mu_g} d\mu \; n(\mu) \tag{5.29}$$

which is always convergent, as when $\mu \leq -B_0/2$ we have $n = 0$. Also, to simplify the notation we introduce the constant $\kappa_p = Nm/(2\pi l_z)$ and a new variable $y = \kappa_p \omega_\perp^2$. From the definition of the density $n(\mu) = -\partial_\mu \Omega$, we integrate to obtain,

$$y = -\Omega(\mu_g). \tag{5.30}$$

From Eq. (5.29) then we can numerically compute the dependency of μ_g on $\omega_\perp$, via the function $\mu_g \equiv \mu_g(y)$. Also by applying the same change of variable as before, we obtain from Eq. (5.21),

$$\langle \rho^2 \rangle \propto -\frac{1}{y^2} \int_{-\infty}^{\mu_g(y)} d\mu \; \Omega(\mu). \tag{5.31}$$

Since we have $d/d(\omega_\perp^2) \propto d/dy$, we obtain

$$\frac{d}{dy}\langle \rho^2 \rangle \propto -\frac{2}{y}\langle \rho^2 \rangle - \frac{1}{y^2}\frac{d}{dy} \int_{-\infty}^{\mu_g(y)} d\mu \; \Omega(\mu). \tag{5.32}$$

We use the fact that Ω turns out to be always strictly monotonically decreasing, which means that y is a strictly monotonic increasing function of μ_g and we can apply the inverse derivative theorem globally, i.e.

$$\frac{d}{dy} = \left(\frac{dy}{d\mu_g}\bigg|_{\mu_g(y)} \right)^{-1} \frac{d}{d\mu_g}\bigg|_{\mu_g(y)}, \tag{5.33}$$

which gives

$$\frac{d}{dy}\langle \rho^2 \rangle \propto -\frac{2}{y}\langle \rho^2 \rangle + \frac{1}{y}\frac{1}{n[\mu(y)]}. \tag{5.34}$$

Finally, due to the proportionality constant κ_p, we can compute

$$\frac{\omega_B^2}{\omega_\perp^2} = -\frac{2}{y}\frac{\langle \rho^2 \rangle}{d\langle \rho^2 \rangle/dy} = \left(1 - \frac{1}{2n[\mu_g(y)]\langle \rho^2 \rangle} \right)^{-1}. \tag{5.35}$$

For a poly-tropic density equation of state, which takes the following form with the step function $\Theta(x)$,

$$n(\mu) \propto \left(\mu + \frac{B_0}{2} \right)^{1/\gamma} \Theta\left[\mu + \frac{B_0}{2} \right], \tag{5.36}$$

it is easy to see that

$$\Omega(\mu) \propto \left(\mu + \frac{B_0}{2} \right)^{(1+\gamma)/\gamma}, \tag{5.37}$$

$$y \propto \left(\mu_g + \frac{B_0}{2} \right)^{(1+\gamma)/\gamma}, \tag{5.38}$$

$$\langle \rho^2 \rangle \propto \left(\mu_g + \frac{B_0}{2} \right)^{(1+2\gamma)/\gamma}, \tag{5.39}$$

by using Eqs. (5.30) and (5.31), respectively. Thus, we obtain

$$\langle \rho^2 \rangle \propto y^{-1/(1+\gamma)}. \tag{5.40}$$

Using Eq. (5.35) we also arrive at the well-known sum-rule relation,

$$\frac{\omega_B^2}{\omega_\perp^2} = 2 + 2\gamma. \tag{5.41}$$

In actual computations, the density equation of state generally does not follow the idealized poly-tropic form. Using the GPF theory as outlined in Sec. 5.1.1, we calculate the thermodynamic function $\Omega(\mu)$ for a broad range of values at a given set of parameters (such as l_z and 3D scattering length a_{3D}), starting from the minimum chemical potential $-B_0/2$ where $\Omega = 0$. We then compute the quantity $y^2 n[\mu_g(y)]\langle \rho^2 \rangle$, which is quadratic in y by solving Eq. (5.30). We fit the results with a quadratic function and extract the second order Taylor coefficient at each y, using this coefficient in Eq. (5.35) to directly obtain $\omega_B/\omega_\perp$. We finally convert the peak density at the trap centre $n_0 = n[\mu_g(y)]$ at the given y to the 3D Fermi momentum at the trap centre $k_F^{3D} = (3\pi^2 n_0)^{1/3}$ and show the breathing mode frequency $\omega_B/\omega_\perp$ as a function of the dimensional parameter $k_F^{3D} l_z$.

5.2.2 The all-direction LDA case

The all-direction LDA mirrors the procedures for the in-plane LDA case. Again we start from the number equation and exploit the symmetry in z,

$$N = 4\pi \int_0^\infty dz \int_0^\infty d\rho \ \rho \ n\left[\mu\left(\rho, z\right)\right], \tag{5.42}$$

where we have assumed

$$\mu(\rho, z) = \mu_g - \frac{1}{2} m \omega_\perp^2 (\rho^2 + \lambda^2 z^2). \tag{5.43}$$

The variables z and ρ span the first quadrant of $\mathbb{R}^2$ and such a surface can be mapped by the polar coordinates $\xi \in [0, \infty]$ and $\psi \in [0, \pi/2]$, defined as

$$\xi^2 = \rho^2 + \lambda^2 z^2 \qquad \tan\psi = \frac{\lambda z}{\rho}. \tag{5.44}$$

The number of particles is,

$$\frac{N\lambda}{4\pi} = \int_0^\infty d\xi \left[\xi^2 n(\xi)\right]. \tag{5.45}$$

A change of variables, identical to Eq. (5.28), allows us to obtain,

$$y = \kappa_c \omega_\perp^2 = -\int_{-\infty}^{\mu_g} d\mu \sqrt{\mu_g - \mu} \ \frac{d\Omega}{d\mu}, \tag{5.46}$$

with

$$\kappa_c = \frac{N\omega_z}{2\pi}\left(\frac{m}{2}\right)^{3/2}\omega_z = \kappa_p\frac{l_z\omega_z}{2}\sqrt{\frac{m}{2}}. \tag{5.47}$$

By applying $l_z \simeq \sqrt{\hbar/(m\omega_z)}$, we obtain the ratio $\kappa_c/\kappa_p = \hbar/(2\sqrt{2}ml_z)$. With a very similar procedure we also compute

$$\langle\rho^2\rangle \propto -\frac{1}{y^2}\int_{-\infty}^{\mu_g(y)}d\mu\,\sqrt{\mu_g(y)-\mu}\,\Omega(\mu), \tag{5.48}$$

and then its derivative,

$$\frac{d\langle\rho^2\rangle}{dy} \propto -2y^{-1}\langle\rho^2\rangle - y^{-2}\frac{d}{dy}\int_{-\infty}^{\mu_g(y)}d\mu\sqrt{\mu_g(y)-\mu}\,\Omega(\mu). \tag{5.49}$$

Since $\mu_g(y)$ is a monotonic function of y we can invert the derivative globally by using Eq. (5.33), which introduces the quantity

$$I(\mu_g) = \frac{dy}{d\mu_g} = -\int_{-\infty}^{\mu_g}d\mu\sqrt{\mu_g-\mu}\,\frac{d^2\Omega}{d\mu^2}, \tag{5.50}$$

and, as observed before,

$$\frac{d}{d\mu_g}\int_{-\infty}^{\mu_g(y)}d\mu\sqrt{\mu_g-\mu}\,\Omega(\mu) = -y. \tag{5.51}$$

Similarly to the in-plane LDA case, we have

$$\frac{\omega_B^2}{\omega_\perp^2} = \left(1 - \frac{1}{2I(\mu_g(y))\langle\rho^2\rangle}\right)^{-1}. \tag{5.52}$$

The computation of the breathing mode frequency in the all-direction LDA requires a further step. We are going to fit quadratically the function $y \mapsto y^2 I(\mu_g(y))\langle\rho^2\rangle$ and obtain the second order Taylor coefficient, as for the in-plane LDA, but we need to consider an important subtlety. The number of particles, N, was hidden by the y variable in both in-plane and all-direction schemes and these need to be the same in order to make a consistent comparison in the case of the harmonic axial trapping potential. Eq. (5.46) needs to be computed for a fixed κ_p and then the ratio κ_c/κ_p has to be adjusted according to the choice of l_z that we are considering. By doing so we are not modifying the form of Eq. (5.52), but only adjusting μ_g to the correct number of particles (which is never explicit but fixed) in Eq. (5.46).

5.3   Results

We outline in this final section the results provided by the implementation of the previously described LDA schemes to the dimensional crossover model. Hereafter,
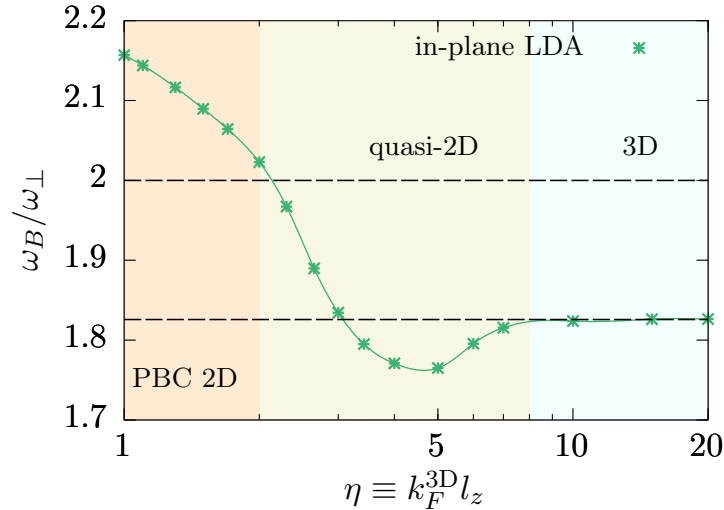
Figure 5.1: *The breathing mode frequency ω_B in units of $\omega_\perp$ as a function of the dimensional crossover tuning parameter $\eta \equiv k_F^{3D} l_z$, when the BCS-BEC crossover is tuned at unitarity with $a_{3D} = \infty$. Here, we consider the hard-wall confinement along the axial direction. The upper and bottom dashed lines are the scale invariant predictions in the 2D and 3D limits, $\omega_{B,2D} = 2\omega_\perp$ and $\omega_{B,3D}^{(HW)} = \sqrt{10/3}\omega_\perp \simeq 1.83\omega_\perp$, respectively. From [72].*

without any confusions we use $k_F^{3D} \equiv (3\pi^2 n_0)^{1/3}$ to represent the 3D Fermi momentum of an *interacting* Fermi gas at the trap centre with density $n_0 \equiv n(\rho = 0, z = 0)$. In our case of considering two different axial confinements, this turns out to be a more convenient option than the use of the 3D Fermi momentum of an ideal Fermi gas at the trap centre.

In Fig. 5.1 and Fig. 5.2, we show the dimensional regimes as a function of η (according with Chap. 4) and we denote the PBC and harmonically trapped 2D regimes using different colours. The harmonically trapped Fermi gas density has been experimentally studied [50, 51] and by converting the experimentally determined threshold number density to the dimensional parameter (i.e., using Eq. (5.9)), we plot the boundary of the HO 2D regime as a function of the interaction strength $(k_F^{3D} a_{3D})^{-1}$. This is illustrated in Fig. 5.3(a) by the pink shaded region.

The hard-wall axial confinement case is only briefly outlined, as the hard-wall confinement is yet to be experimentally demonstrated. In Fig. 5.1 we present the breathing mode frequency of a unitary Fermi gas at the dimensional crossover, in the presence of a hard-wall axial confinement. The mode frequency is calculated by using the in-plane LDA, as a function of the dimensional parameter η expanding from the PBC 2D regime when $\eta \leq 2$ to the 3D regime when $\eta \geq 8$. As our GPF theory provides a reliable equation of state at the dimensional crossover, we anticipate that our prediction on the breathing mode frequency is reliable. In the PBC 2D regime, the mode frequency is larger than $2\omega_\perp$, indicating a pronounced
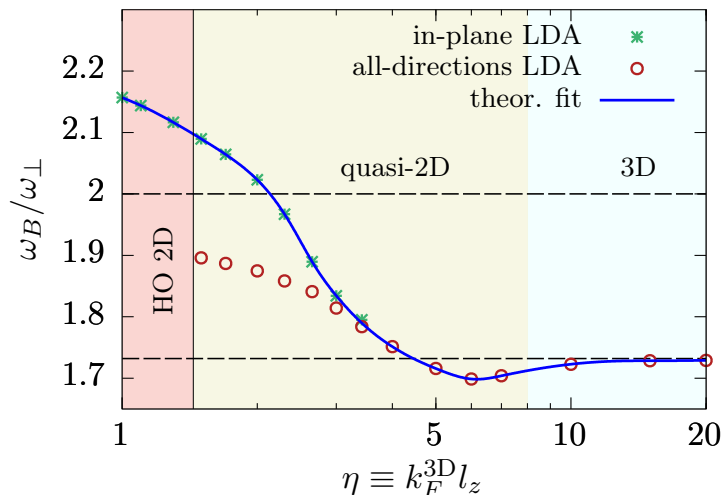
Figure 5.2: *The breathing mode frequency ω_B divided by $\omega_\perp$ as a function of the dimensional crossover tuning parameter $\eta \equiv k_F^{3D} l_z$ when the BCS-BEC crossover is tuned at unitarity with $a_{3D} = \infty$. The results from the in-plane LDA (green stars) and all-direction LDA (brown circles) schemes are merged when the lines match to form a qualitative fit (blue solid). The dimensional crossover is divided into the three dimensional regimes as in Ref. [67] and the HO 2D regime is determined using the experimental criterion of Ref. [51] for a 2D harmonically trapped Fermi gas. The upper and bottom dashed lines are the scale invariant predictions in the 2D and 3D limits, $\omega_{B,2D} = 2\omega_\perp$ and $\omega_{B,3D}^{(HO)} = \sqrt{3}\omega_\perp \simeq 1.73\omega_\perp$, respectively. From [72].*

quantum anomaly. As we move to the quasi-2D regime, the frequency decreases rapidly, reaches a minimum at $\eta \sim 5$ and finally approaches the 3D limiting value of $\omega_{B,3D}^{(HW)} = \sqrt{10/3}\omega_\perp$ at $\eta \geq 10$.

5.3.1   The harmonic axial confinement

In Fig. 5.2, we show the dimensional crossover of the breathing mode again for the unitary Fermi gas, but with the harmonic axial trapping potential. Here, the 3D regime is reached as before when $\eta \geq 8$, and the HO 2D regime is realized when $\eta \leq \sqrt{2}$. As we mentioned earlier, we calculate the breathing mode frequency using the in-plane LDA scheme near the 2D regime (green stars) and using the all-direction LDA scheme close to the 3D regime (brown circles). The in-plane LDA fails to describe the 3D regime, so we show its prediction at $\eta < 4$ only. The all-direction LDA scheme fails in the 2D regime, since the ground state wavefunction in the axial direction is essentially a Gaussian. As a guide to the eyes, we combine the two different LDA schemes with the blue solid line, and this qualitatively describes the breathing mode frequency in two mutually exclusive regions of the dimensional crossover. By increasing η, we find that the mode frequency shows the same behaviour as in the case of the hard-wall confinement: it decreases quickly

away from the 2D regime, exhibits a minimum in the quasi-2D regime and then saturates to a 3D limiting value, which is $\omega_{B,3D}^{(\mathrm{HO})} = \sqrt{3}\omega_\perp \simeq 1.73\omega_\perp$ in the presence of the harmonic trapping potential.

We now turn to describe the behaviour of the breathing mode frequency at the BEC-BCS crossover other than the unitarity limit. For this purpose, we need to distinguish different interacting regimes and *clarify* the so-called unitarity regime. In all the previous discussions, the unitarity regime and an infinite 3D scattering length are two exchangeable terminologies, both of which can be used without any confusion in the 3D regime. Away from the 3D limit, however, it seems more intuitive to define the unitarity regime as the regime where the coherence length of Cooper pairs is comparable to the inter-particle distance and where the fermionic superfluidity is most robust.

It is worth noting that, fixing a constant 3D interacting parameter is the best way to compare with experimental results, however from a theoretical point of view we want an interaction parameter which probes the same interacting regime as a function of η. If we choose the simple condition for the 3D interacting parameter, i.e. $(k_F^{3\mathrm{D}} a_{3\mathrm{D}})^{-1}$ fixed equal to a constant, when we span the dimensional parameter η, the system crosses different interacting regimes. For example, in Fig. 5.1 where we have set the 3D scattering length to infinity, we are in the unitarity regime in the 3D limit while the system enters the BEC regime for the quasi-2D and 2D regimes. In the HO 2D case, the system is even in the deep BEC regime [51]. From now on, we fix the unitary regime through the maximum of the critical velocity, as described in Chapter 4. This is a reasonable definition, since the maximum critical velocity implies the most robust fermionic superfluidity.

Figure 5.3(a) displays the choices made for the BCS (dashed-dotted green line) and BEC (dashed blue line) crossover regimes, in which the two lines are obtained by vertically shifting the maximum critical velocity curve down and up by some amounts. These choices appear to be optimal since they both span the 2D and 3D limits ($\eta = 2$ and $\eta = 20$ respectively). For the 2D limit both the PBC 2D regime and the HO 2D regime are reached, and converting the scattering length to its 2D counterpart, $\ln(k_F^{2\mathrm{D}} a_{2\mathrm{D}})$, we observe that it spans the relevant part of BCS-BEC crossover.

In Fig. 5.3(b) we plot the ratio $\omega_B/\omega_\perp$ in the different interacting regimes as per Fig. 5.3(a), the BCS (dashed dotted green), unitarity (solid red), and BEC (dashed blue) regimes. We see that the deviation of the breathing mode from the classical result, $\omega_B = 2\omega_\perp$, appears when the 2D region is entered. Since the quantum anomaly is due to the presence of the renormalisation energy B_0, which tends to vanish while approaching the BCS regime, we observe a strong deviation in the BEC regime (dashed blue) which is progressively reduced in the unitarity regime (solid

Figure 5.3: *(a) The interaction parameter $(k_F^{3D} a_{3D})^{-1}$, as a function of η, fixed by the BCS, BEC, and v_c^{max} lines in order to span the dimensional crossover and maintain the system in the BCS (dashed dotted green), unitarity (solid red), and BEC (dashed blue) interacting regimes. According to Ref. [67] the solid red line is taken to be a good criterion to distinguish the BCS and BEC regimes. (b) we show the breathing mode frequency ω_B in units of $\omega_\perp$ as a function of the dimensional crossover parameter $\eta \equiv k_F^{3D} l_z$ for the BCS (dashed dotted green), unitarity (solid red), and BEC (dashed blue) interacting regimes.*
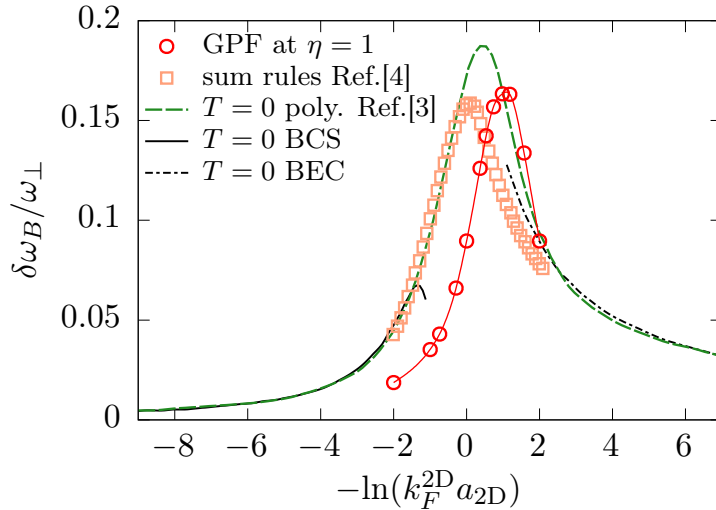
Figure 5.4: *The quantum anomaly deviation $\delta\omega_B = \omega_B - 2\omega_\perp$ of the breathing mode frequency ω_B in units of the transverse harmonic trapping frequency $\omega_\perp$. Our results (red circles) are obtained by applying the in-plane LDA for the PBC confined 2D Fermi gas ($\eta = 1$) at the GPF level. For comparison, we show also the poly-tropic fit from Ref. [71] (dashed green), the sum rule results from Ref. [121] (orange squares), and the zero temperature analytic predictions for the far BCS (solid black) and BEC (dashed-dotted black) regimes. From [72].*

red). Qualitatively, the fit between the in-plane and all-direction LDA results drop from $2\omega_\perp$ to a range of values around the 3D unitarity limit, $\omega_B = \sqrt{3}\omega_\perp$. The unitarity results (red-solid) converge to this value, while as remarked in Ref. [131], the BEC regime provides a larger value of ω_B, and in the BCS limit there is a non trivial behaviour below $\omega_B = \sqrt{3}\omega_\perp$.

5.3.2   Quantum anomaly in the deep 2D regime

The quantum anomaly associated with the scale breaking upon quantisation of the 2D Hamiltonian has been studied via Monte Carlo techniques in previous works [71, 121]. Our dimensional crossover model, according to Fig. 4.9 and the analysis of Chap. 4, associates with the $\eta < 2$ case a good agreement between the thermodynamic variables magnitudes, such as chemical potential and order parameter, and their values in the exact 2D calculations at the GPF level. Hence, we compare our results in the $\eta = 1$ case with the exact 2D calculations. Since the choice $\eta = 1$ and a large range of values of $\ln(k_F^{2D} a_{2D})$ are contained both in the PBC 2D and harmonic oscillator 2D regime, we compare the anomaly through the quantity $\delta\omega_B/\omega_\perp$, where $\delta\omega_B = \omega_B - 2\omega_\perp$.

We observe that the qualitative behaviour of the quantum anomaly is recovered by our data, and the maximum of the deviation, $\delta\omega_B$, is approximately the same

height of Ref. [121]. The shift of the anomaly to the BEC side in our results is due to either the GPF contribution to the global chemical potential μ_g in comparison to the quantum Monte Carlo schemes, or that for $\eta = 1$ the range of $\ln(k_F^{2D} a_{2D})$ is shifted with respect to the exact 2D case when we consider the exact 2D limit [72].

Chapter 6

Conclusions and Perspectives

We dedicate this final chapter to a brief summary of the work presented in this thesis. According to the title and the motivations expressed in the introduction (see Chap. 1) we have investigated some interesting features of low dimensional Fermi gases. We referred in the title to exotic phenomena in order to emphasise the non-trivial nature of their physics content, their existence in a pure quantum realm or their deviation from the mainstream theories. In this regard, we treated an exotic superfluid phase for imbalance Fermi gases, namely the LO_g phase, in Chap. 3. Motivated by experiments, we then moved towards an extension of the BCS-BEC crossover theory for low-dimensional Fermi gases exposed in Chap. 4. Finally we studied the quantum anomaly associated with the breathing mode frequency of a trapped Fermi gas, its interplay with the BCS-BEC crossover and the dimensional crossover, in Chap. 5. It follows here the list of achievements along with some future research perspectives the thesis suggested.

6.1   Summary

We studied, in Chap. 3 in detail the mean field theory of a 2D atomic Fermi gas in presence of imbalance of its spin populations. This investigations led us to consider the interplay of different pairing gap order parameters and their role in the superfluidity this gas may show. In particular, we gave precise conditions, in terms of several polarization conditions, for the appearance of an inhomogenous superfluid phases. The energy gap order parameter, which is responsible for the superfluid properties of this gas, has been self-consistently studied through numerical solutions of the Bogoliubov-de Gennes equations in the case of an s-wave scattering contact potential. The presence of imbalance and the interaction, allowed only between opposite spin particles, prevents the p-wave scattering events to be relevant at the scale of temperature we considered.

The Larkin-Ovchinnikov ansatz for the pairing gap order parameter has been refined and treated with reasonable approximations in order to make computations accessible and useful. Such refinement led us to remark the importance of the LO_g ansatz among the broad FFLO family that so far, in 2D, has been studied mainly in the FF case. The LO_g phase was found to fit a large span of the phase diagram of an interacting ultracold Fermi gas, when compared with the same system in 3D. Such configurations turned out to be energetically favourable with respect to both the FF and the original LO ansatz. The self-consistent methods smeared the order parameter in its most favourable shape including cases where many frequencies contribute to its composition. Beside, we can argue that all the FFLO family's ansatzes merge when the Fermi gas is required to have either a strong imbalance (Canonical Ensemble) or to support the presence of strong magnetic fields (Grand Canonical Ensemble). The phase diagram has been presented at both zero temperature and finite temperature. Our results indicate a clear scenario in terms of the nature of the phase transitions: the Clogston-Chandrashekar limit is superseeded with a second order phase transition from LO_g to a partially polarised free Fermi gas at large imbalance. On the other side, the BCS theory is not favourable at large imbalance condition since it undergoes a first order phase transition to the LO_g phase. In the Canonical Ensemble, this phenomenon is much more emphasised because the BCS theory cannot support a finite polarisation before the Clogston limit sets in and the BCS order parameter disappears. The LO_g phase instead takes over the finite polarisation part of the 2D Fermi gas phase diagram.

The LO_g phase, in the Canonical Ensemble, has been shown to play the role of phase separated phase supporting both a normal part and a superfluid part. The superfluid behaviour of this phase has been studied deploying a phase twisted order paramter method. We have been able to provide a qualitative graph of the superfluid density actually induced in a LO_g phase and its behaviour when we increase the gas polarisation towards the free Fermi gas transition polarization.

Most of the results on the FFLO phase are provided at the mean-field level which mimics some experimental settings for 2D or quasi-2D Fermi gases but we remarked along the work that a pair-fluctuation treatment is required to estimate the contributions due to the BKT transition and, in general, of fluctuations that in 2D are well known to be relevant.

In Chap. 4, we addressed the interplay of the BCS-BEC crossover and the dimensional crossover for an ultracold Fermi gas. Experimentally, the low-dimensional systems are achieved through harmonic trapping which in returns forces the particle density to aquire a spatial dependency.

We proposed a fully consistent new paradigm to concieve and realise low-dimensional systems inspired by recent technological advancements in ultracold gas trapping [68].

The confinement realised with hard-walls allows a large portion of the system to lay in an almost-PBC configuration, which in return makes it possible to go beyond mean-field. The importance of fluctuations in low-dimensional systems plays a remarkable role in the theory of the dimensional crossover.

Once we justified the PBC solutions on trapped Fermi gases, we moved to thoroughly characterise, at zero temperature, the physics of the dimensional crossover. We mapped out the behaviour of chemical potential and order parameter while modifying the dimensionality, we observed an agreement with the true 3D and 2D theory in the respective limiting cases. Consequently we described a criterion to distinguish weakly- and strongly-interacting regimes while we vary both the PBC periodicity and the interaction parameter. Finally we mapped out a diagram interaction vs. dimensionality which provides a visual understanding of the crossovers interplay. The diagram has been separated through the concept of superfluid maximum critical velocity that can be located in the BCS-BEC crossover region where the particles interactions are the strongest. In this way we clarified the concept of unitarity which becomes losely defined when the dimensionality is not exactly 3D. The maximum critical velocity has been computed at the gaussian fluctuations level for both the exact 3D and 2D, revealing consistencies amongst the crossover theory and the exact limiting cases.

Finally, we investigated how to probe the dimensional crossover through Bragg spectroscopy. The density dynamic structure factor, which is naturally measured with Bragg spectroscopy, marks several distinctive features for limiting 2D regime, an almost 3D regime or a middle region referred as quasi-2D. The superfluid maximum critical velocity criterion can be probed via the same spectroscopy techniques and offers a signature to distinguish the different interaction regimes.

The dimensional crossover model was also successfully employed to describe features of the harmonically trapped Fermi systems. In Chap. 5 we used the beyond mean field results of Chap. 4 combined with local density approximation schemes to better understand the breathing mode frequency of a harmonically trapped Fermi gas. Motivated by recent experiments [124, 132], we achieved a description of the breathing mode frequency compatible with the dimensional crossover previously described.

The local density approxiamation (LDA) we employed has been refined and distinguishes two different cases. To simulate a 2D setting we considered an almost-uniform axial density and an in-plane LDA while to reach 3D we used LDA in three directions. The interplay of this two schemes allowed us to map out the breathing mode frequency across different limits with a unique theory and provided, in 2D, a good comparison with previous quantum Monte Carlo calculations.

6.2   A look to the future

It has been remarked the observability of the breathing mode frequency is strongly affected by finite temperature effect. This leads us to consider a serious effort towards expanding the dimensional crossover theory at finite temperature. This development is not expected to be radically different from the point of view of the pair fluctuations theory but will require a careful computational analysis due to the significant loss of accuracy. When not possible to apply a full GPF theory we will attempt to describe the critical superfluid transition temperature in the crossover using simpler theories like Nozières and Schmitt-Rink [33].

Another interesting direction of research is a careful analysis of the 2D limit of a harmonically confined Fermi gas. As pointed out in Ref. [86], the harmonic confinement might fail to exactly reproduce the correct 2D binding energy when the axial harmonic frequency is sent to infinity. This might lead to a discrepancy in the breathing mode frequency, when computed with Monte Carlo techniques and when experimentally probed.

Bibliography

[1] R. Haag. Quantum field theories with composite particles and asymptotic conditions. *Physical Review*, 112(2):669–673, oct 1958.

[2] H. Araki, K. Hepp, and D. Ruelle. On the asymptotic behaviour of wightman functions in space-like directions. *Helvetica Physica Acta*, 35, 1962.

[3] Raymond F. Streater and Arthur S. Wightman. *PCT, Spin and Statistics, and All That.* Princeton University Press, 2000.

[4] Bose. Plancks gesetz und lichtquantenhypothese. *Zeitschrift für Physik*, 26(1):178–181, dec 1924.

[5] M. H. Anderson, J. R. Ensher, M. R. Matthews, C. E. Wieman, and E. A. Cornell. Observation of bose-einstein condensation in a dilute atomic vapor. *Science*, 269(5221):198–201, 1995.

[6] K. B. Davis, M. O. Mewes, M. R. Andrews, N. J. van Druten, D. S. Durfee, D. M. Kurn, and W. Ketterle. Bose-einstein condensation in a gas of sodium atoms. *Phys. Rev. Lett.*, 75:3969–3973, Nov 1995.

[7] Heike K. Onnes. On the sudden change in the rate at which the resistance of mercury disappears. *Comm. Phys. Lab. Univ. Leiden*, (122b), nov 1911.

[8] A. L. Robinson. Niobium-germanium: Becoming a practical superconductor. *Science*, 185(4154):846–848, sep 1974.

[9] Hiroshi Maeda, Yoshiaki Tanaka, Masao Fukutomi, and Toshihisa Asano. A new high-Tc Oxide superconductor without a rare earth element. *Japanese Journal of Applied Physics*, 27(Part 2, No. 2):L209–L210, feb 1988.

[10] M. A. Subramanian, C. C. Torardi, J. C. Calabrese, J. Gopalakrishnan, K. J. Morrissey, T. R. Askew, R. B. Flippen, U. Chowdhry, and A. W. Sleight. A new high-temperature superconductor: $Bi_2Sr_{3-x}Ca_xCu_2O_{8+y}$. *Science*, 239(4843):1015–1017, feb 1988.

[11] J. L. Tallon, R. G. Buckley, P. W. Gilberd, M. R. Presland, I. W. M. Brown, M. E. Bowden, L. A. Christian, and R. Goguel. High-tc superconducting phases in the series $Bi_{2.1}(Ca,Sr)_{n+1}Cu_nO_{2n+4+\delta}$. *Nature*, 333(6169):153–156, may 1988.

[12] L. Gao, Y. Y. Xue, F. Chen, Q. Xiong, R. L. Meng, D. Ramirez, C. W. Chu, J. H. Eggert, and H. K. Mao. Superconductivity up to 164 k in $HgBa_2Ca_{m-1}Cu_mO_{2m+2+\delta}$ (m=1, 2, and 3) under quasihydrostatic pressures. *Physical Review B*, 50(6):4260–4263, aug 1994.

[13] Pia Jensen Ray. Master's thesis: Structural investigation of $La_{(2-x)}Sr_{(x)}CuO_{(4+y)}$ - following staging as a function of temperature, 2016.

[14] J. File and R. G. Mills. Observation of persistent current in a superconducting solenoid. *Phys. Rev. Lett.*, 10:93–96, Feb 1963.

[15] J. Bardeen, L. N. Cooper, and J. R. Schrieffer. Theory of superconductivity. *Phys. Rev.*, 108:1175–1204, Dec 1957.

[16] Immanuel Bloch, Jean Dalibard, and Sylvain Nascimbène. Quantum simulations with ultracold quantum gases. *Nature Physics*, 8(4):267–276, apr 2012.

[17] M. Greiner, O. Mandel, T. Esslinger, T. W. Hänsch, and I. Bloch. Quantum phase transition from a superfluid to a Mott insulator in a gas of ultracold atoms. *Nature*, 415:39–44, jan 2002.

[18] I. Bloch. Ultracold quantum gases in optical lattices. *Nature Physics*, 1:23–30, October 2005.

[19] V. L. Berezinskiĭ. Destruction of Long-range Order in One-dimensional and Two-dimensional Systems having a Continuous Symmetry Group I. Classical Systems. *Soviet Journal of Experimental and Theoretical Physics*, 32:493, 1971.

[20] J. M. Kosterlitz and D. J. Thouless. Long range order and metastability in two dimensional solids and superfluids. (Application of dislocation theory). *Journal of Physics C Solid State Physics*, 5:L124–L126, June 1972.

[21] N. D. Mermin and H. Wagner. Absence of Ferromagnetism or Antiferromagnetism in One- or Two-Dimensional Isotropic Heisenberg Models. *Physical Review Letters*, 17:1133–1136, November 1966.

[22] W. C. Stwalley. Stability of Spin-Aligned Hydrogen at Low Temperatures and High Magnetic Fields: New Field-Dependent Scattering Resonances and Predissociations. *Physical Review Letters*, 37:1628–1631, December 1976.

[23] E. Tiesinga, B. J. Verhaar, and H. T. C. Stoof. Threshold and resonance phenomena in ultracold ground-state collisions. *Phys. Rev. A*, 47:4114–4122, May 1993.

[24] U. Fano. Effects of Configuration Interaction on Intensities and Phase Shifts. *Physical Review*, 124:1866–1878, dec 1961.

[25] H. Feshbach. A unified theory of nuclear reactions. II. *Annals of Physics*, 19:287–313, aug 1962.

[26] E. R. I. Abraham, W. I. McAlexander, J. M. Gerton, R. G. Hulet, R. Côté, and A. Dalgarno. Triplet s-wave resonance in ^{6}Li collisions and scattering lengths of ^{6}Li and ^{7}Li. *Phys. Rev. A*, 55:R3299–R3302, May 1997.

[27] J. Cubizolles, T. Bourdel, S. J. J. M. F. Kokkelmans, G. V. Shlyapnikov, and C. Salomon. Production of long-lived ultracold li$_2$ molecules from a fermi gas. *Phys. Rev. Lett.*, 91:240401, Dec 2003.

[28] K. M. O'Hara. Observation of a strongly interacting degenerate fermi gas of atoms. *Science*, 298(5601):2179–2182, nov 2002.

[29] P. Townsend and J. Sutton. Investigation by electron tunneling of the superconducting energy gaps in nb, ta, sn, and pb. *Phys. Rev.*, 128:591–595, Oct 1962.

[30] M.R. Schafroth, S.T. Butler, and J.M. Blatt. Quasichemical equilibrium approach to superconductivity. *Helv. Phys. Acta*, 30:93, 1957.

[31] D. M. Eagles. Possible pairing without superconductivity at low carrier concentrations in bulk and thin-film superconducting semiconductors. *Phys. Rev.*, 186:456–463, Oct 1969.

[32] A. J. Leggett. Interpretation of recent results on he^3 below 3 mk: A new liquid phase? *Phys. Rev. Lett.*, 29:1227–1230, Oct 1972.

[33] P. Nozières and S. Schmitt-Rink. Bose condensation in an attractive fermion gas: from weak to strong coupling superconductivity. *J. Low Temp. Phys.*, 59:195–211, 1985.

[34] Leo Radzihovsky and Daniel E Sheehy. Imbalanced feshbach-resonant fermi gases. *Rep. Prog. Phys.*, 73(7):076501, jun 2010.

[35] Lianyi He and Xu-Guang Huang. Superfluidity and collective modes in rashba spin–orbit coupled fermi gases. *Annals of Physics*, 337:163–207, oct 2013.

[36] B. DeMarco. Onset of fermi degeneracy in a trapped atomic gas. *Science*, 285(5434):1703–1706, sep 1999.

[37] P. Fulde and R. A. Ferrell. Superconductivity in a Strong Spin-Exchange Field. *Phys. Rev.*, 135:550–563, aug 1964.

[38] A. I. Larkin and Yu. N. Ovchinnikov. *Zh. Eksp. Teor. Fiz.*, 47:1136, 1964. [Sov. Phys. JETP 20, 762 (1965)].

[39] A. Bianchi, R. Movshovich, C. Capan, P. G. Pagliuso, and J. L. Sarrao. Possible fulde-ferrell-larkin-ovchinnikov superconducting state in cecoin$_5$. *Phys. Rev. Lett.*, 91:187004, Oct 2003.

[40] F. Steglich, R. Modler, P. Gegenwart, M. Deppe, M. Weiden, M. Lang, C. Geibel, T. Lühmann, C. Paulsen, J.L. Tholence, Y. Ōnuki, M. Tachiki, and S. Takahashi. Experimental evidence for a generalized FFLO state in clean type-II superconductors with short coherence length and enhanced pauli susceptibility. *Physica C: Superconductivity*, 263(1-4):498–504, may 1996.

[41] W. E. Pickett, R. Weht, and A. B. Shick. Superconductivity in ferromagnetic rusr$_2$gdcu$_2O_8$. *Phys. Rev. Lett.*, 83:3713–3716, Nov 1999.

[42] H. Burkhardt and D. Rainer. Fulde-ferrell-larkin-ovchinnikov state in layered superconductors. *Ann. Phys.*, 506(3):181–194, 1994.

[43] Daniel E. Sheehy and Leo Radzihovsky. Bec-bcs crossover in "magnetized" feshbach-resonantly paired superfluids. *Phys. Rev. Lett.*, 96:060401, Feb 2006.

[44] Daniel E. Sheehy and Leo Radzihovsky. BEC–BCS crossover, phase transitions and phase separation in polarized resonantly-paired superfluids. *Annals of Physics*, 322(8):1790–1924, aug 2007.

[45] Shaoyu Yin, J.-P. Martikainen, and P. Törmä. Fulde-ferrell states and berezinskii-kosterlitz-thouless phase transition in two-dimensional imbalanced fermi gases. *Phys. Rev. B*, 89:014507, Jan 2014.

[46] Yong Xu and Chuanwei Zhang. Berezinskii-kosterlitz-thouless phase transition in 2d spin-orbit-coupled fulde-ferrell superfluids. *Phys. Rev. Lett.*, 114:110401, Mar 2015.

[47] Xia-Ji Liu, Hui Hu, and Peter D. Drummond. Fulde-ferrell-larkin-ovchinnikov states in one-dimensional spin-polarized ultracold atomic fermi gases. *Phys. Rev. A*, 76(4):043605, oct 2007.

[48] Daniel E. Sheehy. Fulde-ferrell-larkin-ovchinnikov state of two-dimensional imbalanced fermi gases. *Phys. Rev. A*, 92:053631, Nov 2015.

[49] Umberto Toniolo, Brendan Mulkerin, Xia-Ji Liu, and Hui Hu. Larkin-ovchinnikov superfluidity in a two-dimensional imbalanced atomic fermi gas. *Phys. Rev. A*, 95:013603, Jan 2017.

[50] P. Dyke, K. Fenech, T. Peppler, M. G. Lingham, S. Hoinka, W. Zhang, S.-G. Peng, B. Mulkerin, H. Hu, X.-J. Liu, and C. J. Vale. Criteria for two-dimensional kinematics in an interacting fermi gas. *Phys. Rev. A*, 93(1):011603, jan 2016.

[51] P. Dyke, E. D. Kuhnle, S. Whitlock, H. Hu, M. Mark, S. Hoinka, M. Lingham, P. Hannaford, and C. J. Vale. Crossover from 2d to 3d in a weakly interacting fermi gas. *Phys. Rev. Lett.*, 106:105304, Mar 2011.

[52] Kirill Martiyanov, Vasiliy Makhalov, and Andrey Turlapov. Observation of a two-dimensional fermi gas of atoms. *Phys. Rev. Lett.*, 105:030404, Jul 2010.

[53] Michael Feld, Bernd Fröhlich, Enrico Vogt, Marco Koschorreck, and Michael Köhl. Observation of a pairing pseudogap in a two-dimensional fermi gas. *Nature*, 480(7375):75–78, nov 2011.

[54] Bernd Fröhlich, Michael Feld, Enrico Vogt, Marco Koschorreck, Wilhelm Zwerger, and Michael Köhl. Radio-frequency spectroscopy of a strongly interacting two-dimensional fermi gas. *Phys. Rev. Lett.*, 106:105301, Mar 2011.

[55] Alexey A Orel, Paul Dyke, Marion Delehaye, Chris J Vale, and Hui Hu. Density distribution of a trapped two-dimensional strongly interacting fermi gas. *New Journal of Physics*, 13(11):113032, nov 2011.

[56] Marco Koschorreck, Daniel Pertot, Enrico Vogt, Bernd Fröhlich, Michael Feld, and Michael Köhl. Attractive and repulsive fermi polarons in two dimensions. *Nature*, 485(7400):619–622, may 2012.

[57] Ariel T. Sommer, Lawrence W. Cheuk, Mark J. H. Ku, Waseem S. Bakr, and Martin W. Zwierlein. Evolution of fermion pairing from three to two dimensions. *Phys. Rev. Lett.*, 108:045302, Jan 2012.

[58] Y. Zhang, W. Ong, I. Arakelyan, and J. E. Thomas. Polaron-to-polaron transitions in the radio-frequency spectrum of a quasi-two-dimensional fermi gas. *Phys. Rev. Lett.*, 108:235302, Jun 2012.

[59] Vasiliy Makhalov, Kirill Martiyanov, and Andrey Turlapov. Ground-state pressure of quasi-2d fermi and bose gases. *Phys. Rev. Lett.*, 112:045301, Jan 2014.

[60] W. Ong, Chingyun Cheng, I. Arakelyan, and J. E. Thomas. Spin-imbalanced quasi-two-dimensional fermi gases. *Phys. Rev. Lett.*, 114(11):110403, mar 2015.

[61] M. G. Ries, A. N. Wenz, G. Zürn, L. Bayha, I. Boettcher, D. Kedar, P. A. Murthy, M. Neidig, T. Lompe, and S. Jochim. Observation of pair condensation in the quasi-2d BEC-BCS crossover. *Physical Review Letters*, 114(23), jun 2015.

[62] P. A. Murthy, I. Boettcher, L. Bayha, M. Holzmann, D. Kedar, M. Neidig, M. G. Ries, A. N. Wenz, G. Zürn, and S. Jochim. Observation of the berezinskii-kosterlitz-thouless phase transition in an ultracold fermi gas. *Phys. Rev. Lett.*, 115:010401, Jun 2015.

[63] Kirill Martiyanov, Tatiana Barmashova, Vasiliy Makhalov, and Andrey Turlapov. Pressure profiles of nonuniform two-dimensional atomic fermi gases. *Phys. Rev. A*, 93:063622, Jun 2016.

[64] I. Boettcher, L. Bayha, D. Kedar, P. A. Murthy, M. Neidig, M. G. Ries, A. N. Wenz, G. Zürn, S. Jochim, and T. Enss. Equation of state of ultracold fermions in the 2d bec-bcs crossover region. *Phys. Rev. Lett.*, 116:045303, Jan 2016.

[65] Chingyun Cheng, J. Kangara, I. Arakelyan, and J. E. Thomas. Fermi gases in the two-dimensional to quasi-two-dimensional crossover. *Phys. Rev. A*, 94:031606, Sep 2016.

[66] K. Fenech, P. Dyke, T. Peppler, M. G. Lingham, S. Hoinka, H. Hu, and C. J. Vale. Thermodynamics of an attractive 2d fermi gas. *Phys. Rev. Lett.*, 116(4):045302, jan 2016.

[67] Umberto Toniolo, Brendan C. Mulkerin, Chris J. Vale, Xia-Ji Liu, and Hui Hu. Dimensional crossover in a strongly interacting ultracold atomic fermi gas. *Phys. Rev. A*, 96:041604, Oct 2017.

[68] Biswaroop Mukherjee, Zhenjie Yan, Parth B. Patel, Zoran Hadzibabic, Tarik Yefsah, Julian Struck, and Martin W. Zwierlein. Homogeneous atomic fermi gases. *Phys. Rev. Lett.*, 118:123401, Mar 2017.

[69] L. P. Pitaevskii and A. Rosch. Breathing modes and hidden symmetry of trapped atoms in two dimensions. *Phys. Rev. A*, 55:R853–R856, Feb 1997.

[70] D. S. Petrov and G. V. Shlyapnikov. Interatomic collisions in a tightly confined bose gas. *Phys. Rev. A*, 64:012706, Jun 2001.

[71] Johannes Hofmann. Quantum anomaly, universal relations, and breathing mode of a two-dimensional fermi gas. *Phys. Rev. Lett.*, 108:185303, May 2012.

[72] Umberto Toniolo, Brendan C. Mulkerin, Xia-Ji Liu, and Hui Hu. Breathing-mode frequency of a strongly interacting fermi gas across the two- to three-dimensional crossover. *Phys. Rev. A*, 97:063622, Jun 2018.

[73] Ola Bratteli and Derek W. Robinson. *Operator Algebras and Quantum Statistical Mechanics*. Springer Berlin Heidelberg, 1997.

[74] Lianyi He. Dynamic density and spin responses of a superfluid fermi gas in the BCS–BEC crossover: Path integral formulation and pair fluctuation theory. *Annals of Physics*, 373:470–511, oct 2016.

[75] Lianyi He, Haifeng Lü, Gaoqing Cao, Hui Hu, and Xia-Ji Liu. Quantum fluctuations in the BCS-BEC crossover of two-dimensional fermi gases. *Phys. Rev. A*, 92(2), aug 2015.

[76] H Hu, X.-J Liu, and P. D Drummond. Equation of state of a superfluid fermi gas in the BCS-BEC crossover. *Europhysics Letters (EPL)*, 74(4):574–580, may 2006.

[77] Roberto B. Diener, Rajdeep Sensarma, and Mohit Randeria. Quantum fluctuations in the superfluid state of the bcs-bec crossover. *Phys. Rev. A*, 77:023626, Feb 2008.

[78] Daniel E. Sheehy and Leo Radzihovsky. BEC-BCS crossover in "magnetized" feshbach-resonantly paired superfluids. *Phys. Rev. Lett.*, 96(6):060401, feb 2006.

[79] Yuji Matsuda and Hiroshi Shimahara. Fulde–ferrell–larkin–ovchinnikov state in heavy fermion superconductors. *Journal of the Physical Society of Japan*, 76(5):051005, may 2007.

[80] C. Mora and R. Combescot. Transition to fulde-ferrell-larkin-ovchinnikov phases in three dimensions: A quasiclassical investigation at low temperature with fourier expansion. *Phys. Rev. B*, 71:214504, Jun 2005.

[81] T. Mizushima, K. Machida, and M. Ichioka. Topological structure of a vortex in the fulde-ferrell-larkin-ovchinnikov state. *Phys. Rev. Lett.*, 95:117003, Sep 2005.

[82] Zi Cai, Yupeng Wang, and Congjun Wu. Stable fulde-ferrell-larkin-ovchinnikov pairing states in two-dimensional and three-dimensional optical lattices. *Phys. Rev. A*, 83:063621, Jun 2011.

[83] Yean an Liao, Ann Sophie C. Rittner, Tobias Paprotta, Wenhui Li, Guthrie B. Partridge, Randall G. Hulet, Stefan K. Baur, and Erich J. Mueller. Spin-imbalance in a one-dimensional fermi gas. *Nature*, 467(7315):567–569, sep 2010.

[84] Kazushige Machida and Hiizu Nakanishi. Superconductivity under a ferromagnetic molecular field. *Phys. Rev. B*, 30:122–133, Jul 1984.

[85] J. E. Baarsma and P. Törmä. Larkin-ovchinnikov phases in two-dimensional square lattices. *Journal of Modern Optics*, 63(18):1795–1804, 2016.

[86] Jesper Levinsen and Meera M. Parish. *Strongly interacting two-dimensional Fermi gases*, chapter CHAPTER 1, pages 1–75. World Scientific Pub Co Pte Lt, mar 2015.

[87] Lianyi He and Pengfei Zhuang. Phase diagram of a cold polarized fermi gas in two dimensions. *Phys. Rev. A*, 78:033613, Sep 2008.

[88] Daniel E. Sheehy. Fulde-ferrell-larkin-ovchinnikov state of two-dimensional imbalanced fermi gases. *Phys. Rev. A*, 92:053631, Nov 2015.

[89] M. M. Parish, F. M. Marchetti, A. Lamacraft, and B. D. Simons. Finite-temperature phase diagram of a polarized fermi condensate. *Nat Phys*, 3(2):124–128, jan 2007.

[90] E. Taylor, A. Griffin, N. Fukushima, and Y. Ohashi. Pairing fluctuations and the superfluid density through the BCS-BEC crossover. *Phys. Rev. A*, 74(6):063626, dec 2006.

[91] Michael E. Fisher, Michael N. Barber, and David Jasnow. Helicity modulus, superfluidity, and scaling in isotropic systems. *Phys. Rev. A*, 8(2):1111–1124, aug 1973.

[92] Ye Cao, Xia-Ji Liu, Lianyi He, Gui-Lu Long, and Hui Hu. Superfluid density and berezinskii-kosterlitz-thouless transition of a spin-orbit-coupled fulde-ferrell superfluid. *Phys. Rev. A*, 91(2):023609, feb 2015.

[93] Immanuel Bloch, Jean Dalibard, and Wilhelm Zwerger. Many-body physics with ultracold gases. *Rev. Mod. Phys.*, 80:885–964, Jul 2008.

[94] Cheng Chin, Rudolf Grimm, Paul Julienne, and Eite Tiesinga. Feshbach resonances in ultracold gases. *Rev. Mod. Phys.*, 82(2):1225–1286, April 2010.

[95] K. Hueck, N. Luick, L. Sobirey, J. Siegl, T. Lompe, and H. Moritz. Two-Dimensional Homogeneous Fermi Gases. *ArXiv e-prints*, April 2017.

[96] V. L. Berezinskiĭ. Destruction of Long-range Order in One-dimensional and Two-dimensional Systems having a Continuous Symmetry Group I. Classical Systems. *Soviet Journal of Experimental and Theoretical Physics*, 32:493, 1971.

[97] J. M. Kosterlitz and D. J. Thouless. Long range order and metastability in two dimensional solids and superfluids. (Application of dislocation theory). *Journal of Physics C Solid State Physics*, 5:L124–L126, June 1972.

[98] L. Salasnich, P. A. Marchetti, and F. Toigo. Superfluidity, sound velocity, and quasicondensation in the two-dimensional bcs-bec crossover. *Phys. Rev. A*, 88:053612, Nov 2013.

[99] G. J. Conduit, P. H. Conlon, and B. D. Simons. Superfluidity at the bec-bcs crossover in two-dimensional fermi gases with population and mass imbalance. *Phys. Rev. A*, 77:053617, May 2008.

[100] Shaoyu Yin, J.-P. Martikainen, and P. Törmä. Fulde-ferrell states and berezinskii-kosterlitz-thouless phase transition in two-dimensional imbalanced fermi gases. *Phys. Rev. B*, 89:014507, Jan 2014.

[101] G. Bertaina and S. Giorgini. Bcs-bec crossover in a two-dimensional fermi gas. *Phys. Rev. Lett.*, 106:110403, Mar 2011.

[102] J. Carlson, Stefano Gandolfi, Kevin E. Schmidt, and Shiwei Zhang. Auxiliary-field quantum monte carlo method for strongly paired fermions. *Phys. Rev. A*, 84:061602, Dec 2011.

[103] Joaquín E. Drut, Timo A. Lähde, Gabriel Wlazłowski, and Piotr Magierski. Equation of state of the unitary fermi gas: An update on lattice calculations. *Phys. Rev. A*, 85:051601, May 2012.

[104] Hao Shi, Simone Chiesa, and Shiwei Zhang. Ground-state properties of strongly interacting fermi gases in two dimensions. *Phys. Rev. A*, 92:033603, Sep 2015.

[105] K. M. Rasch and L. Mitas. Fixed-node diffusion monte carlo method for lithium systems. *Phys. Rev. B*, 92:045122, Jul 2015.

[106] Zhihuan Luo, Casey E. Berger, and Joaquín E. Drut. Harmonically trapped fermions in two dimensions: Ground-state energy and contact of su(2) and su(4) systems via a nonuniform lattice monte carlo method. *Phys. Rev. A*, 93:033604, Mar 2016.

[107] Brendan C. Mulkerin, Xia-Ji Liu, and Hui Hu. Beyond gaussian pair fluctuation theory for strongly interacting fermi gases. *Phys. Rev. A*, 94:013610, Jul 2016.

[108] M T Yamashita, F F Bellotti, T Frederico, D V Fedorov, A S Jensen, and N T Zinner. Weakly bound states of two- and three-boson systems in the crossover from two to three dimensions. *Journal of Physics B: Atomic, Molecular and Optical Physics*, 48(2):025302, dec 2014.

[109] R. Combescot, M. Yu. Kagan, and S. Stringari. Collective mode of homogeneous superfluid fermi gases in the bec-bcs crossover. *Phys. Rev. A*, 74:042717, Oct 2006.

[110] A. Brunello, F. Dalfovo, L. Pitaevskii, S. Stringari, and F. Zambelli. Momentum transferred to a trapped bose-einstein condensate by stimulated light scattering. *Phys. Rev. A*, 64:063614, Nov 2001.

[111] G. Veeravalli, E. Kuhnle, P. Dyke, and C. J. Vale. Bragg spectroscopy of a strongly interacting fermi gas. *Phys. Rev. Lett.*, 101:250403, Dec 2008.

[112] Sascha Hoinka, Marcus Lingham, Kristian Fenech, Hui Hu, Chris J. Vale, Joaquín E. Drut, and Stefano Gandolfi. Precise determination of the structure factor and contact in a unitary fermi gas. *Phys. Rev. Lett.*, 110:055305, Jan 2013.

[113] Pengfei Zhang and Zhenhua Yu. Energy-absorption spectroscopy of unitary fermi gases in a uniform potential. *Phys. Rev. A*, 97:041601, Apr 2018.

[114] Peng Zou, Eva D. Kuhnle, Chris J. Vale, and Hui Hu. Quantitative comparison between theoretical predictions and experimental results for bragg spectroscopy of a strongly interacting fermi superfluid. *Physical Review A*, 82(6), dec 2010.

[115] Klaus Hueck, Niclas Luick, Lennart Sobirey, Jonas Siegl, Thomas Lompe, and Henning Moritz. Two-dimensional homogeneous fermi gases. *Phys. Rev. Lett.*, 120:060402, Feb 2018.

[116] Xi-Wen Guan, Murray T. Batchelor, and Chaohong Lee. Fermi gases in one dimension: From bethe ansatz to experiments. *Rev. Mod. Phys.*, 85:1633–1691, Nov 2013.

[117] B.R. Holstein. Anomalies for pedestrians. *American Journal of Physics*, 61(142), 1993.

[118] L. P. Pitaevskii and A. Rosch. Breathing modes and hidden symmetry of trapped atoms in two dimensions. *Phys. Rev. A*, 55:R853–R856, Feb 1997.

[119] Félix Werner and Yvan Castin. Unitary gas in an isotropic harmonic trap: Symmetry properties and applications. *Phys. Rev. A*, 74(5):053604–, November 2006.

[120] Maxim Olshanii, Hélène Perrin, and Vincent Lorent. Example of a quantum anomaly in the physics of ultracold gases. *Phys. Rev. Lett.*, 105:095302, Aug 2010.

[121] Chao Gao and Zhenhua Yu. Breathing mode of two-dimensional atomic fermi gases in harmonic traps. *Phys. Rev. A*, 86:043609, Oct 2012.

[122] Yan-Hua Hou, Lev P. Pitaevskii, and Sandro Stringari. Scaling solutions of the two-fluid hydrodynamic equations in a harmonically trapped gas at unitarity. *Phys. Rev. A*, 87:033620, Mar 2013.

[123] T. Peppler, P. Dyke, M. Zamorano, S. Hoinka, and C. J. Vale. Quantum anomaly and 2D-3D crossover in strongly interacting Fermi gases. *ArXiv e-prints*, April 2018.

[124] M. Holten, L. Bayha, A. C. Klein, P. A. Murthy, P. M. Preiss, and S. Jochim. Anomalous breaking of scale invariance in a two-dimensional Fermi gas. *ArXiv e-prints*, March 2018.

[125] Chiara Menotti and Sandro Stringari. Collective oscillations of a one-dimensional trapped bose-einstein gas. *Phys. Rev. A*, 66:043610, Oct 2002.

[126] Edward Taylor and Mohit Randeria. Apparent low-energy scale invariance in two-dimensional fermi gases. *Phys. Rev. Lett.*, 109:135301, Sep 2012.

[127] A. Griffin, Wen-Chin Wu, and S. Stringari. Hydrodynamic modes in a trapped bose gas above the bose-einstein transition. *Phys. Rev. Lett.*, 78:1838–1841, Mar 1997.

[128] S. Stringari. Dynamics of bose-einstein condensed gases in highly deformed traps. *Phys. Rev. A*, 58:2385–2388, Sep 1998.

[129] Hui Hu, Paul Dyke, Chris J Vale, and Xia-Ji Liu. First and second sound of a unitary fermi gas in highly oblate harmonic traps. *New Journal of Physics*, 16(8):083023, 2014.

[130] Giulia De Rosi and Sandro Stringari. Collective oscillations of a trapped quantum gas in low dimensions. *Phys. Rev. A*, 92:053617, Nov 2015.

[131] Hui Hu, A. Minguzzi, Xia-Ji Liu, and M. P. Tosi. Collective modes and ballistic expansion of a fermi gas in the bcs-bec crossover. *Phys. Rev. Lett.*, 93:190403, Nov 2004.

[132] T. Peppler, P. Dyke, M. Zamorano, S. Hoinka, and C. J. Vale. Quantum anomaly and 2D-3D crossover in strongly interacting Fermi gases. *ArXiv e-prints*, April 2018.

List of Publications

The major contents of this thesis have already appeared in some of the following journal papers or preprints co-authored during my PhD study:

1. **Umberto Toniolo**, Brendan C. Mulkerin, Xia-Ji Liu, and Hui Hu,
   Larkin-Ovchinnikov superfluidity in a two-dimensional imbalanced atomic Fermi gas,
   Phys. Rev. A **95**, 013603 (2017).

2. **Umberto Toniolo**, Brendan C. Mulkerin, Chris J. Vale, Xia-Ji Liu, and Hui Hu,
   Dimensional crossover in a strongly interacting ultracold atomic Fermi gas,
   Phys. Rev. A **96**, 041604(R) (2017).

3. **Umberto Toniolo**, Brendan C. Mulkerin, Xia-Ji Liu, and Hui Hu,
   Breathing-mode frequency of a strongly interacting Fermi gas across the two- to three-dimensional crossover,
   Phys. Rev. A **97**, 063622 (2018).

4. Hui Hu, Brendan C. Mulkerin, **Umberto Toniolo**, Lianyi He, and Xia-Ji Liu,
   Quantum anomaly in a quasi-two-dimensional strongly interacting Fermi gas,
   arXiv:1806.04383 (2018).